Quench protection of the LHC quadrupole magnets

Diplomarbeit

Author:

Christoph Kurfürst
Matrikelnummer: 0327552

Supervisors:

Prof. Christian W. Fabjan
Atominstitut der Österreichischen Universitäten
Technische Universität Wien

Dr. Bernd Dehning
Dr. Mariusz Sapinski
CERN BE-BI-BL

CERN-THESIS-2010-070
2010

February 2009 - February 2010, Geneva

Abstract

CERNs Large Hadron Collider (LHC) is a new high energy proton accelerator and storage ring. Its design allows to reach unprecedented beam energies and beam intensities, resulting in a largely increased particle physics discovery potential. The combination of its high beam energy and intensity may lead to beam losses which can have a severe impact on the LHC equipment and damage sensitive elements. To protect those and to measure operational losses, a Beam Loss Monitoring system has been installed all along the ring. The protection is achieved by extracting the beam from the ring in case thresholds imposed on measured radiation levels are exceeded.

The thresholds are estimated through particle shower simulations. The simulated geometry and physic processes need to be precise in order to determine an optimum value, which therefore assures a high availability of the LHC for operation.

This study is focused on the interconnection region between the main dipole and the main quadrupole magnet of the LHC. Six monitors are placed around the interconnection, three for each beam line. As proton impact location two loss patterns are assumed: one derived from halo particle tracking simulations and the other through analytic calculations relying on optical beam parameters.

Particle shower simulations make the link between the amount of energy deposited in the superconducting coil and the signal measured in the ionisation chambers. The energy deposition in the coil results in its temperature increase. In case a critical temperature is exceeded, a transition from the superconducting state to the normal conducting one will occur. This transition is called a quench and is analysed for steady state and for fast transient losses. The fundamental parameters for the analysis are the critical power density and the enthalpy margin respectively.

The combination of the detector signals allows the reconstruction of the loss pattern. Also the quench-protecting thresholds for two protection schemes have been evaluated and an optimisation of the detector positions in order to extend the protected area to the upstream main dipole magnet is proposed.

First LHC results are used to verify the simulations and considerations with measurements, so that conclusions about the simulation accuracy and observed loss patterns could be drawn.

For transient losses the quench protecting threshold used as initial setting in the Beam Loss Monitoring system for the 2010 run is for the first ionisation chamber of 1520 μGy at injection energy and 178 μGy at 7 TeV beam energy. For the second detector the respective values are 575 μGy and 29.7 μGy.

For steady state losses the used threshold for the first ionisation chamber is 4960 μGy/s at injection energy and 1876 μGy/s at collision energy. For the second detector the respective values are 3789 μGy/s and 805 μGy/s.

Kurzfassung

Der am CERN aufgebaute Large Hadron Collider (LHC) ist der weltweit leistungsstärkste Teilchenbeschleuniger und Speicherring. Die Inbetriebnahme des LHC ermöglicht neue Entdeckungen in der Teilchenphysik bei bisher unerreichter Teilchenenergie und Intensität. Diese Kombination aus hoher Energie und Intensität kann zu Teilchenverlusten mit schwerwiegenden Konsequenzen für die Elemente des LHC führen. Um diese Komponenten zu schützen und operative Verluste zu messen wurde ein Beam Loss Monitoring System entlang des Ringes installiert. Der Schutz wird gewährleistet, indem der Strahl extrahiert wird im Falle zu hoher Teilchenverluste.

Die Schwellenwerte für Verluste, die Schaden verursachen, werden mit Hilfe von Teilchenschauersimulationen abgeschätzt. Die Simulationsgeometrie und die Modelle der physikalischen Prozesse müssen möglichst realistisch sein, um eine optimale Verlustschwelle bestimmen zu können und somit eine hohe Betriebsbereitschaft des LHC zu ermöglichen.

In dieser Arbeit werden Teilchenverluste in der Nähe der Verbindung zwischen dem Hauptdipolmagneten und dem Hauptquadrupolmagneten des LHC untersucht. Sechs Detektoren sind in der studierten Region installiert, jeweils drei davon pro Strahllinie. Als Protonenimpaktverteilung wurden zwei Verlustmuster angenommen: eines hergeleitet mittels Teilchentrackingsimulationen und das andere mittels analytischer Berechnungen mit Hilfe der optischen Strahlparameter.

Anhand der Teilchenschauersimulationen können Rückschlüsse über den Zusammenhang zwischen der Energieablage in der Spule des Magneten und der gemessenen Signale in den Detektoren gezogen werden. Die Energiedeposition im Supraleiter führt zu einer Temperaturerhöhung. Im Falle des Erreichens der kritischen Temperatur tritt der Übergang zum normalleitenden Zustand ein. Dieser Übergang wurde für stationäre und instationäre Verluste analysiert. Die fundamentalen Parameter hierfür sind jeweils die kritische Leistungsdichte und die Enthalpietoleranz.

Die Stärke des von den Monitoren gemessenen Signals ist abhängig vom Verlustmuster. Die Rekonstruktion der Teilchenverluste konnte geprüft werden. Zur Abschätzung der Position der maximalen Verluste, wurde eine spezielle Methode entwickelt. Zusätzlich wurden Schwellenwerte für zwei Protektionsstrategien berechnet und es konnte eine Optimierung der Detektorpositionen vorgeschlagen werden, sodass der geschützte Bereich bis zu dem strahlaufwärts gelegenen Dipolmagnet erweitert werden könnte.

Erste gemessene Strahlverluste des LHC wurden analysiert um die Ergebnisse der Simulationen anhand der Messdaten zu verifizieren und so Schlussfolgerungen über die Simulationsgenauigkeit und die beobachteten Verlustmuster ziehen zu können.

Die Anfangseinstellungen des Beam Loss Monitoring Systems für den LHC Betrieb in 2010 im Falle stationärer Verluste wurden bestimmt. Die Schwellenwerte für einen Schutz der Supraleiter vor einen Übergang zum normalleitenden Zustand sind in der Höhe von 1520 μGy, bei einer Teilchenstrahlenergie von 450 GeV und 178 μGy bei 7 TeV für die erste Ionisationskammer. Für den zweiten Detektor sind die entsprechenden Werte 575 μGy und 29.7 μGy.

Im Falle instationärer Verluste sind die ermittelten und verwendeten Schwellen-

werte für die erste Ionisationskammer 4960 μGy/s bei einer Teilchenstrahlenergie von 450 GeV und 1876 μGy/s bei 7 TeV. Für den zweiten Detektor sind die entsprechenden Werte 3789 μGy/s und 805 μGy/s.

Acknowledgements

I want to thank Prof. Christian Fabjan, who agreed to supervise me and the project. Through his experience and past work with the BLM group, he could optimally guide and follow my progress. I am grateful for his support.

I consider myself as very lucky to have been chosen by Barbara Holzer, Bernd Dehning and Mariusz Sapinski to work with them. Together with Annika Nordt they supervised me throughout the whole project, answering my questions and suggesting possible improvements. Additionally their critical questions during numerous student meetings and many more private meetings depicted for me weak argumentation, essential parts and enhanced my progression. Special thanks for good supervision and many helpful meetings go to Mariusz.

Prof. Faber and Ass. Prof. Jericha enabled me in first place to come to CERN. Without their backup my application as a technical student would have drown in the mass of candidates.

Further I want to thank all members of the BLM group. It is a pleasure working with them. Even under stressful conditions while the startup of the LHC, they took their time to help me and discuss with me. I am looking forward to spend the comming years with them.

Also many thanks to my office mates Aurelien, Javier and Julien. Not only they facilitated my introduction to the topic with many useful hints, but also they often loosen up the atmosphere in our everyday work and I gratefully remember situations where we laughed a lot together.

Finally major thanks go to my family. I received a lot of support and encouragement from them, troughout my entire career.

Contents

Chapter 1

Introduction

CERN (European Organisation for Nuclear Research) is a scientific research centre founded in 1954 with the goal to find answers to the questions of particle physics. With its 20 member states and many more collaborating states, CERN proves and strengthens the possibility of fruitfull international cooperation. Since its existence fundamental discoveries have been made, which not only once were honoured with the Nobel price. In order to enable those discoveries CERN scientists motivate, use and develop high-end technologies. Furthermore education plays a major role in CERNs philosophy. Many students have the opportunity to spend part of their studies in this supportive environment and are prepared to be the future scientists.

CERNs main field of research is particle physics and its research instrument is the LHC (Large Hadron Collider), the largest storage ring on Earth. The LHC circumference in about 100 m underground is of 27 km. CERN scientists are witnessing a very fascinating period, as the first beams have been successfully injected into the LHC, ramped and collisions have been observed. Protons and ions are planned to be accelerated to an energy of 7 TeV, which is 7 times higher than for every instrument existing until now (see Figure 2.10). The particles are circulating in two beams on trajectories with opposite direction and the energy stored in the beam will be of 362 MJ. The particles are brought to collision in four main interaction points, where the experiments are located.

Further important and successfull CERN technology development fields are for example radiation protection, medical applications like cancer therapy and medical imaging, industrial imaging, electronics, cryogenics, superconductivity and vacuum technology. CERN is hence not only a research centre, but also a technology laboratory.

To keep the protons on their trajectories high field superconducting magnets have been designed. Through regular and irregular beam losses energy is deposited in those coils. The transition from the superconducting state to the normal conducting one is then possible. The energy a coil can absorb without undergoing this transition was found with ROXIE for transient losses. For the steady state case a heat exchange with the cooling system needs to be taken into account and the coils critical power density was analysed.

Furthermore severe machine deterioration can occur with high energy and intensity beam. To ensure safe beam operation and to avoid unwanted damages and quenches

from beam losses, different feedback and machine protection systems have been developed. This way operational downtimes can be minimised and a high availability of the LHC can be guaranteed. Those protection systems will trigger a beam dump in the case of a critical event. Further emphasis will be on the Beam Loss Monitoring (BLM), where the energy deposition of secondary particle showers are measured.

Geant4 particle shower simulations enable to make the link between the energy deposition in the coil and the signal in the detectors from beam losses at different locations. The estimation of the quench protecting threshold, which is the limit for beam losses at which the magnet is close to lose its superconducting property, is possible through those simulations. If the beam losses lead to detector signals above this limit a beam abort trigger generation occurs and the extraction of the beam is induced, hence assuring the protection of the coil.

To identify ideal placements of the beam loss monitors critical regions of the LHC have been identified. The interconnection between the main dipole magnet and the main quadrupole magnet is expected to be subject of losses. At this location the beta and the dispersion function reach their maximum on the defocussing plane. Also dipole correctors are placed close to the main quadrupole coil, leading to an orbit maximum at their location. Furthermore changes in the aperture limitations occur and misalignments due to construction imperfections are possible. The strategy for a detailed analysis of the situation in the interconnection region was to estimate the behaviour of the particles in this region through theoretical calculations based on the optical beam parameters, through halo particle tracking simulations and finally compare it with the first data from the LHC startup.

Six Beam Loss Monitors are placed in the region of the main quadrupole magnet, three for each beam line. Depending on where the losses happend, the height of the detector signals and relations between them are different. Hence an attempt to conclude from the monitor signals on the location of the maximal losses can be done.

In **Chapter 2** an introduction to the LHC is given, explaining its purpose and how the beam is mathematically described. Also the most sensitive elements inside the accelerator, being the superconducting magnets, are presented together with the challenge of protecting them from beam losses.

Chapter 3 gives an overview over beam loss mechanisms and explains through the impact of beam losses on accelerators elements why it is important to understand them and protect from them. Moreover the beam losses will be analysed in detail for the special case of the interconnection between the main dipole and the main quadrupole.

The purpose of the Beam Loss Monitors in the LHC, described in **Chapter 4**, is to detect those beam losses. The employed detectors are presented, as well as the methods and electronic implementation to treat the monitor signals.

Chapter 5 is devoted to the simulation of beam losses with Geant4. The geometry of the interconnection and its surrounding parts is described. Also the utilised method, the conditions and the assumptions for the simulations are presented. Finally the important results for this study are summarised in this chapter.

In **Chapter 6** the results from Geant4 simulations will be used to estimate the thresholds for each monitor, protecting from quenches of the superconducting coils. The regional specialisation of the BLMs to specific regions is proposed and final thresholds for transient and steady state losses are presented.

In **Chapter 7** the obtained results from simulations are evaluated through mea-

surements and a first method to reconstruct from a loss event through the BLM signals where the maximum of the losses took place.

In the **last Chapter** the conclusions of this study are stated.

Chapter 2

LHC (Large Hadron Collider)

The LHC is a circular particle accelerator with eight straight sections (IRs) where the experiments and the utility insertions are located and eight arcs, where the dipoles are bending the beam for the circular motion. It is an instrument operating two counterrotating beams, brought in collision at high energy so that investigation on open questions in physics can be made. Since November the 30th 2009 the LHC is the worlds highest energy particle accelerator and storage ring with the highest beam energy. The twin beams of protons have been accelerated to an energy of 1.18 TeV. With a stable beam circulating at 450 GeV for 10 hours, the LHC furthermore has proven its effective operation as a storage ring.

In the accelerator chain (see Figure 2.1), the LHC is the last element as it is designed for a beam with injection energy of 450 GeV for protons. From the proton or ion sources, LINACs(LINear ACcelerators) increase the particle energies to 50 MeV. Passing through the LEIR (Low Energy Ions Ring) for ions or the PSB (Proton Synchrotron Booster) for protons, the particles reach the PS (Proton Synchrotron), which is now successfully running for 50 years already. There they reach an energy of 25 GeV and are guided to the SPS (Super Proton Synchrotron), which accelerates the bunches up to the LHC injection energy of 450 GeV. Through the two transfer lines TI2 and TI8 for beam 1 and beam 2 respectively the particles finally reach the LHC, where they are meant to be accelerated to the nominal energy of 7 TeV per charge with radio frequency cavities. For ions the preacceleration is slightly different and in the LHC their nominal energy is 2.76 TeV per charge.

The beam is ejected through the dump system located in IR6. This is done regularly under normal operation circumstances and also in cases of an unwanted event.

Remarkable is furthermore the continuous ultrahigh vacuum along the beam tube of about 10^{-10} Torr, to minimise unwanted beam interactions with rest-gas molecules. This corresponds to about $3{\cdot}10^6$ particles/cm^3.

Another challenging and impressive project is the cryogenic system, which is cooling the over 2000 superconducting magnets to 1.9 K with 60 tonnes of liquid Helium.

2.1 The experiments and their goals

The four big LHC experiments are situated at the interaction points (IP) of the LHC, where the beam trajectories cross each other, the beam size is minimised and head-on

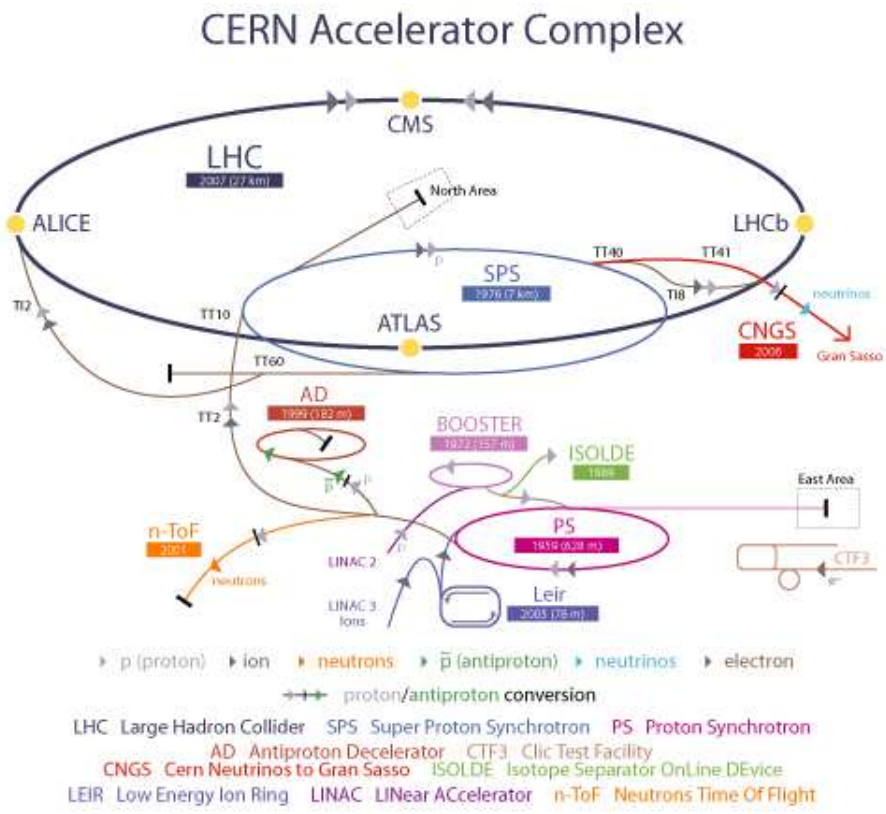

Figure 2.1: Schematic of the CERN accelerator complex. The beams are generated at the LINAC2 or 3 and their energy is increased in the BOOSTER, PS and SPS.

collisions can be generated.

An important criteria for the quality of the experiments is the luminosity, which is the density of colliding particles per unit time. In the case of colliding beams with a transverse Gaussian particle distribution the luminosity is [1]:

$$L = \frac{N_1 N_2 n_b f_{rev} \gamma_r}{4\Pi\epsilon_n \beta^*} F \tag{2.1}$$

where N_1 and N_2 are the number of particles per bunch for beam 1 and 2 respectively, n_b is the number of bunches per beam, f_{rev} is the revolution frequency in the ring, γ_r is the relativistic gamma factor and F is a geometric correction factor due to the crossing angle at the interaction point. ϵ_n is the transverse normalised emittance and β^* is the betatron function at the interaction point. These two parameters describe together the beam size. In order to have a high luminosity the beam intensity has to be maximised (N,n_b), whereas the beam cross section needs to be minimised(ϵ,β). This possibility is limited by the beam-beam effect, where electromagnetic fields are created by the beams themselves. The expected peak luminosity is of 10^{34} cm^{-2}s^{-1} in ATLAS and CMS.

ATLAS (A Toroidal LHC ApparatuS) and CMS (Compact Muon Solenoid) are build as detectors for high energy proton-proton collisions. They follow the same main purpose to find the Higgs boson, a particle which existence has been predicted 50 years

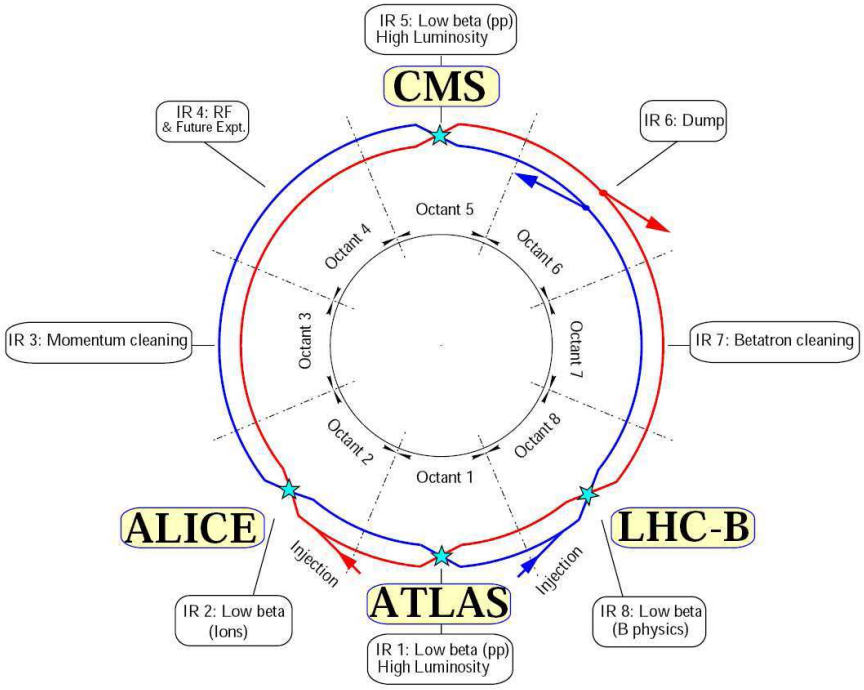

Figure 2.2: LHC Overview with the four main experiments and the acceleratorfacility areas. The red and blue lines stand for the beam lines and show their relative locations to each other as well as the crossing areas.

ago. Other goals are the search for supersymmetry and particles responsible for dark matter. The purpose of those two experiments is the same, but the used technologies are very different.

ALICE (A Large Ion Collider Experiment) is dedicated to the LHC Heavy Ion program. One month per year instead of the proton acceleration, heavy ions will be accelerated with a luminosity of about 10^{27} $cm^{-2}s^{-1}$. In the first period high energy Pb-Pb collisions are the goal, which are expected to produce a quark-gluon plasma. The purpose of the experiment is to understand the quark-confinement.

LHCb (LHC beauty) concentrates its researches on CP-parity violation in the b-quark system. The question why the Universe seems to be made mainly of matter, but no antimatter is being investigated.

In the first three days of the LHC start-up in 2009 already all four experiments observed successfully collisions from beams at injection energy and 1.18 TeV per beam.

2.2 Beam Parameters

In Table 2.1 one can see LHC beam parameters that will be essential for further analysis in this study.

The beam dynamics are formally described through a six dimensional phase space. Each particle can be represented by one point and its corresponding six coordinates:

	Injection	Collision
Beam Data		
Proton energy [GeV]	450	7000
Relativistic gamma	479.6	7461
Number of particles per bunch	$1.15 \cdot 10^{11}$	
Number of bunches	2808	
Transversal normalised emittance [μm rad]	3.5	3.75
Stored energy per beam [MJ]	23.3	362
RMS bunch length [cm]	11.24	7.55
RMS energy spread δE/E$_0$ [10^{-4}]	3.06	1.129
Revolution frequency [kHz]	11.245	
Lattice		
Maximum dispersion in arc [m]	2.018(h)/0.0(v)	
Maximum β in arc [m]	177(h)/180(v)	

Table 2.1: LHC parameters with respect to later analysis

three for the location and three for their momenta in the different directions. The area in phase space occupied by the particles inside the beam is called beam emittance. Due to the much higher transverse oscillation frequencies one can consider in a first approximation the longitudinal one as independent. Figure 2.3 shows the phase space area in the 2 dimensional phase space for the transverse x-direction.

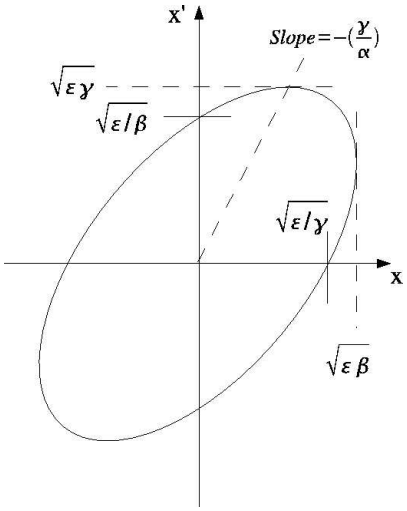

Figure 2.3: Phase space ellipse for a diverging beam with Twiss parameters α, β, γ and ϵ.

Where

$$x' = \frac{dx}{dt} \tag{2.2}$$

is the transverse velocity of the particle in x-direction. α, β, γ and ϵ are the ellipse

parameters, also called the Twiss parameters. Additionally β is the betatron function, giving the modulation amplitude of the betatron oscillation of the particles in the considered plane. ϵ is the beam emittance, a measure for the ellipse area. The index u will further be used to indicate the transverse coordinates x or y.

The phase space ellipse is described by:

$$\gamma u^2 + 2\alpha u u' + \beta u'^2 = \epsilon \tag{2.3}$$

The area of the ellipse is proportional to the emittance: Area = $\Pi\epsilon$ [2]. Through the geometrical properties of an ellipse, one can further write the following corelation:

$$\beta\gamma - \alpha^2 = 1 \tag{2.4}$$

The normalised emittance is defined by:

$$\epsilon_n = \beta_r \gamma_r \epsilon \tag{2.5}$$

with:

β_r**:** Relative velocity

γ_r**:** Lorentz factor of the special relativity

ϵ**:** Transverse emittance. For the LHC at injection energy $\epsilon = 7.82\,nm$. For collision energy $\epsilon = 0.503\,nm$.

ϵ_n**:** Normalised emittance. For the LHC $\epsilon_n = 3.75\ \mu m$ [3].

The normalised emittance was defined, and therefore has the property, to stay constant when the beam is accelerated.

The Twiss parameters β and γ should not be confounded with the relativity parameters β_r and γ_r.

For a Gaussian beam the relation between beam size, betatron function and beam emittance is given by:

$$\sigma = \sqrt{\beta\epsilon} \tag{2.6}$$

Where σ is the sigma-parameter of the Gaussian parametrisation of transverse beam intensity. The assumption of Gaussian beam is often a good approximation for the beam core, which is approximately $\pm 3\sigma$, whereas the particles in the tails outside 3σ form the beam halo. Beam intensities for protons are often given in $\sqrt{6}\sigma$, for which in three dimensions 95.74% of the beam is included [4].

The beam in a storage ring is never perfectly monochromatic. The particles have a finite spread of energies around the nominal energy cp_0. Passing through dipoles the beam is bent. As each particle has a slightly different longitudinal velocity, they are bend differently by the Lorentz force. Therefore protons with higher energies gather more on the outside and those with lower energies more on the inside of the LHC ring.

This transverse spread of particles around the ideal trajectory for nominal energy is described by the dispersion function D_u. Taking this into account the beam size for a Gaussian beam becomes:

$$\sigma = \sqrt{\beta\epsilon + (D_u \sigma_p)^2} \tag{2.7}$$

where $\sigma_p = \sigma_\epsilon / cp_0$ with σ_ϵ the mean energy spread and cp_0 the nominal energy.

In the quadrupoles particles with different longitudinal velocity are then focused to different points as seen in figure 2.4. This effect called chromaticity can be reduced through sextupole magnets, that work like quadrupoles, but with varying focal strength. Therefore higher energy particles feel some additional focussing, whereas the lower energy protons from an inner trajectory are less focused.

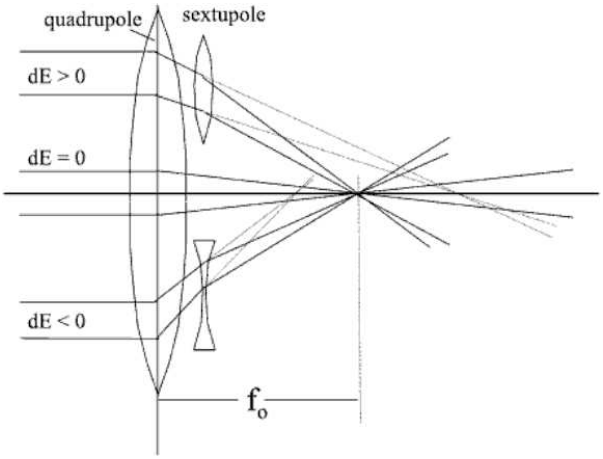

Figure 2.4: Origin and correction of chromaticity from [4].

2.3 Superconducting magnets

Superconductors are materials that have zero resistivity under certain conditions. The advantage of usage of superconducting wires in magnets is the possibility to reach high magnetic fields without heat dissipation. The superconducting material must be cooled to very low temperatures around 10 K in order to work properly. Some high temperature superconductors can work above a temperature of 100 K (for example BSCCO and TBCCO) and a lot of effort is done to find and develop materials with superconductivity for even higher temperatures.

A transition to the normal conducting state takes place, if one of the following critical parameters is exceeded:

- temperature T_c,
- current I_c and
- magnetic field H_c.

This is often summarised in a three dimensional phase diagram as a critical surface. The critical surface can be seen for the example of Niobium-Titanium, a material used in the LHC magnets, in figure 2.9. Every state underneath the surface is superconducting, while for points above, at least one critical parameter has been exceeded and the material is normal conducting.

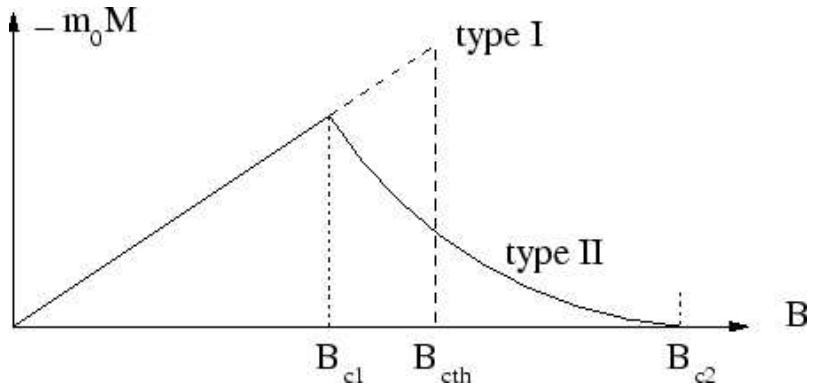

Figure 2.5: Type I and Type II superconductors magnetisation properties [5]. m_0 on the y-axis is the magnetic permeability in vacuum known as μ_0. For a Type I superconductor the magnetisation is M = -B/μ_0

Due to different physical properties the superconductors can be classified into two groups: Type I and Type II superconductors. The difference can be seen through the example of the magnetisation of the material as a function of the applied magnetic field in figure 2.5.

The magnetic field inside a Type I superconductor needs to be zero. When the strength of the applied field surpasses the critical value B_{cth}, the superconductivity immediately breaks down. The critical magnetic field is very low. Therefore Type I superconductors do not allow the construction of superconducting magnets.

Below the critical field B_{c1}, a type II superconductor has the same properties as a type 1 superconductor, being in the Meissner phase, in which the field is completely excluded from the inside of the magnet. After B_{c1} a smooth transition to the normal conducting state takes place in case of increasing field. The smoothness can be seen in figure 2.5 between B_{c1} and B_{c2}. This is due to the existence of a mixed phase, meaning that magnetic flux lines can penetrate the material at high enough external fields, without the loss of superconductivity. Type II superconductors have for each parameter two critical values. Should the material be in between the critical values, the mixed state is observed, whereas an exceeding of the higher critical value leads to the loss of the superconductive property.

2.3.1 The main quadrupole (MQ)

In the LHC are 1232 main dipoles (MB), 392 main quadrupoles (MQ) and more than 4000 corrector magnets. They are cooled at cryogenic temperatures of 1.9 K and 4.5 K. A two-in-one design was used for allmost all the LHC magnets, meaning that the magnets for the two beam lines are accommodated in the same cold mass cryostat. The cross sections of the two main LHC magnets for one beam are shown in figure 2.6. The structural stability in presence of large electromagnetic forces is achieved by enclosing the cold mass with a rigid collar made out of austenitic steel. A common iron magnetic yoke shown in figure 2.7 then surrounds the collars.

The MQ is the major element of the Short Straight Section (SSS) inside the LHC arcs. Depending on the configuration there are various corrector magnets on both sides

of the MQ in the SSS. A small corrector magnet is installed on one side: an octupole MO, a tuning quadrupole MQT or a skew quadrupole MQS. On the other side are installed larger combined sextupole-dipole correctors MSCB [3]. All magnets in the SSS are together in the same cryostat. If a small corrector loses its superconductivity the beam can still run normally, while in the case of MQ the beam is not stable anymore. Therefore the main quadrupole magnet is the one studied further.

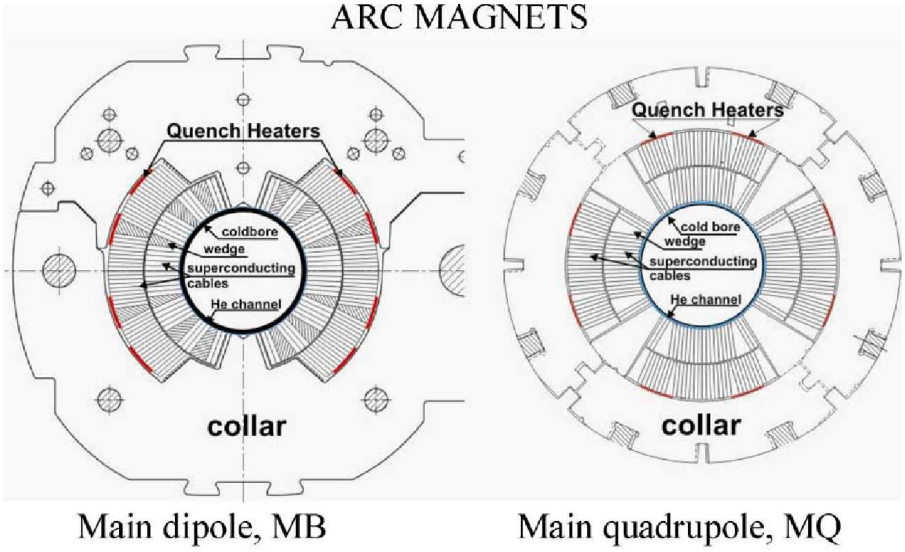

Figure 2.6: Cross section of LHCs main magnets for one beam.

Quadrupoles play a major role in accelerator physics. They are needed to ensure a constant beam envelope during the circulation of the beam. The LHC quadrupole cross section with its magnetic field is shown in Figure 2.7. They have a focussing effect on the beam in one plane, while they are defocussing in the other one. In Twiss parameters this is translated to a maximum of the beta function in the defocussing plane and a minimum in the focussing one, corresponding to a maximal and minimal beam size respectively (see equation 2.6). In order to provide beam stability, quadrupoles are arranged in FODO lattices, where defocussing quadrupoles and focussing ones are periodically alternated.

The quadrupoles are cooled to 1.9 K and have a nominal current of 7.6 kA generating a peak field of 6.85 T in the conductor. They have a magnetic length of 3.1 m and store an energy of 395 kJ per magnet. Each cable of the MQ is formed of 36 strands, containing copper and about 6500 superconducting Niobium-Titanium filaments of 6μm diameter (see figure 2.8). They are insulated with polyimide tapes. The copper is very important as it provides the mechanical stability and has a low resistance, where the high currents can flow in case of transition to the normal conducting state.

A quench, which is the transition from super- to normal conducting state, happens if temperature, magnetic field or current density exceed a critical value. This relation can be seen through the critical surface shown in figure 2.9. For instance for the main dipole the critical current I_c is above 12960 A, for a magnetic field of 10 T and at a temperature of 1.9 K. Should the quenched volume be small, a self-healing process of the coil is possible.

The amount of energy a superconducting magnet can absorb before transition to the normal conducting state has been subject for many research [7] [8]. In the case of the LHC it mainly depends on the particle energy and on the timescale of the losses. The duration of the losses δt needs to be compared with the time constants τ for heat exchange of the system. The most critical losses are the ones happening faster than the time τ_{metal} for heat transfer in the cable, as the energy deposition then occurs locally, without any heat evacuation. The energy from losses slower than the heat exchange with the cryogenic liquid He-system $\delta t > \tau_{He}$ can be evacuated from the cable using the enthalpy of the Helium.

In this study two extrem cases are investigated: transient and steady state losses.

2.4 The machine protection systems

With its energy stored in every beam of 362 MJ at nominal conditions, the LHC surpasses its antecessor by a factor of 200 (see Figure 2.10). Due to this high beam energy and intensity, a sophisticated machine protection system needed to be designed. While the collimation system and the QPS (Quench Protecting System) will be shortly presented, a major further emphasis will lie on the functioning of the BLM (Beam Loss Monitoring) system, to which the entire chapter 4 has been dedicated. Yet before the introduction to the ionisation chambers an overview of beam loss origins in the LHC, as well as their impact on accelerator elements will be given in chapter 3. Those considerations being the reason for the design of the BLM system, explaining its purpose and its protection functionality. Figure 2.11 shows the relation between the duration of the losses and its corresponding protection mechanisms.

The LHC protection through collimators is a passive system, enabling the protection from losses occurring with time scales shorter than the extraction time of the beams. Collimators have two moveable jaws that can be positioned in order to define the free path for the beam core. Halo particles on trajectories too large for a continuous circulation are removed so that they can not cause damage anymore. Figure 2.12 shows the principle of three-stage beam cleaning in the LHC with three collimators in a row.

Considering the high beam energies in the LHC, the collimator system needs to have a cleaning efficiency above 99.99% to concentrate the steady state losses at appropriate locations and not on cold elements [9].

Previous to the experiments they furthermore enable a certain beam conditioning by stopping particles that could lead to parasitic detections.

In case energy is deposited in the superconducting magnets a transition to the normal conducting state is possible. To detect and initiate a protection procedure the QPS has been developed. It surveys the voltage in the superconducting magnets and if a local quench is detected, it warms up the whole coil, so that it becomes normal conducting. By provoking this transition to the normal conducting state for the whole coil, the energy stored in the magnetic field is dissipated over the entire volume of the superconductor and major damage can be avoided. Quenches should be avoided, as they have a negative influence on the magnets lifetime and the coil needs ten minutes to two hours for recovery into a superconducting state.

In parallel to the QPS the BLM (Beam Loss Monitoring) system has been devel-

oped, which reacts faster to losses and enables quench and damage protection (see section 4). With the BLMs no quench should occur, while the QPS induces a controlled quench and both therefore avoiding damage of the superconducting coils. The QPS is hence an active system, that can trigger a beam dump together with many other redundant LHC protection, like the cryogenic system and the Beam Conditioning Monitoring for ATLAS. Redundancy in the LHC machine protection system has a high priority.

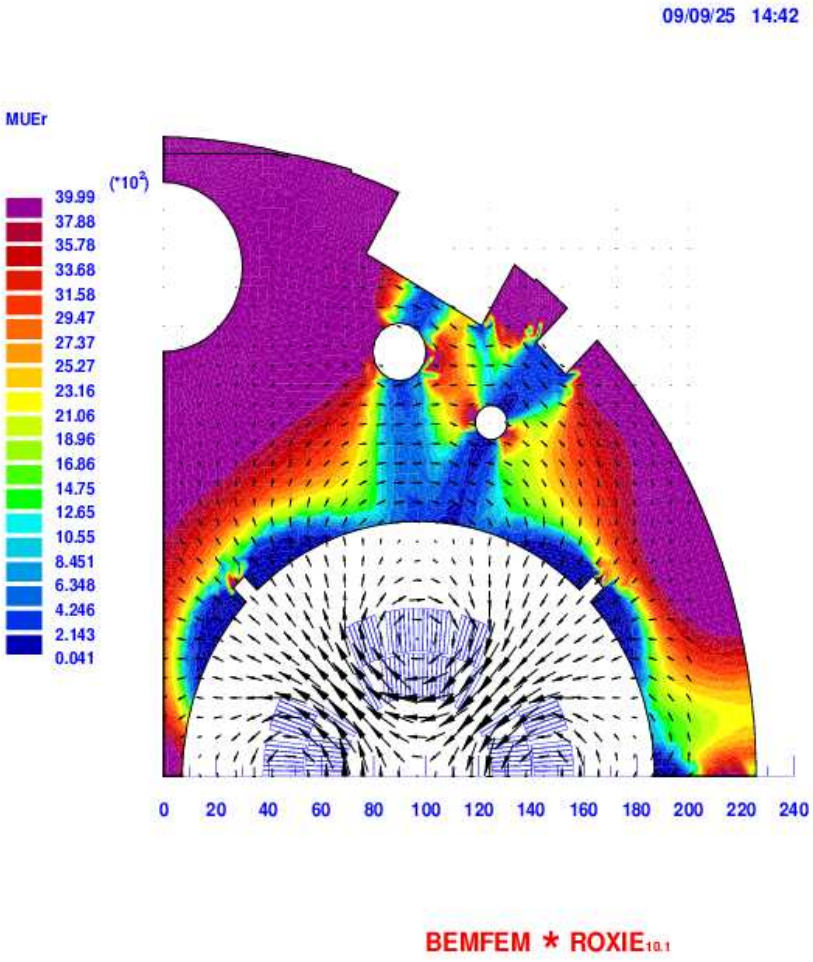

Figure 2.7: Quadrupole cross section with iron yoke, the collar is not shown. The arrows illustrate the typical magnetic field with its amplitude and direction. The colours of the iron yoke indicate the relative permeability of the iron material. The plot was done with ROXIE, see section 3.2.1.

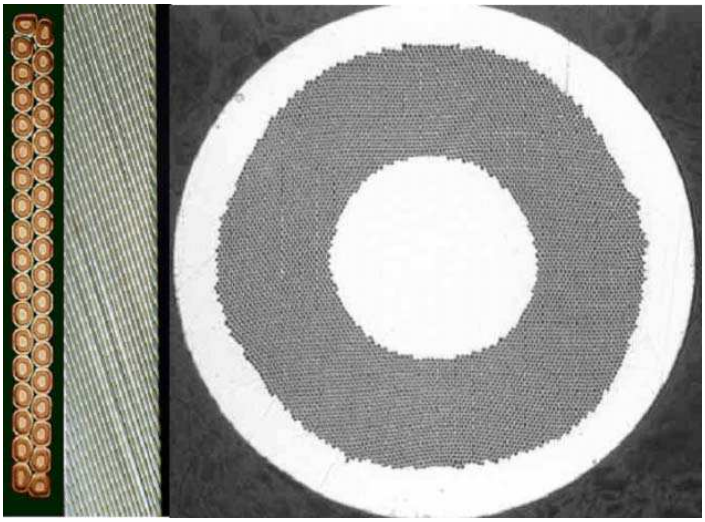

Figure 2.8: Picture of the cable with 36 strands and in the zoom the Niobium-Titanium filaments can be seen [3].

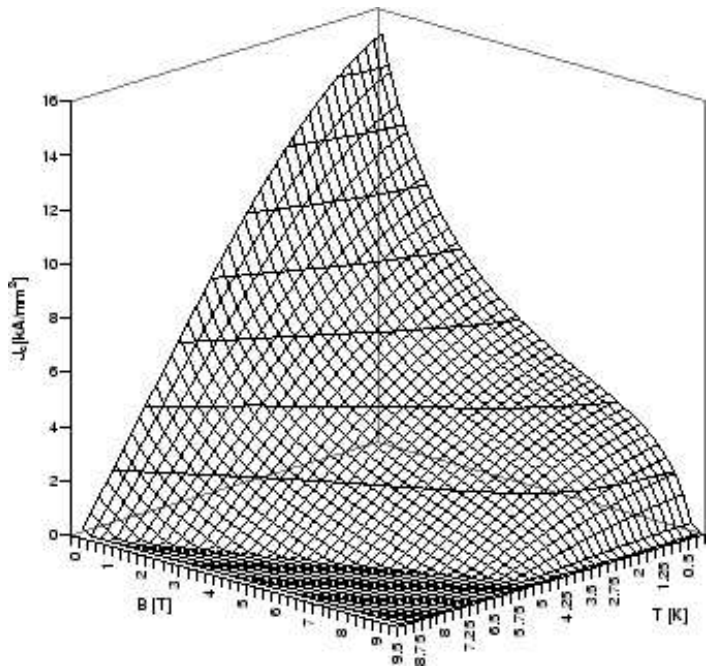

Figure 2.9: Niobium-Titanium critical surface [6].

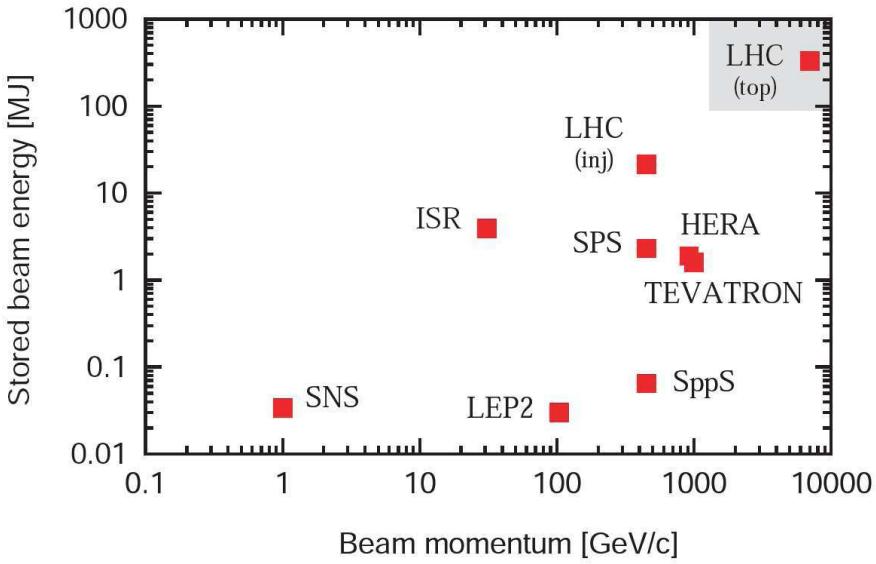

Figure 2.10: Beam energy and beam momentum comparison between existing accelerators. Courtesy of R. Assmann.

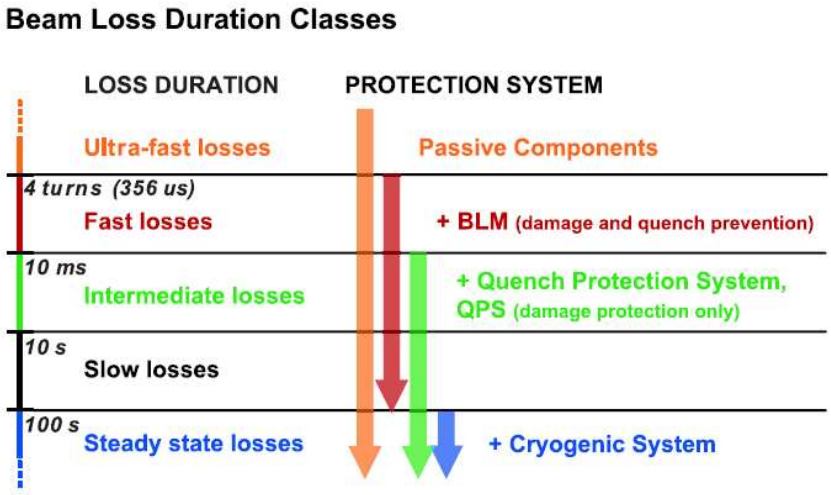

Figure 2.11: Classification of the protection systems according to the loss duration

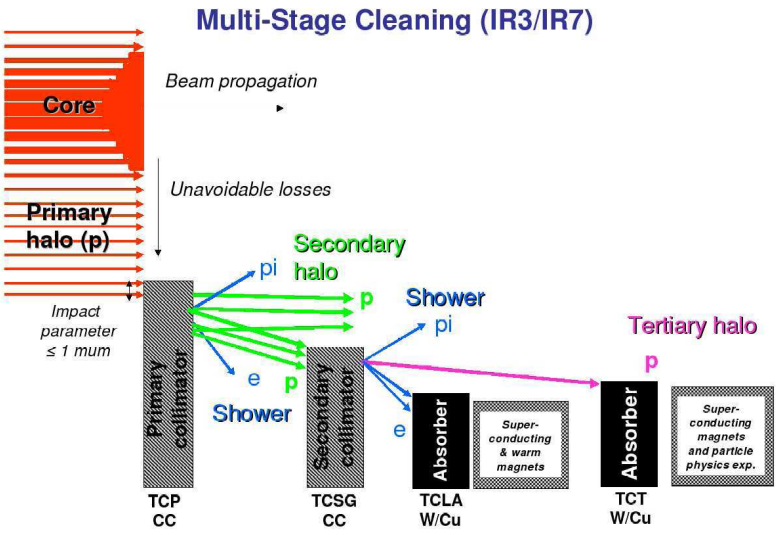

Figure 2.12: Principle of the collimation system

Chapter 3

Beam losses

The LHC beam will reach unprecedented energies. To make this possible high end technology, that can be extremely sensitive, is used close to the beam trajectory. For equipment protection it is important to understand the beam loss mechanisms, their impact on the magnet elements and to analyse the regions where major parts of those losses are expected.

3.1 Beam loss origins

In this part an overview will be given about the known reasons for particle losses.

One can classify the losses into regular and irregular ones. First happen even under perfect machine circumstances, while second are basically due to errors. Additionally in the literature one can often find the following categorisation of regular particle losses: losses due to scattering and losses due to instabilities [4]. By themself most of the regular beam losses can be considered as slow compared to the LHC revolution time. They mainly are the root for certain performance limitations. For example they limitate the LHC luminosity, can cause beam instabilities or reduce the beam lifetime and provoke emittance growth. Added up and together with machine imperfection the effects of beam losses need to be understood and can compromise the correct functioning of the LHC.

For later discussion one needs to define two terms: beam life time and emittance growth. The beam life time τ is define as the time at which the beam intensity N(t) declined to a value of 1/e of the initial intensity N(0):

$$N(t) = N(0)e^{-\frac{t}{\tau}} \tag{3.1}$$

The emittance growth on the other side is characterised through the time τ_ϵ:

$$\epsilon_u(t) = \epsilon_u(0)e^{\frac{t}{\tau_\epsilon}} \tag{3.2}$$

3.1.1 Collisions

Collisions for the main experiments in the interaction points are the main reason for losses and beam life time reduction. Collisions between protons of the two counterwise rotating beams can be categorised into the following cases:

- inelastic
- elastic and
- diffractive.

Only particles from inelastic collisions will be seen by the experiments detectors[1]. The products from diffractive and elastic interactions together with some remains from inelastic collisions will not have such high scattering angles. They will therefore be lost later or cause emittance growth depending on the size of the angle. The mean scattering angle was found to be around 34 μrad at 7 TeV [10]. Such an angle is small and does not cause losses. The major part of the scattered particles is therefore not lost, but performs a betatron oscillation and induces emittance growth. This transverse emittance growth is given by [11]:

$$\frac{d\epsilon_x}{dt} = \frac{(\beta^*_{1x} L_1 + \beta^*_{2x} L_2)\sigma_{el}\langle\theta_x^2\rangle}{M N_b} \tag{3.3}$$

where β_i and L_i are the beta function and the luminosity respectively at the i-th interaction point, σ_{el} is the scattering cross section for elastic proton-proton collisions, $\sqrt{\langle\theta_x^2\rangle}$ the RMS of the elastic scattering angle, M the number of bunches and N_b the number of particles per bunch. This leads to an emittance growth rate for one degree of freedom of 87 h and a beam life time of around 310 h [10].

The beam life time due to inelastic collisions is:

$$\tau_N = \frac{N_0}{L_0 \sigma_{inel}} \tag{3.4}$$

with τ_N the beam halving time, N_0 and L_0 respectively the initial number of protons and the initial luminosity and σ_{inel} the inelastic cross section of proton-proton collisions. The beam life time due to inelastic collisions is of about 108 h [10]. Due to their small scattering cross section the contribution to the overall beam life time of diffractive collisions is negligible.

3.1.2 Intra-Beam scattering (IBS)

IBS is the small angle Coulomb collisions of two particles from the same bunch. This energy exchange induces a coupling between the transverse and longitudinal emittances. In the case of the LHC there is continuous emittance growth in all directions due to IBS.

At injection energy the emittance growth rate is of 38 hours for transverse IBS and 30 hours for longitudinal IBS. At collision energy the transverse beam emittance growth is about 105 h, whereas for the longitudinal one it is about 63 h [3]. The values are obtained from MAD-X simulations using the Bjorken-Mtingwa theory.

[1] With the exception of some detectors made to investigate the diffractive events (e.g. TOTEM and fLHC)

3.1.3 Touschek scattering

The Touschek scattering is for large angle particles collision, where enough energy is exchanged between the transverse and longitudinal plane to remove particles from the stable RF bucket. Those unaccelerated particles build the coasting beam and lose their energy mainly due to synchrotron radiation(See section 3.1.5). For a Gaussian particle distribution the beam lifetime is given by:

$$\frac{1}{\tau_{Touschek}} = -\frac{1}{N_b}\frac{dN_b}{dt} \tag{3.5}$$

In the LHC the coasting beam gets populated at a rate per proton per hour of $1.8 \cdot 10^{-4}$ for 450 GeV and $8 \cdot 10^{-5}$ for 7 TeV [3]. The Touschek lifetime is then of 4831 hours for injection energy and 12077 hours at collision energy [12] and has hence a small effect on the beam life time compared to other effects.

3.1.4 Residual gas scattering

In the LHC is ultrahigh vacuum along the beam tube of about 10^{-10} Torr, which corresponds to about $3 \cdot 10^6$ particles/cm^3. The beam can collide elastically and inelastically with those resting gas molecules. For inelastic scattering a nuclear interaction takes place and secondary particles are created. Their energy can be expected to be dissipated locally within 15 m of the collision. The beam lifetime from inelastic residual gas scattering is estimated to be about 129 hours. For elastic scattering the obtained outcome depends on the scattering angle:

- emittance growth occurs for a small scattering angle(the growth rate is of 87 hours for 7 TeV),
- scattered protons with a larger betatron amplitude than the one allowed by the collimation system will be lost in the betatron cleaning insertions,
- direct proton losses in the aperture are possible for large scattering angles.

The beam lifetime from elastic residual gas scattering is estimated to be about 459 hours.

The heat load in the magnets cold bore from this effect is not neglectable. The beam lifetime should be of 100 hours with a heat load not exceeding 0.1 W/m. From those target values one can define an upper limit for the LHC gas density of different molecules. Knowing that the relation between the beam lifetime τ and the density n_i of the residual gas molecules is:

$$\frac{1}{\tau} = c\sum_i \sigma_i n_i \tag{3.6}$$

Where the sum goes over the different gas molecule types, with σ_i being the nuclear scattering cross section for the i-th type.

This then leads for each molecule to different acceptable densities shown in [3]. As H_2 has the smallest scattering cross section, the largest density of about $1.2 \cdot 10^{15}$ molecules$\cdot$m^{-3} is allowed for it. This is important to notice, as the normalised emittance growth depends on the mass of the molecules and will therefore be dominated by hydrogen.

3.1.5 Synchrotron radiation

Synchrotron radiation is an electromagnetic radiation that charged ultrarelativistic particles under transverse acceleration emit[2]. In storage rings it is emitted tangentially to the beam trajectory and in direction of the particle velocity. It is proportional to γ^4, so up to now it was important for electron storage rings and neglectable for protons. With the expected LHC proton energies synchrotron radiation yet needs to be taken into account. The radiated power for transverse acceleration is [1]:

$$P_{\perp} = \frac{c}{6\pi\epsilon_0} e^2 \frac{(\beta\gamma)^4}{\rho^2} \tag{3.7}$$

where ϵ_0 is the vacuum dielectric constant, ρ the curvature radius, e is the proton charge and β and γ the relativistic parameters.

Moreover the energy lost per turn by the protons in the LHC is:

$$U_0 = \frac{e^2\beta^3\gamma^4}{3\epsilon_0\rho} \tag{3.8}$$

For injection energy the synchrotron radiation is still neglectable with a radiated power of 66 mW per beam, corresponding to an energy loss of 0.11 eV per turn per proton. For 7 TeV the situation is different and the energy lost per turn is about 6.7 keV. The total radiated power is of 3.9 kW [3].

Important to notice is the effect of synchrotron radiation damping, which is significant at collision energy with 13 and 26 hours for longitudinal and transverse emittance damping respectively. Synchrotron radiation therefore can compensate some of the emittance growth mechanisms. For the LHC the general assumption is that the damping takes out the effect of long range beam-beam interactions and RF noise. So synchrotron radiation is actually not provoking beam losses like other discussed effects, but in contrary noticeably reducing the emittance growth at collision energy, which makes losses rather less probable.

3.1.6 Electron cloud effects

Coulomb scattering of the protons with electrons is completely negligible, but other effects have to be taken into account.

Through beam losses on surrounding machine parts and scattering with residual gas molecules, ionisation takes place and electrons are liberated. Those are attracted by the electrically positive beam and secondary emission on the vacuum chamber walls is the consequence. Further electrons are created exponentially, building up an electron cloud. This cloud influences the beam trajectory and causes emittance growth [13]. Those photoelectrons and electrons from secondary emissions can be responsible for a noticeable heat load. This heat load can be a serious menace for the superconducting magnets. The developed beam screens intercept the major part of the energy from electron clouds. Still some heat reaches the cold magnets through nuclear interactions. Depending on the assumed secondary emission yield and bunch intensity the heat load on the magnets can exceed the cooling capacity of the cryogenic system. For a yield of

[2] Radiation from longitudinal acceleration can be neglected

1.1 and nominal bunch spacing safe operation is anticipated [3]. Those considerations are moreover important for the LHC luminosity and electron clouds clearly account for a limitation in this matter. In addition electron clouds can influence the vacuum conditions, through gas desorption by electrons on the chamber walls.

From the experience with SPS, CERN scientists could learn about the effects of electron clouds, also endangering the beam stability. For the LHC several counteractive measures have therefore been designed. Examples are the TiZrV getter films [14] and the beam screen with some special characteristics.

3.1.7 Long range Beam-beam effects

The beam-beam effect is a longdistance interaction between the two counterwise rotating beams in the LHC. It can cause a beam life time reduction, emittance growth and instabilities.

Due to the non-linear field of the other beam, the trajectories of single particles can be disturbed in such a way, that they get lost.

As the LHC presents symmetry breaking parts, one may assume that the coherent effects from long range beam-beam interaction can be neglected.

3.1.8 Accidental beam losses

Accidental beam losses are the most dangerous effects. They can be fast and their prediction is impossible. They typically happen in case of operational mistakes or machine failures. The loss rate can then increase very rapidly and endanger further machinery. Due to its fast reaction time, the Beam Loss Monitoring system, that will be discussed in detail in the next chapter, is perfectly able to deal with those irregular losses and induce a beam abort. Later analysis of the post mortem data should then enable to understand the causes of losses, make the right corrections and possibly avoid the error in the future.

Examples for accidental beam losses are: injection losses(those are important and mainly due mismatches with SPS and transverse injection oscillations leading to losses on IR7 and IR3 collimators), kickers malfunctioning(misfiring), operator errors, resonances, generally beam instabilities, parameter control challenges and vacuum leaks.

3.1.9 Summary of lifetime and emittance growth

The timescales for the beam lifetime and emittance growths of the previously introduced beam loss effects are summarised in table 3.1.

3.2 Impact of beam losses on accelerator elements

The impact of beam losses on accelerator elements needs to be understood, in order to create awareness for sensitive parts, estimate the nature and seriousness of possible damages and design protection systems accordingly. Protons with high energy hitting a target generate a hadronic shower. This interaction leads to energy deposition in the material of the target and an increase of temperature. The consequences can be

Process	Lifetime [h]	Emittance growth [h]
Residual Gas - inelastic	129	-
Residual Gas - elastic	459	-
Touschek	1250	-
Collision - inelastic	108	-
Collision - elastic	310	44
IBS transverse	-	80
IBS longitudinal	-	61
RF Noise/beam-beam	-	55
SR - longitudinal	-	-13
SR - transverse	-	-26

Table 3.1: Beam lifetime contributions and emittance growth rates of different beam loss mechanisms for nominal physics [10].

damages and in the case of a superconductor the transition to the normal conducting state. Also long term radiation damage needs investigation.

The effect of beam losses on different materials used in the LHC equipment has been studied in [15]. The results from a particle-matter interaction simulation program FLUKA are compared with material damage experiments done in TT40. The analysed material is zinc, copper and stainless steel (316L, INCONEL). Zinc serves as a comparison group having a lower melting point of 420°C than the others. Copper with a melting point of 1083°C and the stainless steels are materials used in the LHC equipment. Cu is of special interest for this study, as it is used in the beam screen and in the superconducting magnets.

For a 450 GeV proton beam of a size of σ = 1 mm, the maximum energy density in a Cu target is reached after a distance of about 15 cm and is of E^D_{max} = 10 GeV/cm^3/proton = 1.6 $\cdot$ 10^{-9} mJ/cm^3/proton. From this value an estimation of the critical number of protons until the melting point of copper is reached can be done:

$$n_{critical} = \frac{\Delta T \rho C_p}{E^D_{max}} \tag{3.9}$$

with ρ being the materials density, C_p its heat capacity and ΔT the temperature difference from room temperature until the melting point. The obtained result is $n_{critical}$ = 2.3 $\cdot$ 10^{12} protons [15]. This can be considered as the damage limit and corresponds to around 5% of ultimate beam intensity with full injected batch. The effect of direct beam losses on Cu plates as targets is shown in figure 3.1. Noteworthy is that no stress related damage, like cracks or twisting, has been observed.

The understanding of the damage limit is important. The reparation or replacement of damaged elements is time consuming, complicated and expensive. For the protection of superconducting magnets the quench limit is the one enabling ideal safety from damages. Its limit in terms of critical number of protons is much lower. This is due to the fact that inducing a quench needs less energy deposition than melting of copper.

Figure 3.1: Effect of beam irradiation with 450 GeV protons on two Cu plates on different positions. The letter A, B, C and D correspond to tested beam intensities. D is the highest intensity with $7.92 \cdot 10^{12}$ protons and leads to the first damages on the plates. While plate 11 shows just slight discolouration, plate 12 situated closer to the location of maximal energy deposition presents melted material [15].

3.2.1 Enthalpy limit of MQ

The superconducting magnets are cooled at 1.9 K. Beam losses can deposit enough energy to induce a quench. For the calculation of the threshold, it is important to estimate how much energy the magnet coil can absorb without transition to the normal conducting state.

A situation without heat transfer to the cooling system can be considered as the heat deposition time is short compared to the cooling time constant. Hence the enthalpy margin of the magnet cables is the critical factor for a quench of the quadrupole and therefore for an estimation of the threshold. The enthalpy margin is defined as the difference between the enthalpy at working temperature of the coil (1.9 K) and the enthalpy at occurrence of a quench:

$$\Delta H = H_{quench} - H_{work}^{1.9K} \tag{3.10}$$

In this study the interesting values are the cable enthalpy margins for the LHC main quadrupole magnet. The magnet cables are shown in figure 2.8 and consist mainly of copper and superconducting filaments of Niobium-Titanium.

The enthalpy for each temperature can be obtained through the specific heat of the materials inside the cables. For the considered limited temperature range, one can assume to a good approximation the equality between the specific heat at constant volume c_v and constant pressure c_p. The specific heat of copper $c_{Cu}(T)$ can be parameterised by [8]:

$$c_{Cu}(T) = \gamma_{e^-} T + \alpha_{Ph} T^3 \tag{3.11}$$

where γ_{e^-} stands for the heat conduction through electrons, α_{Ph} for the conduction through lattice waves (phonons) and T is the temperature. For NbTi the parameterisa-

tion is the following [8]:

$$c_{NbTi}(T) = \gamma_{NbTi}\frac{B}{B_{c2}}T + \alpha_{NbTi}(T_c)T^3 \tag{3.12}$$

where the factor γ_{NbTi} of the linear term is a constant, while α_{NbTi} is depending on the critical temperature T_c. B_{c2} and B are the applied and the second critical magnetic field respectively. The effect of the insulation material in case of transient losses is small and is hence not presented here.

The enthalpy margin is obtained by adding the specific heat of the materials according to their proportions and integrating between the critical temperature and the temperature of the bath.

The exact calculations of the cable enthalpy margins are done with ROXIE [16]. This software enables the detailed modeling of superconducting magnets including the specification of its cable characteristics. Its main purpose is the estimation of important specification of magnets. This is necessary for the design of magnets prior to their construction as well as for quench simulations without damages on the coil. One can for example specify parameters to vary in a predefined way in the simulation, in order to then find the perfect optimisations for the magnet. Sophisticated quench simulations have been programed, where many parameters can be set depending on the given situation [17]. Important examples for those parameters are the time constants of the process(specially interesting regarding fast/slow beam losses), the heat exchange possibilities and the definition of the present quench protection. Moreover different interfaces are enabled. An important one is the possibility of visualising the geometry of the coil as well as the simulation and calculation results.

Through the coupled boundary and finite element method(BEM-FEM), peak fields and forces can be accurately computed [18]. The calculations yield regions with different enthalpy margins, as shown in figures 3.2 and 3.3. The interesting region of the coil is the most exposed one, which is situated on the internal surface, closest to the beam. Lost protons would deposit the highest amount of energy at this location. At the same time one can notice from the figures, that it is also the most fragile region.

For each beam energy in the LHC, the focussing strength of the magnetic field is different and therefore the current in the cables changes respectively. This leads to a corresponding variation of the enthalpy limit. The obtained results for the most exposed region are summarised in table 3.2 and figure 3.4.

The enthalpy margins for different beam energies will later be used to estimate the quench protecting threshold for the BLM system.

Another study about the stability margin of the superconducting magnets for transient heat deposition has been done and its result are discussed in [19].

3.2.2 Steady state quench limit

Earlier presented mechanisms of continuous beam losses imply a heat evacuation from the superconducting magnets, so that their critical temperature is not exceeded. The heat flow in the main magnets of the LHC was analysed through the construction of a Network Model [7], the superconducting cable structure was transformed into a thermal resistance network, which can be seen in figure 3.5. At steady state the limiting

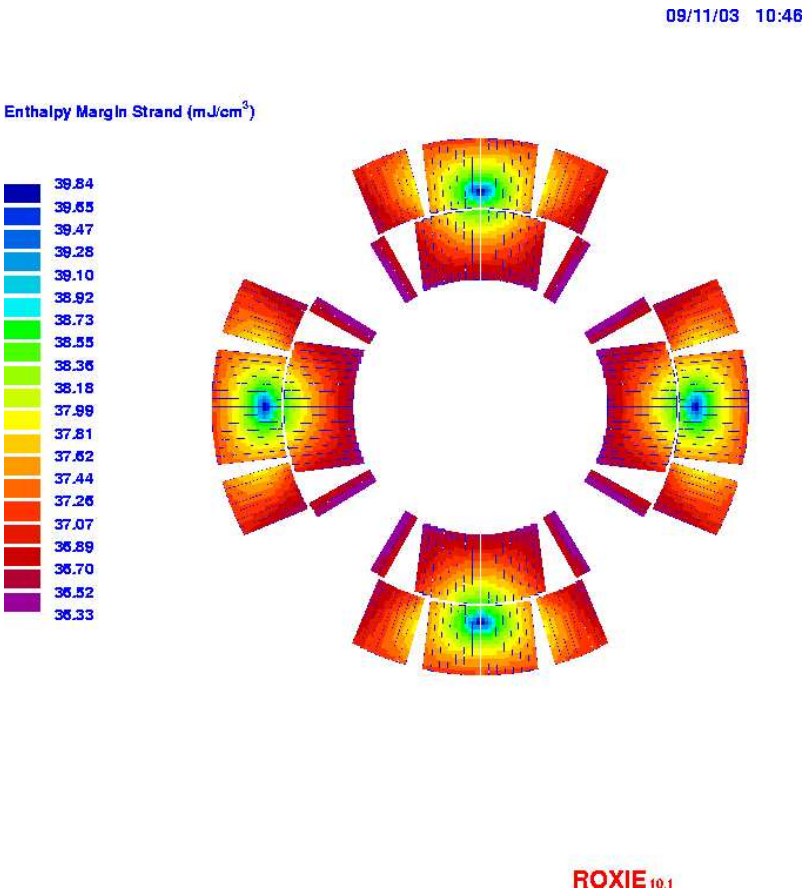

Figure 3.2: MQ Enthalpy margin for 450 GeV cable current

factors for the heat flow are the size of the helium channels and the heat capacity of the cable insulation.

The results from the Network Model simulations for the main quadrupole magnet are of a steady state quench limit of 23 mW/cm^3 for a Gaussian beam loss profile at 7 TeV. Together with assumptions from [8], the quench limit for injection energy was found to of around 48 mW/cm^3. The difference between measurements and simulations did for a majority not exceed 40%.

New not yet published measurements indicate a significant difference between the quench limit at the endings and the middle of the coil. The endings were found to be less sensitive compared to the middle, which is supposed to be due to a lower magnetic field and a better cooling (more helium) at the endings of the magnet [20]. More investigations on this topic needs to be done. For later calculations of the quench protecting threshold this effect is not taken into account. For the safety of the magnets this is not a problem: the beginnings were found to be less sensitive and the resulting thresholds are therefore rather underestimated.

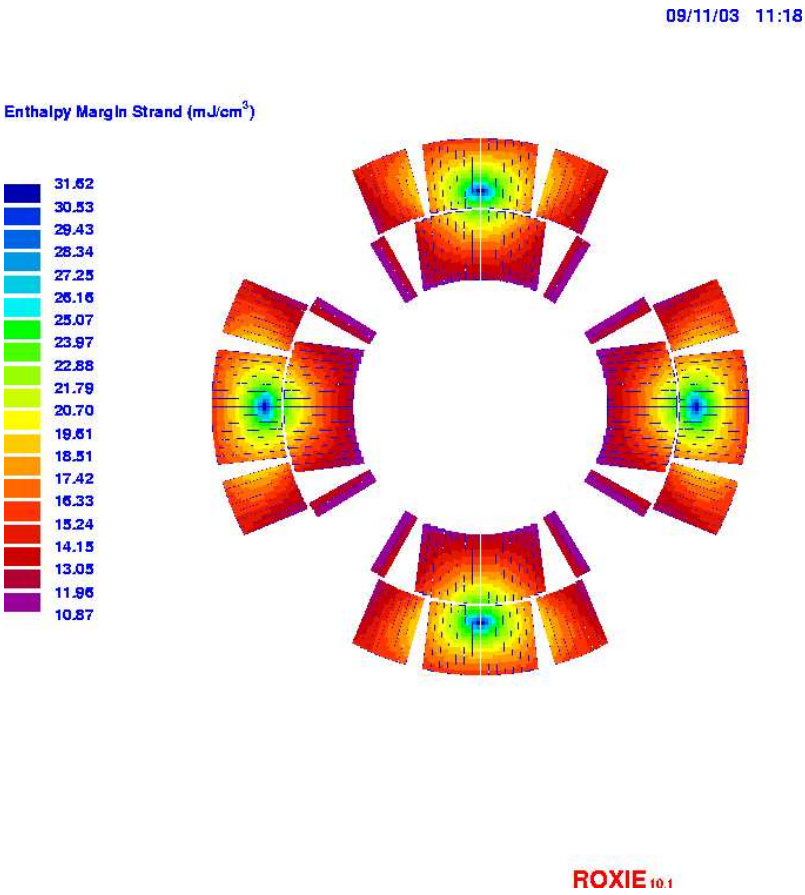

Figure 3.3: MQ Enthalpy margin for 5 TeV cable current

3.3 Loss rates in the interconnection and along MQ

The losses can happen at different places and depending on their location, the energy deposition in the coil can by orders of magnitude, as well as the signal in the BLMs. Therefore it is important to find critical locations and predict a realistic loss pattern, probabilities and weights for the loss locations. That way a representative and realistic threshold can be set.

Losses have been simulated with Geant4 at 14 different locations. This will further be explained in section 5. In order to make general conclusions and to create a realistic scenario, one has to combine the collected information from the Geant4 simulations. This is done by calculating the relative probabilities of the loss locations and then add their results accordingly.

In the following section an attempt has been made to calculate the expected losses caused by beam size variations and therefore predictable through Twiss parameters (definition see section 2.2). In figure 3.6 one can see the evolution of beta and dispersion function through an arc cell. On its top are represented the superconducting magnets. The big squares are the main dipoles, while the small ones are the main quadrupoles. The MQ in the middle of the plot is focussing in the horizontale plane.

To set a safe threshold the worst case LHC arc cell needs to be analysed. Like

Beam Energy [GeV]	Enthalpy limit [mJ/cm^3]
450	36.52
1000	32.12
2000	25.55
3000	20.18
3500	17.86
4000	15.72
5000	11.96
7000	3.44

Table 3.2: Evolution of the enthalpy margin with the beam energy.

that for all other cases the protection will be assured. In the horizontal plane the beta function and the dispersion function take their maximum in a horizontally defocussing quadrupole. The particles will therefore have the highest spread in the middle of MQ, where a major part of the losses is expected. This is the situation that has been simulated with Geant4 and that will be further analysed.

3.3.1 Theoretical estimation from Twiss parameters

The main goal is to estimate the losses from the beam size and the aperture limitations. This can be done using the Twiss Parameters and the situation in the considered MQ is:

1. the betatron function got its maximum in the horizontal plane and its minimum for the vertical one,
2. the dispersion function reaches its maximum in the horizontal plane (in the vertical one no dispersion exists) and
3. the momentum spread x' in the horizontal plane is minimal.

The beam is considered to be Gaussian. Therefore the loss probability density is calculated in a first approximation with:

$$P_{abs}(z) = \int_{r(z)}^{\infty} \frac{1}{\sigma(z)\sqrt{2\pi}} e^{-\frac{x^2}{2\sigma^2(z)}} \mathrm{d}x \tag{3.13}$$

with:

$r(z)$**:** Horizontal aperture dimension at the longitudinal coordinate z

$\sigma(z)$**:** Standard deviation of the Gaussian beam, calculated through the emittance, the energy spread, the dispersion function and the betatron function $\sigma(z) = \sqrt{\beta_x(z)\epsilon + D_x^2(z)\sigma_p^2}$, see section 2.2.

P_{abs} can be translated to the absolute number of lost protons by multiplying the formula by the beam intensity, which corresponds to the initial number of protons N_0.

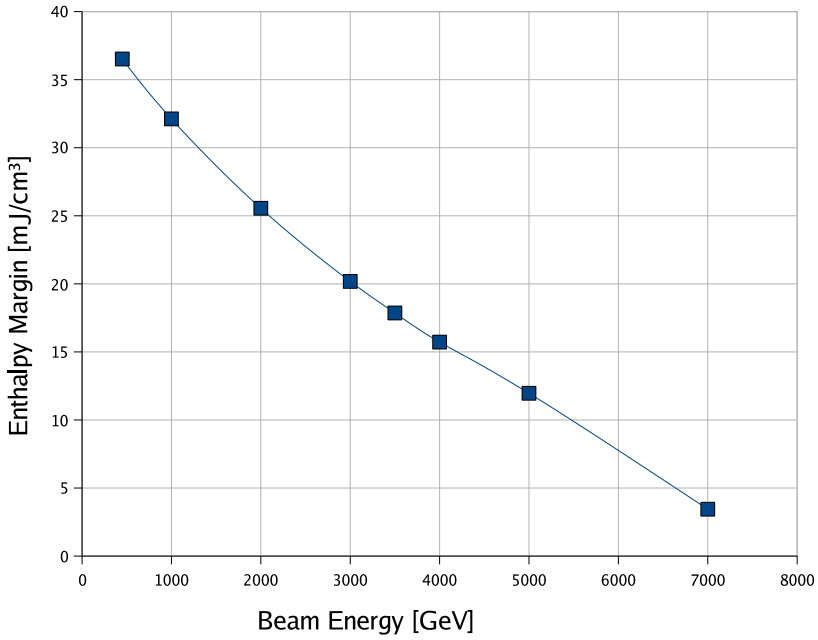

Figure 3.4: Enthalpy margin at the most exposed surface for different beam energies. The non-linearity can be explained by the non-linear dependence of the specific heat on the temperature and the magnetic field(in equation 3.11 and 3.12), and remembering that the critical temperature further depends on the magnetic field.

For the calculations the normalised $\epsilon_n = 3.75\mu m$ has been chosen. This is possible, as we are only interested in relative probabilities and not absolute ones. Besides both emittances are constant over the length of the ring.

In the region of interest(which corresponds to the interconnection including the end of MB and the beginning of MQ) every 10 cm the absolute number of lost protons have been calculated, through the given beam size and the aperture limitations. Then the principle that lost particles can not be lost again has been taken into account by substraction of the calculated losses of the point before, through:

$$N_i = \int_{r_i}^{\infty} N(x)dx - N_{i-1} \tag{3.14}$$

where N_i is the number of lost particles at the i-th loss location and N(x) the particle density in the horizontal plane. A possible re-population from one point to the next still needs to be taken into account.

All the earlier mentioned beam loss mechanisms can cause the re-population of the Gaussian region, where particles were lost already. New losses could then occur. For the LHC the particle diffusion speed away from the core of the beam through regular beam loss mechanisms was estimated to be of the order of 5.3 nm/turn at a dynamical aperture of 6σ [21]. The dynamic aperture is the upper limit for the betatron oscillation amplitude for which the particles of the beam have a stable motion. Protons with motions above this limit are unstable due to magnetic non-linearities. They are lost

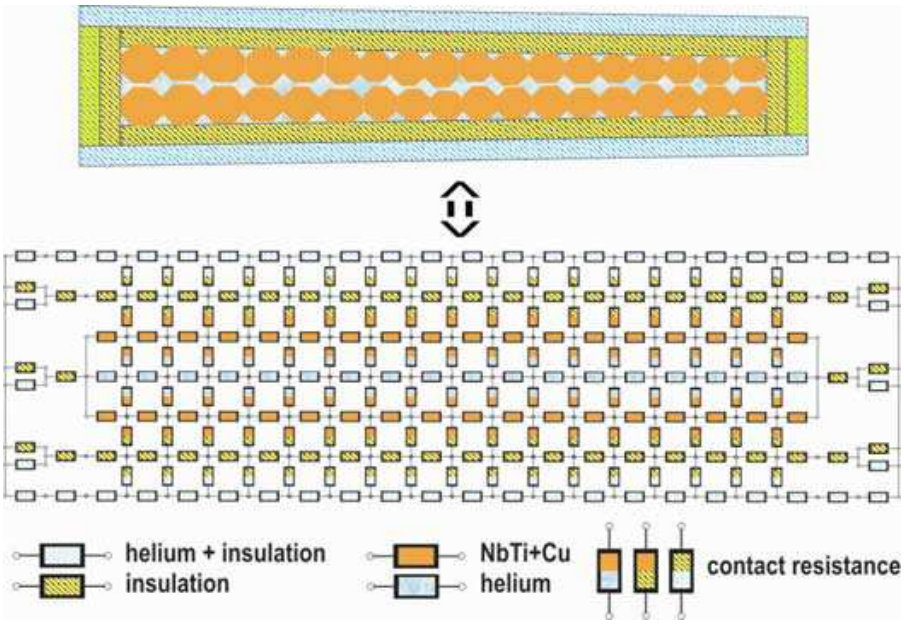

Figure 3.5: Physical model of superconducting cables and its network model equivalent [7].

after a certain number of turns. Ideally the geometrical aperture limitations should be bigger than the dynamic aperture. This is not the case for a nonlinear machine like the LHC with its many high order corrector magnets. Over the considered region of about 6 m this diffusion factor of 5.3 nm/turn is negligible.

A re-population is also possible due to the transverse momentum of the protons and phase advances. First is neglectable, as the betatron function takes a maximum in the middle of the quadrupole and the transverse momentum spread scales approximately with 1/ β. The re-population due to momentum distribution is therefore very small. Second the LHC arc cells contain a FODO lattice with a phase advance of 90°and have a length of 106.9 m [3]. As the studied region is about 6 m long, this effect can be neglected as well. Hence no re-population needs to be taken into account.

The obtained results are plotted in the figure 3.7. The plot shows in red the aperture limitation and in black the relative lost protons for a beam comming from the left side of the plot. One can see the high weight of the region at the beginning of the beam screen for beam losses. This is manly due to the fact, that the radial dimension is reduced with the start of the beam screen. Moreover one can notice that the loss function does not vary much, when the aperture radius is constant. Only a zoom makes the slight change of the function visible. This can be explained by the slow variation of the beta function in the considered region. The BPM tube, with the highest radius, is in the shadow of the Beam screen of MB. Hence no losses are expected in this region, as one can see it in the plot.

Although the beam is generally well approximated as being Gaussian, lost particles are usually not describable by Gaussian statistics. Lost protons come mainly from the halo of the beam, which can not be fully considerated as Gaussian, but has an unknown structure. The loss rates are still important. If normal particles are more probable to

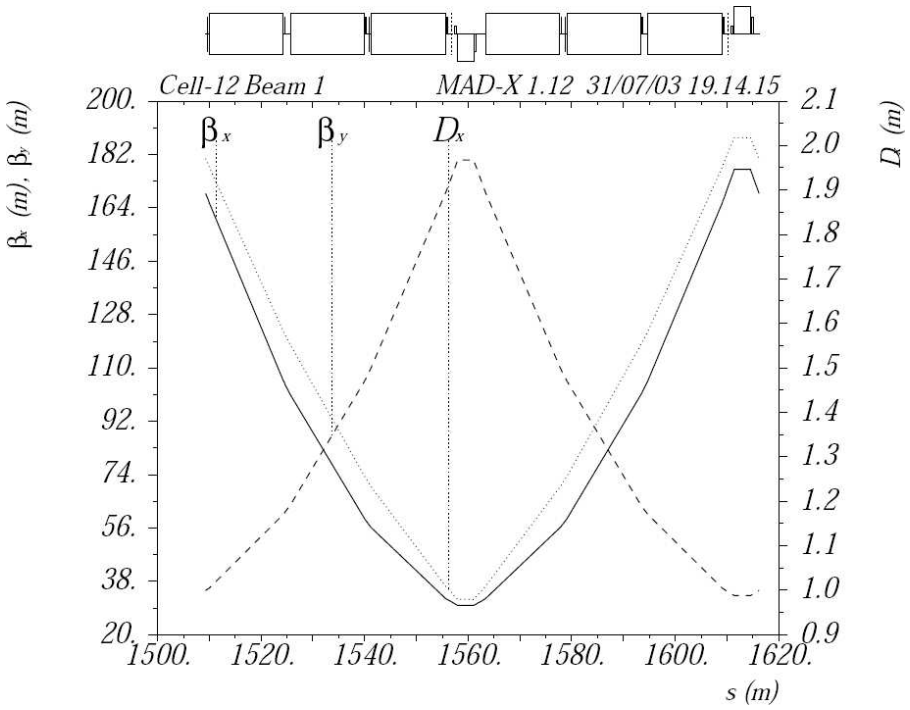

Figure 3.6: Horizontal and vertical beta function and dispersion function for the worst case LHC arc cell [3].

get lost at some points, the particles out of trajectory are also more probably lost at these points (highest beta value and/or aperture limitation).

3.3.2 SixTrack Simulation

In parallel to the theoretical considerations with Twiss parameters, simulations with SixTrack have been done [22]. This program is used to test steady state beam stability in accelerators. Particles are tracked around the ring and their scattering in collimators and movements are recorded. SixTrack takes magnet non linearities to high orders into account and is optimised for fast tracking.

This study is specially interesting, because the information about the location of lost particles is available. A comparison with the earlier made calculations can therefore be done, but conclusions need to be drawn carefully. In the SixTrack simulations losses from the beam halo, hence from off-momentum and off-orbit particles, are considered, whereas for the Twiss calculations one assumed a Gaussian beam. For losses the SixTrack simulations can therefore be considered as more realistic.

The loss rates from the SixTrack simulations at injection energy can be reconstructed and are shown in the figure 3.8. This loss pattern is extremely similar to the one found in simulations made in 2006 [23], only the population of lost protons was smaller. For higher energies the SixTrack simulations were done as well, yet the loss statistics was to low though to deduce the corresponding loss pattern.

Another important result from the simulations was the confirmation that in the arcs vertical losses are less important than horizontal ones. Furthermore no losses

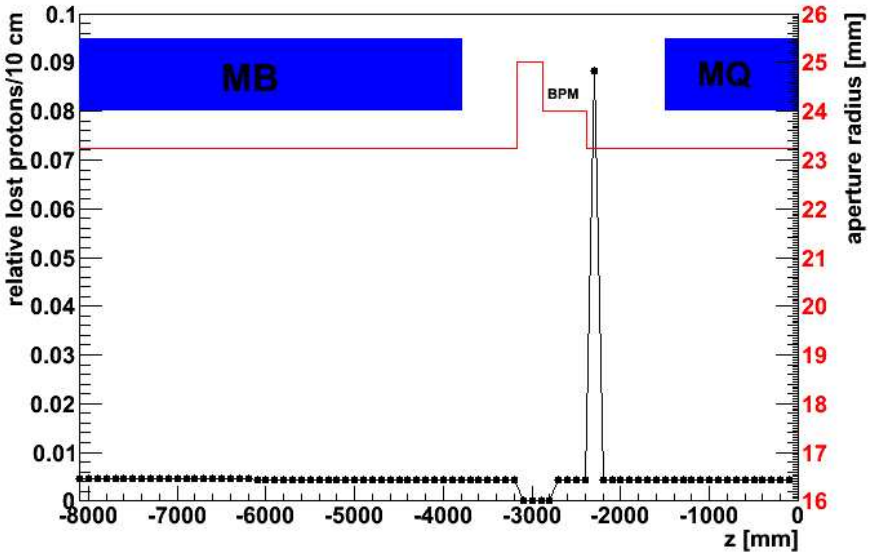

Figure 3.7: Loss rates from Twiss calculations for 450 GeV proton beam parameters. Notice the high peak at the beginning of the beam screen.

were registered after the MQ middle.

3.3.3 Results

Both loss patterns found the maximum to be at the beginning of the beam screen of MQ, which confirms this region to be critical. The threshold should be set with special care to this point. They also agree on the minimum, which is in both cases at the location with highest aperture limits. This is coherent with the expectations, as this region is in the shadow of the beam screen.

The main difference between the calculations with Gaussian beam approximation and the SixTrack simulations is the rise of the loss rates in the MQ middle and end of MB for later one.

The relative lost protons for each loss location of the Geant4 simulations are taken out and normalised so that their sum is one. They will later be used as coefficients for the energy deposition in the coil and the signals inside the BLMs. The final coefficients are in table 3.3.

In order to conclude on the weights each Geant4 loss location should be given, the following algorithm has been used:

$$\omega_i = \frac{1}{\sum\limits_n \omega_n} \int\limits_{x_i - dx_i}^{x_i + dx_i} \frac{dN}{ds} dx \tag{3.15}$$

where the first fraction corresponds to the normalisation of the weights, $\frac{dN}{ds}$ in protons/cm stands for the relative lost protons and is integrated over the bin size used in the histogram.

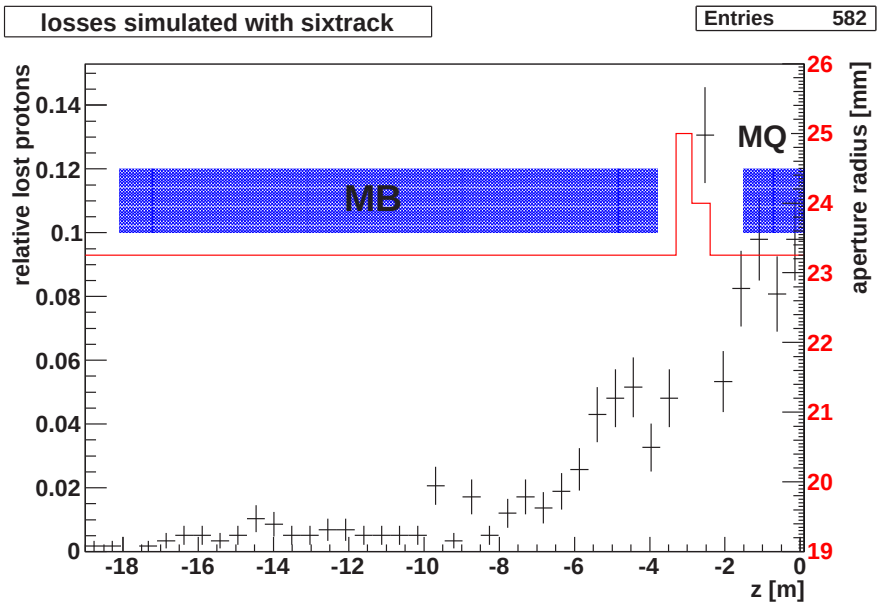

Figure 3.8: Loss rates from SixTrack simulations at injection energy.

3.4 Summary

In this section beam loss mechanisms were discussed. Their contribution to beam life time and emittance growth was explained and quantitative estimations were given.

Further the impact of beam losses on accelerator elements are presented. In particular the amount of energy that can be deposited inside the superconducting quadrupole coil was analysed using ROXIE for the transient case. For injection energy an enthalpy margin of 36.5 mJ/cm^3 was found for the most exposed region, while for collision energy the limit was of 3.44 mJ/cm^3. For steady state losses a heat evacuation capability to the cooling system determines the quench limit corresponding to the critical power density. For injection energy this limit is of 48 mW/cm^3, while for collision energy the critical power density is of 23 mW/cm^3.

Depending on where the beam is lost, its effect on the machinery will be different (this will later be quantified for the interconnection). It is hence crucial to investigate at which locations the protons are more probable to get lost. This was done in detail for the interconnection between the main dipole magnet and the main quadrupole in the short straight section, using calculations through optical Twiss parameters and SixTrack particle tracking simulations. The assumption for the calculations was a Gaussian beam halo, whereas off-momentum and off-orbit particles with an arbitrary halo are tracked in the SixTrack simulations. The two resulting proton impact maps were presented, with the main difference being the expected losses in the middle of the quadrupole coil. The main similarities are that no losses are assumed in the point with the largest aperture and that the maximum of the impacts is expected at the beginning of the beam screen.

loss location z [mm]	Coefficients Twiss [%]	Coefficients SixTrack [%]
-8000	2.03	0.54
-4800	1.96	4.85
-4300	1.96	5.39
-4050	1.95	3.99
-3800	1.95	3.44
-2879	0	0
-2390	76.83	14.11
-1475	1.92	10.24
-1250	1.91	10.34
-1000	1.91	8.62
-750	1.90	8.73
-500	1.90	8.84
-250	1.89	10.45
0	1.89	10.45

Table 3.3: Final coefficients for various loss locations (the same ones will later be used for single proton impact simulations). The observed differences are mainly due to the assumption of the beam halo and the fact that for the SixTrack simulations earlier happenings (e.g. scattering of a proton on a collimator two LHC rounds ago leading to a loss in the interconnection) are taken into account.

Chapter 4

The LHC Beam Loss Monitoring (BLM) system

In order to monitor the beam losses, their evolution and their criticality for surrounding LHC equipment, the Beam Loss Monitoring system has been developed. The system is designed for fastest losses, with a reaction time of about 320 μs, which corresponds to four LHC revolution times. About 4000 detectors have been placed outside the magnet cryostats and measure the radiation of secondary shower particles from lost protons. Should the measured signal exceed a certain threshold, a beam dump is requested to protect sensitive equipment. This threshold needs to be set in a way that a high availability of the LHC for operation is guaranteed. If the threshold is set too low, unnecessary down times are induced by triggering a beam dump, without any potential danger. After the extraction of the beam, the whole system needs a certain amount of time to recover until the next beam can be injected and re-ramped. Is the threshold set too high, superconducting coils can get quenched from beam losses without a reaction of the BLM system. As already mentioned in section 2.4 this has a negative influence on the lifetime of the magnet and the superconducting coil needs ten minutes to two hours for recovery from the normal conducting to the superconducting state. During this time no new beam can be injected.

The placement of the BLMs is critical and needs to be close to where major losses are expected and where the sensitive elements need protection. Typical examples of where losses are expected are the collimator regions and close to the main quadrupole.

Not to underestimate is the role of the BLM system as a fast and accurate indicator for the safe operation of the beam. After injection or in case of unwanted happenings, one immediately sees where losses happen and can adjust the settings accordingly.

The BLM system hence is not only a major protection system, but also a necessary tool in the daily beam operating business.

4.1 Ionisation Chamber

An Ionisation chamber is a particle detector, with a detector gas between electrodes. In an ionisation chamber the applied voltage is of a magnitude that the number of primary created charges is the one collected by the electrodes, without further multiplication. This operational domain of gaseous detectors corresponds to the plateau region[24]

and has the advantage, that slight variations of the applied voltage do not influence the response of the detector. This region can be seen in figure 4.1.

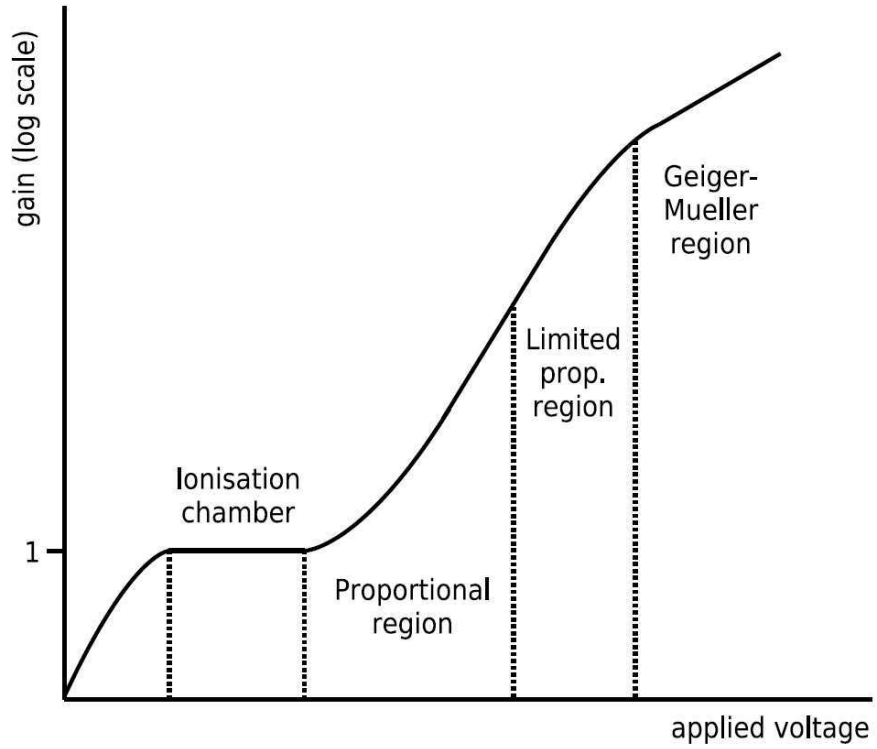

Figure 4.1: The LHC beam loss ionisation chamber.

The main detectors of the BLM system are ionisation chambers. Figure 4.2 shows a picture of the ionisation chamber and in table 4.1 its most important properties are summarised. They are filled with nitrogen N_2 at 100 mbar over pressure. Parallel Al-electrodes inside the detector are under a voltage of 1.5 kV, creating an electric field. The voltage must be high enough to avoid recombination of positive and negative ions [25]. A charged particle entering the BLM ionises the molecules of the filling gas on their way through the chamber. While the released electrons are accelerated towards the anode, the ions are moving to the cathode. A current proportional to energy deposited by the particles can be measured.

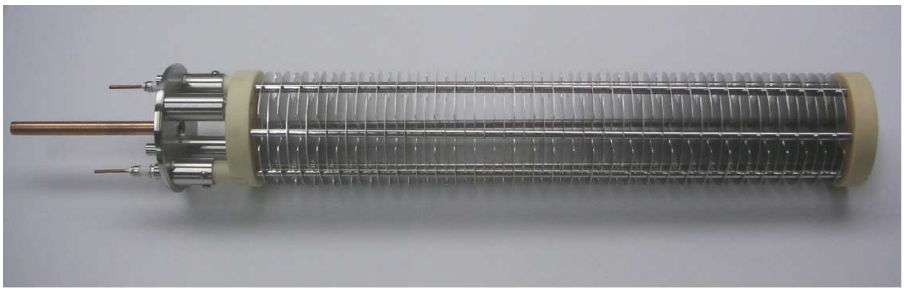

Figure 4.2: The LHC beam loss ionisation chamber.

Property	Value
Detector gas	N_2
Length [cm]	50
Diameter [cm]	8.9
Sensitive volume [l]	1.52
Sensitive volume length [m]	38
Pressure [bar]	1.1
No of electrodes	61
Electrode spacing [mm]	5.75
Electrode thickness [mm]	0.5
Electrode diameter [mm]	75
Standard bias voltage [kV]	1.5

Table 4.1: Properties of the LHC BLM ionisation chamber.

To estimate from the collected charges the energy deposited in the detector, the W-factor was defined. This factor stands for the average amount of energy necessary to create one electron-ion pair.

In order to liberate an electron from its orbit in the molecule a certain energy is needed. For N_2 the first ionisation energy is of about 15.58 eV, whereas its W-factor is around 34.8-36.4 eV[26], slightly depending on the type of particle entering the detector. The W-factor is higher than the needed ionisation energy, as additional loss processes are possible, which do not contribute to ionisation.

The response of the LHC BLM ionisation chambers as a function of particle type, its momentum and incident angle is analysed in [27]. Those response functions are shown in figure 4.3 and will later be very important in order to deduce from the Geant4 particle simulations to the measured BLM signal.

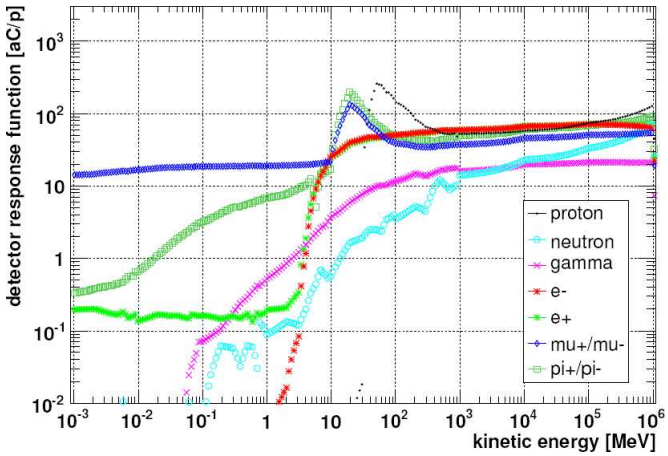

Figure 4.3: BLM response functions for different particle types with an impacting angle of 60° relative to the detector axis [27].

To cover a higher range of energies secondary emission monitors have been developed and installed at points, where higher losses are expected [28].

4.2 Data processing

An overview of the BLM data processing is given in figure 4.4.

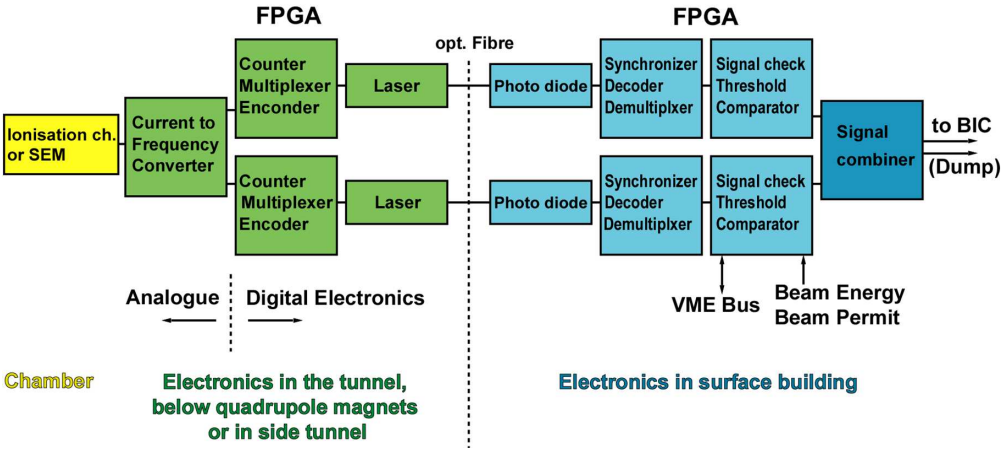

Figure 4.4: Simplified monitor signal chain [29].

Collecting the charges from ionised molecules, the ionisation chamber transforms the energy from particles inside the detector into a signal current. This current is digitalised in the current-to-frequency converter (CFC) [30], which is located in the tunnel and needs to be radiation resistant. Due to the requirements of protecting the LHC superconducting magnets from quenches the upper CFC limit has been set to 23.7 Gy/s. This signifies that for high losses the first running sum (RS, see later) is over the dynamic range with a dose of 948 μGy.

A CFC ASIC (Application Specific Integrated Circuit) is in development [31]. An ASIC is an integrated circuit, designed for a particular application. In the case of the BLM system, it is the digitisation of the output current of the ionisation chambers through a current-to-frequency converter. The increased radiation tolerance of the new design will allow to place the electronic board in the long straight section, where until now long analogue cables are employed. This way the analogue to digital conversion happens at an earlier stage and the cable noise can be reduced.

From the front-end electronics in the tunnel the digital data is proceeded through redundant optical fibers to the surface. Two optical fibers are used for each monitor to ensure the availability and to augment the reliability of the system for the future, knowing that the lasers are the weakest part. In the surface electronics the signal reaches the data acquisition card[1], where it is compared to the security thresholds for beam dumps.

The BLMs need a certain amount of time to collect all the charges and measure the whole dose. Moreover different loss durations and noise considerations have to be taken into account. Hence several time windows, in which the signal gets integrated, are available. Those time windows with their characteristics can be seen in table 4.2.

In Figures 4.5, 4.6 and 4.7 one can see the variation of the collected dose for the nine first RS and for different heights of the signal, in case of instantaneous beam loss.

[1] BLMTC, TC for threshold comparator

Name	Integration Time [μs]	Refreshing rate [μs]	Data type
RS01	40	40	max
RS02	80	40	max
RS03	320	40	max
RS04	640	40	max
RS05	2560	80	max
RS06	10240	80	max
RS07	81920	2560	max
RS08	655360	2560	max
RS09	1310720	81920	sum
RS10	5.24288 s	81920	sum
RS11	20.97152 s	655360	sum
RS12	83.88606 s	655360	sum

Table 4.2: Twelve running sums are available to take into account the different time scales of the losses. Only the first nine are saved in the data base (since the first of April 2010 additionally RS12 is stored in the data base). Data type means that for integration times under a second, the maximum values are saved in the data base, whereas for time windows larger than one second the sum of the 40 μs values in their interval are stored.

This is specially important regarding the information of from when on the entire dose is collected. Furthermore it was feared that for larger time windows the integration of noise could play a major role and overwhelm the signal.

From the plots one can deduce, that for RS03 the full dose has already been collected. For the post-analysis of interesting events this is therefore the one recommended. In the case of very long cables(in section 11R3 the cables are 733 m long) a difference between RS03 and RS04 become noticeable. For those long cables the full dose is hence collected for RS04. The dose collection delay is due to the following effects:

- ion tail: the ions need more time to reach the electrodes than the electrons(the rise time of the signal in the detector is around 100 ns, while the time to collect the ions is of about 100 μs),
- signal pulse broadening in the cables and
- a short-time effect between RS01 and RS02: it is possible that the signal is between two 40 μs time windows and therefore its dose is shared.

RS01 and RS02 are still crucial, as they are the fastest to trigger a dump in case of dangerous losses[2]. For signals over 60 μGy, thus also for critical signals close to the threshold, it was found that the influence of noise integration can be neglected even for large time windows.

[2]In some special cases it can happen, that the threshold is above the saturation level of RS01

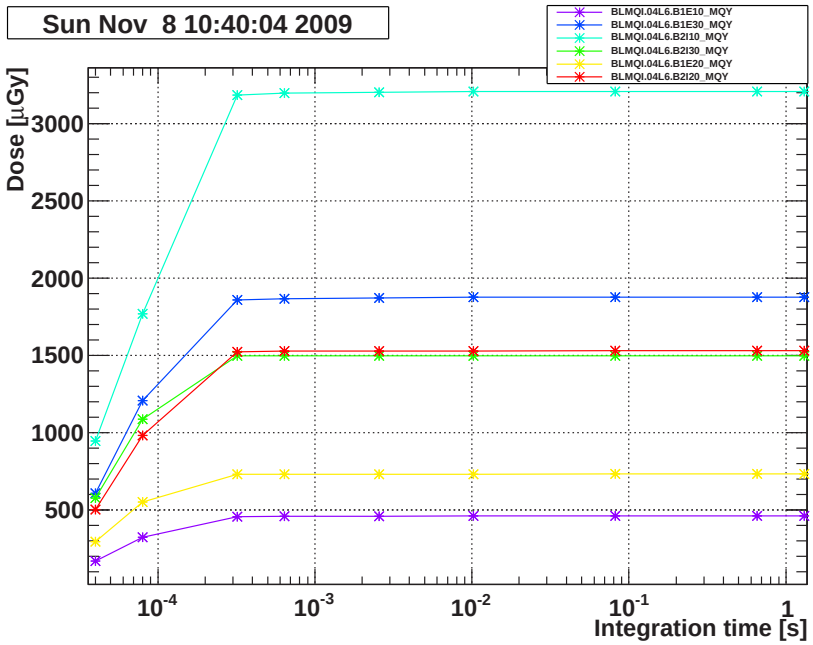

Figure 4.5: Integrated Dose for the first nine RS. For an integration time of 320 μs (RS03) the full dose is reached already. This has been confirmed through a detailed analysis of post mortem data. RS01 is saturated, reaching almost 1000 μGy. Another important information from this plot is that the integration of noise over larger time windows is neglectable for high values.

4.3 Data Contribution to other systems

The BLM measurements are transfered to other systems, needing the information about the losses.

Logging and Measurement Database:

The Beam Loss Monitoring system is publishing data at a frequency of 1 Hz for the measurement database. This is needed for a detailed analysis of the signals and enables the detection of regions with higher losses. For each monitor the maximum value of the last second for the first nine running sums is stored for one week. For permantent storage this data is forwarded through a filter to the logging database. Only the last value in one minute is stored, except for additional storage of values that are above a certain limit, predefined for each running sum. So should the limit not be exceeded, one value per minute is stored. Are some values during the considered minute above the limit, all of them will be stored. Figure 4.8 shows an example of data taken during one second with the different running sums.

All data from the BLMs used in this study is coming from one of those databases. It is therefore important to understand and take into account the data processing and filtering procedures.

Another System to which the BLMs contribute with their data is the **Post Mortem** system [33]. There the detailed data is needed to reconstruct the event leading to a beam or power abort.

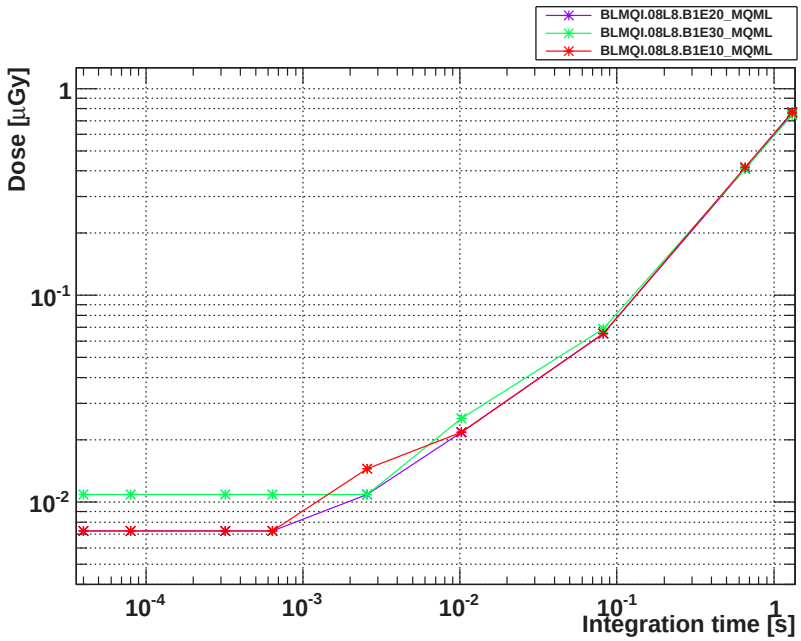

Figure 4.6: Dose for the first nine RS without beam. Offset and noise are integrated and their effect is visible around RS05.

For the **collimation system** the BLM data allows finding the correct positions and improving the beam-based alignment of the jaws.

Furthermore the recorded data will allow an **on line event display** in the Control room, with warnings in case of high losses. The operator will be immediately able to see the beam loss map of the LHC.

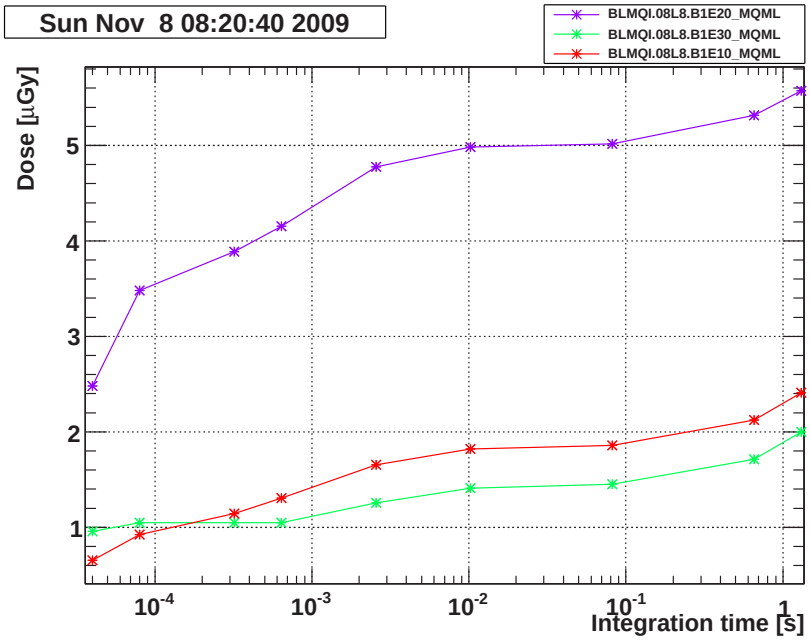

Figure 4.7: Dose for the first nine RS in a situation with little losses. Influence of offset and noise is visible.

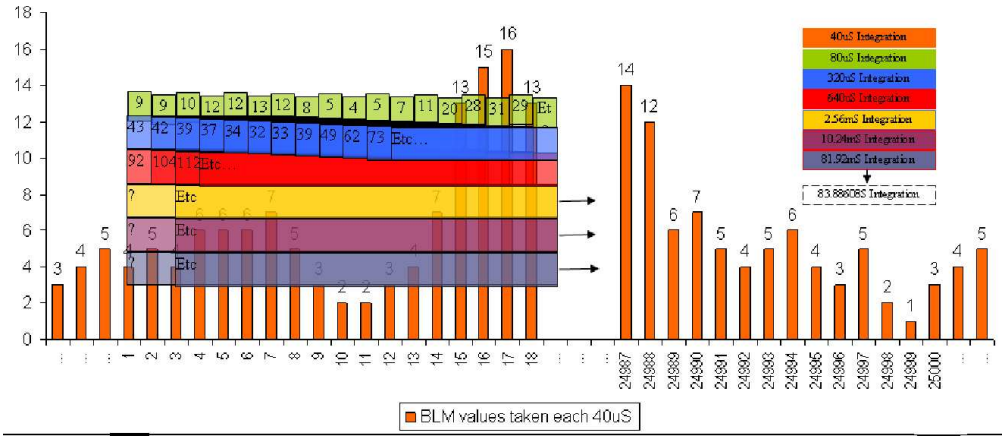

Figure 4.8: Overview and example of the functioning of the running sums during one second (25000 values for 40μs). On the x-axis are the numbers of 40 μs time windows and on the y-axis their corresponding values, with orange bars. In green are the values for the 80 μs time window, in blue the one from 320 μs. The maximum values for each RS are kept in the measurement data base. For the first four running sums those are 16, 31, 73 and 112. All four have a refreshing rate of 40 μs. Courtesy of Stephen Jackson [32].

Chapter 5

Simulation of beam losses

In the past years a lot of effort has been done to develop particle-matter interaction simulations through the Monte Carlo Method. At CERN mainly two applications of this kind are used: FLUKA and Geant4. In this study the simulations have been done with Geant4.

Every modern particle physics experiment is accompanied by extensive simulations. They are used for example to optimise the performance of the detector (positioning of the subdetectors, their properties, setting up the trigger, etc.), to estimate the shape of the backgrounds, to exercise and to perfectionise the reconstruction of expected physical processes.

In case of the study presented here the simulations are used to link the energy deposition inside the coil of the LHC magnets with the signal in the ionisation chambers placed outside the cryostats. The goal of this simulations is to find the value of the signal in the chamber which corresponds to the energy deposition in the coil at which the transition from superconducting to normal-conducting state occurs.

In contrary to simulations of the experiments, this simulations will never be completely validated as the measured signals in the BLMs will not allow to reconstruct precisely the beam loss patterns and material distribution between the loss and the chamber.

In this section first the basics of the simulation technique are explained and then the simulated geometry is described. The main part is a presentation of the simulation results in terms of energy deposition in the coils and signals in the BLMs.

5.1 Monte Carlo method

Monte Carlo method is a computational algorithm based on random sampling of variables characteristic for the investigated process. The method was initially developed to estimate the range of neutrons in the objects (for instance shielding walls) of complex geometry and structure. In these cases findinging the analytic solution was not possible. The correct result has been obtained by simulating the trajectories and interactions of a sample of neutrons. Every time an interaction occurred its parameters (e.g. lost energy, scattering angle) were generated randomly from a known distribution.

The use of the Monte Carlo method in the simulations presented here is a direct heritage of the first problems, for which the method has been developed. The particle

tracking is not limited to neutrons only but any particle type is tracked and corresponding interactions are simulated.

Obviously the method based on multiple calculation of randomly chosen samples can be fully developed on computers. But computers are fully deterministic machines therefore the generation of the values of random variables must be done with use of so called pseudorandom numbers. This numbers are generated by an entirely deterministic causal process, but statistically they approximate the properties of truly random ones.

The pseudo-random number generator usually takes a random number as an input (seed) and based on that it generates the pseudorandom sequence. It is important to say that using the same seed, the same sequences will be obtained. In addition each pseudorandom generator has a period (of millions of generated values). Therefore its use to produce a very large sample might be biased by generating repetitively identical events.

For the simulation of particle interactions the basic principle of the Monte Carlo method can be described by the following steps. First a primary particle is generated with an initial position and momentum. The environment in which the particle will move and interact is called the geometry. The better its characteristics like dimensions, material and density, are defined the more reliable the results will be. Through the whole process the coordinates and momenta of the particles are tracked, as well as those of other particles created due to interaction and decay. This is done until the particle disappears through inelastic processes, leaves the region of interest or until one decides to stop the tracking of the low energy particle through a predefined cutoff energy. At the interaction points the situation has different outcome possibilities with corresponding probabilities. The generated random number then decides on one outcome, taking into account the probabilities. The resulting particles and conditions are again recorded for further processing. This is repeated for all interactions occurring during the simulation and the important information in the regions of interest is saved.

The user typically needs to find the balance between a time consuming simulation and the desired precision, taking furthermore into account the computing limitations.

5.2 Geant4

Geant4 is an application enabling to simulate the passage of particles through matter. It is based on the Monte Carlo method, using object-oriented technology and written entirely in C++ programming language. It is highly flexible and accreditates the user with a lot of freedom and simulation possibilities, being an open source software.

The development of Geant4 was pushed forward due to increasing needs of physicists concerning accuracy, complexity, and sensitivity of the simulated systems. At the same time high-capacity computers enable this development.

Interactions for leptons, hadrons, photons and ions are possible over a high range of energies [34]. Moreover the visualisation of the geometry and particle trajectories is enabled. Interfaces with other software, in this study ROOT, has been foreseen to facilitate later detailed analysis.

The Geant4 software leaves a lot of freedom to the user, who can chose between many different physic models, depending on the wanted accuracy, the available CPU

and the particles and energy ranges expected. In this study the QGSP_BERT_HP physics list has been used, being the one recommended in [27] for those situations. The best description of the hadronic shower shape was found for this list. For high energies, meaning about above 12 GeV the Quark-Gluon String (QGSP) enables the modelling for hadronic interactions, while for energies below 10 GeV the Bertini (BERT) parametrisation of the hadronic cascade is used. The intermediate energy levels have been obtained with the GEISHA parameterisation. Additionally the High Precision (HP) transportation of low energy neutrons, with kinetic energies below 20 MeV, is applied for the Geant4 simulations.

The Geant4 World is the region the programmer needs to define in order to place all the elements of the simulation relative to its centre. For the elements declared as sensitive detectors, the energy density in the bins is saved, so that later analysis is possible.

5.3 Method

Pointlike losses are simulated for 14 different loss locations at injection energy. From section 3.3 one knows that over the considered length around MQ some regions are more critical for potential losses than others. Two loss patterns were discussed: a theoretical one found through Twiss parameters under the assumption of a Gaussian beam and a more realistic one, where the losses come from off-momentum and off-orbit particles. First is referred to as Twiss loss pattern and second as SixTrack loss pattern, according to their origins. While the Twiss loss rates are applicable for all considered beam energies, the SixTrack ones were only found for injection energy. Further simulations were done for higher beam energies. Yet those registered very little loss events and can therefore not be used for conclusions on the loss pattern.

For each loss location one obtains the energy density in the coil, as well as the signal in the BLMs from the Geant4 simulations. From the loss patterns one knows which locations are more critical for losses. The point like losses need to be added up according to the loss pattern. This way a realistic loss scenario is created and its results are obtained.

Inside the arcs of the LHC the dispersion function is zero in the vertical plane, while it reaches its maximum in the horizontal one. This is due to the fact that particles from the same bunch with an energy spread are bent differently, while their passage through the dipole. They hence have a dispersion in the horizontale plane in which they are bent. The assumption of having less losses in the vertical plane is reinforced by the SixTrack simulations, where from 560 loss events in the analysed region only one happend in the vertical direction.

The random seeds for the Monte Carlo procedure are varied between each simulated population of lost protons.

5.4 Interconnection simulations

In Geant4 first a detailed modeling of the coils and the interconnection has been done, in order to later make the wanted simulations and collect their results. In this section

the geometry will be described and then the important information about the circumstances of the simulation will be given.

5.4.1 The Geant4 geometry

In figure 5.1 the LHC interconnection between two main dipoles is shown. The situation is very similar to the one between MB and MQ.

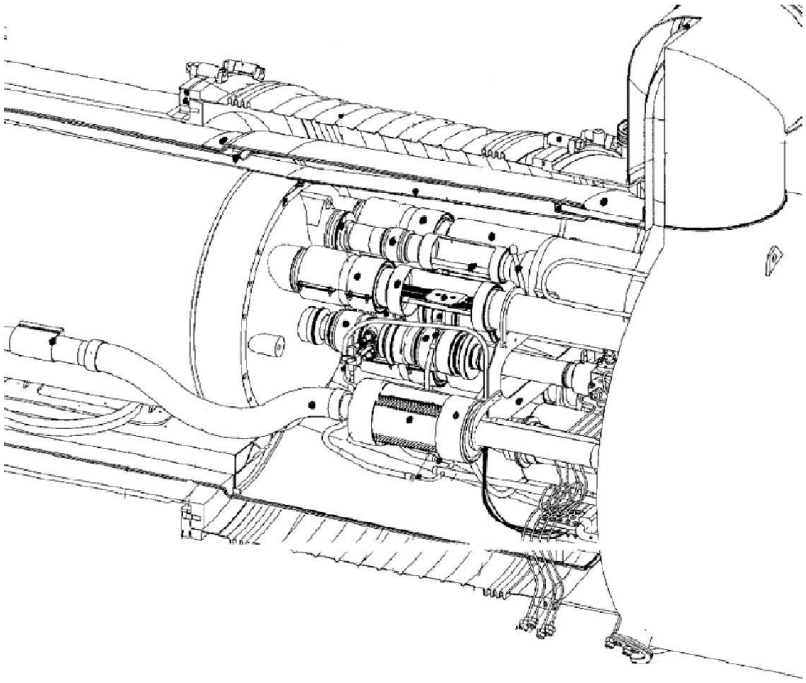

Figure 5.1: Overview of the interconnection between two main dipoles, comparable to the one between MB and MQ. The black dots indicate quality assurance points [3].

The main parts in the geometry of the interconnection are:

- the main quadrupole,
- the main dipole,
- the beam loss monitors,
- the beam screen,
- the LHC tunnel,
- the beam pipe and
- the beam position monitor.

In figure 5.2 the basic geometry is drawn, with its longitudinal dimensions. The aperture limitations for the beam in the interconnection are shown through the cross sections of the beam screen, the beam pipe and the beam position monitor in figure 5.3.

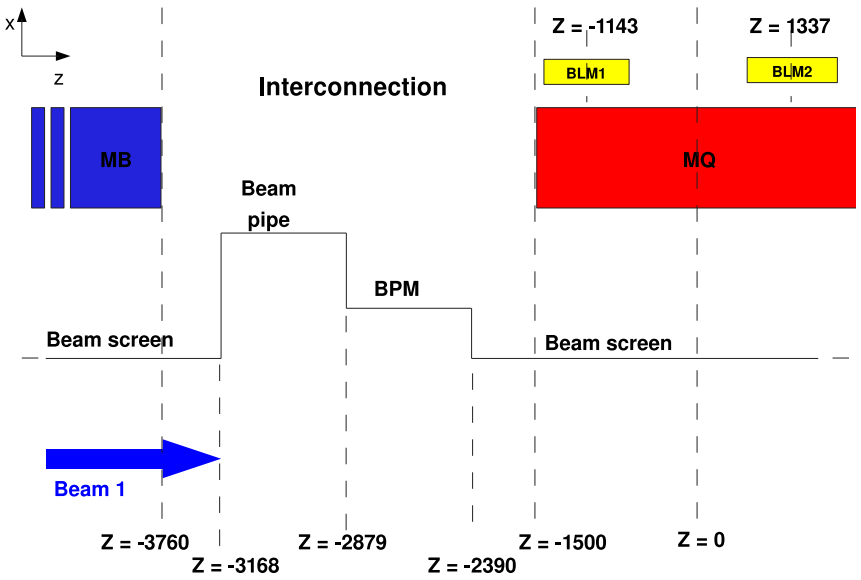

Figure 5.2: Schematic overview of main parts in the interconnection. The middle of the MQ coil's magnetic length corresponds to the zero of the Geant4 world. Dimensions and scales are not respected in this drawing. The unit of the longitudinal coordinate z is mm. In the real machine the edges of the aperture limitations are smoothened to reduce the impedance of the machine and limitate the generation of weak fields, that can provoke beam instabilities.

The following additional features are also implemented among other things: the vacuum vessels, the helium vessels, the iron yoke, the thermal insulation, the superconducting bus bars, the cryostat and some support elements. A detailed view on the Geant4 geometry can be seen in figure 5.4.

The superconducting material was simplified as being a uniform mixture of copper (59.2 %), niobium (19 %), titanium (16.8 %) and liquid helium (5 %). The superconducting quadrupole coil and the bus bars were declared as sensitive detectors, which means the energy deposition in their cells was recorded. For the main quadrupole $3 \cdot 90 \cdot 300 = 81000$ cells were computed. Three for the radial direction, 90 for the angular one and 300 in longitudinal direction. This can be seen in figure 5.5.

The bus bar is responsible for the electrical interconnection. The main bus bar powers MB and MQ, carrying a current of up to 12 kA. They are also made of superconducting material and go through the interconnection. It was feared to be highly exposed to hadronic showers in case of proton losses. Hence it was introduced into the geometry, declared as a sensitive detector and further analysis was done.

The BLMs were implemented in a way to store all particles entering their region with all necessary information to later deduce on the produced signal.

The magnetic field map is 2 dimensional and does not take into account the bending of the magnet cables at the end of the coil. At the endings a simplified smooth decrease to zero of the field was programed instead.

For further information on the geometry also look into [35].

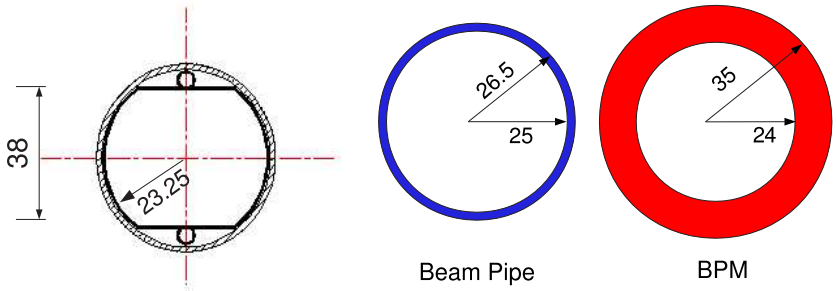

Figure 5.3: In the left picture one can see the cross section of the beam screen, while in the right one is the beam pipe and the beam position monitor. The unit of the dimension is mm.

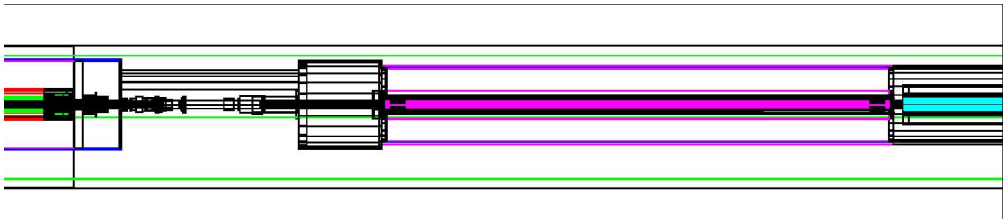

Figure 5.4: Interconnection geometry modeled with Geant4. In this view MB is on the left side, while MQ is on the right one in the pink coloured region.

5.4.2 The simulations

Inside the simulations the following main parameters can be varied: the particle energy and the loss location.

For all the simulations in this study the shooting angle has been kept constant and the particle type of interest is the proton.

Earlier analyses have shown that the signals do not show a high dependence on the angle at which protons are lost [23]. Furthermore it was found that the most realistic loss angle is of 240 μm [36]. This is the one chosen and kept along all simulations.

The LHC has a working range going from a particle energy of 450 GeV to 7 TeV. Those were also the energies used in the simulation.

Two considerations were done concerning the choice of the loss locations: first the aperture limitation. As one expects higher losses at points where the beam encounters a radial restriction, those are important to simulate for a realistic scenario. Second an appropriate density of loss locations. To guaranty reliable conclusions, not only high statistics per loss location are necessary, but also the frequency of those is critical. Due to this argument losses are simulated every 25 cm along the MQ and on the aperture limitation points outside of the MQ region. Losses from MB locations have been added in order to see their influence on the BLM signal, as less shielding is expected through the interconnection. This makes a total of 14 loss locations for injection energy, see table 5.1. Further simulations were done with 2, 3, 5 and 7 TeV. For those less loss locations were simulated and also limited statistics is available, which is simply due to time and computer memory restrictions. Still some conclusions can be made from

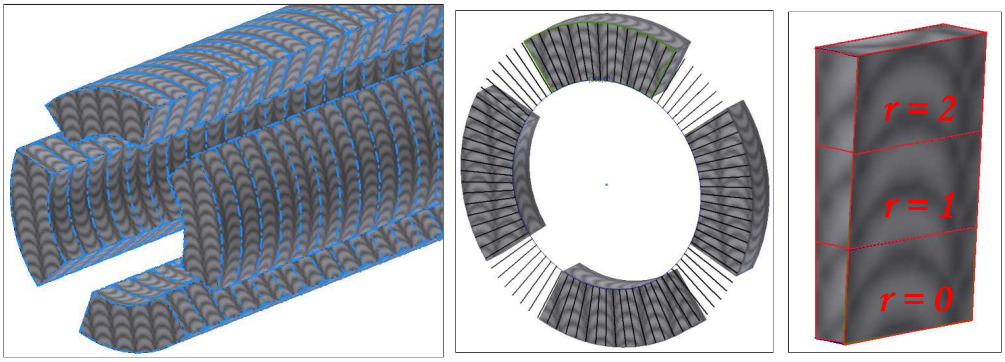

Figure 5.5: On the left one can see the superconducting MQ coil as implemented in the Geant4 geometry. In blue is indicated the longitudinal division into equal bins. The picture in the middle depicts the angular binning and on the right are shown the three radial divisions [35].

those values.

For each loss location and beam energy protons are simulated to get lost in Geant4. Typically 100 protons are shot in one simulation.

The most important outputs from the Geant4 simulation are: the energy deposition and its location inside the coil as well as type, angle, position and energy from the particle entering the BLMs. Those values enable later to compare the energy in the coil with the signal inside the BLM in order to set the thresholds.

		Number of protons		
loss location [mm]	horizontal/vertical	at 450 GeV	at 5 TeV	at 7 TeV
-8000	h	500	0	0
-4800	h	500	0	0
-4300	h	500	0	0
-4050	h	500	0	0
-3800	h	500	500	0
-2879	h	500	300	80
-2390	h	5500	1500	550
-1475	h	500	500	60
-1250	h	500	500	80
-1000	h	500	500	80
-750	h	500	500	80
-500	h	500	500	60
-250	h	500	500	100
0	h	700	500	40

Table 5.1: Loss locations and simulation statistics for 450 GeV, 5 TeV and 7 TeV protons.

5.5 Energy deposition in the coil

An essential information from the Geant4 simulations to allow further conclusions is where and how much energy got deposited in the coil. Knowing the energy density in the superconducting magnet, it is possible to calculate how far the situation is away from endangering the correct functioning of the superconducting coil. An estimation of the critical number of protons until a quench occurs can be given.

In figures 5.6 and 5.7 one can see the most exposed cross section of the MQ for two different loss locations. Noticeable is that for loss locations inside MQ the energy density deposition is more located and also higher, whereas for loss locations outside of MQ the energy density deposition spread is larger and the maximum is lower. The first radial bin in the horizontal plane in the direction of the losses is the most exposed one.

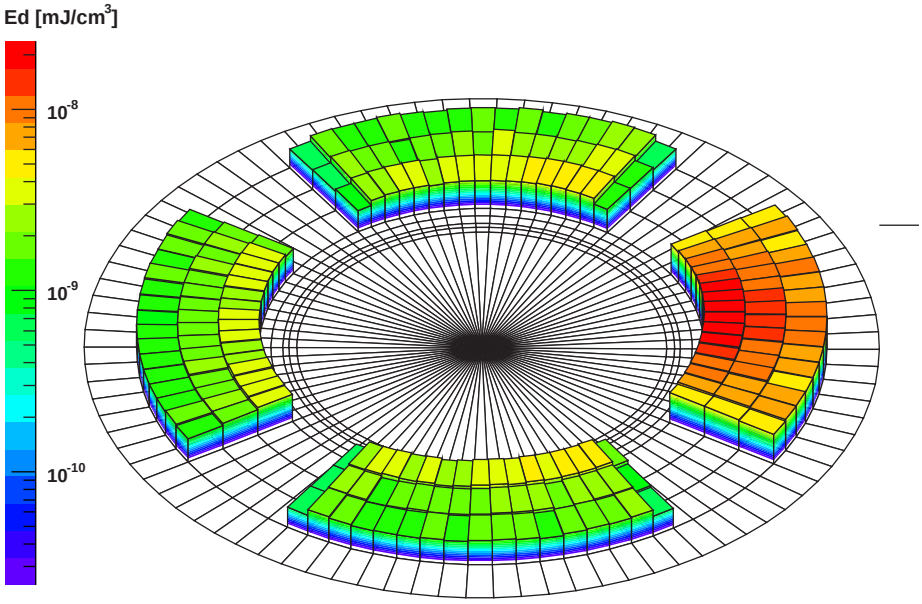

Figure 5.6: Energy density in the most exposed cross section of the quadrupole coil from a 450 GeV proton lost at the beginning of beam screen at z = -2390 mm.

5.5.1 Linear Interpolation

Finding the point where the highest amount of energy is expected to be deposited after a realistic loss is crucial, as the threshold should be set for the most sensitive region in order to protect from quenches. The realistic loss can be constructed through a longitudinal linear interpolation between the pointlike losses together with the already mentioned loss patterns.

For the detection of the most exposed point in longitudinal direction, one needs to combine the energy deposition from each loss locations with the coefficients from

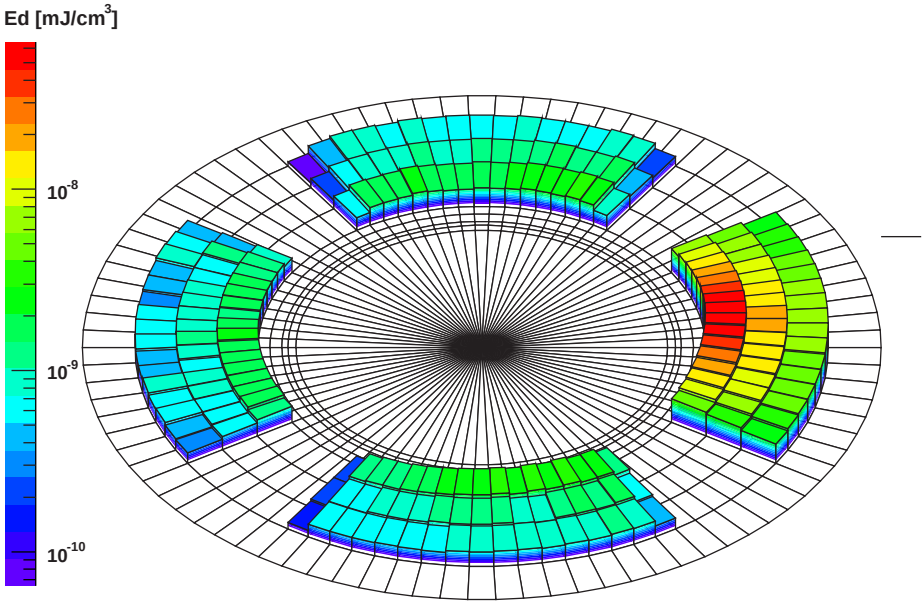

Figure 5.7: Energy density in the most exposed cross section of the quadrupole coil from a 450 GeV proton lost in the middle of MQ at z = 0 mm.

Twiss calculations and SixTrack simulations. That way two loss scenarios are created and can later be compared.

In figure 5.8 one can see the individual energy density distributions of each loss location for the first layer and the most exposed azimuth of the coil. The middle of MQ corresponds to z = 0. The maximum of the energy density deposition in the coil is situated about 25 cm after the point where the losses were simulated. The simulations that had their loss locations at the outside of the MQ have their maximum right at the beginning of the coil. The farther away the loss location from the coil, the lower the maximum energy density deposition.

As has been shown in the earlier section, each location has its probability so that the individual energy density distributions have been multiplied by the corresponding coefficient and added up. The loss locations at the MQ region are 25 cm distant from each other. This distance was chosen because the width of the curves in figure 5.8 20% underneath the peak is of about 25 cm. In order to augment the precision and smoothen out statistical variations, averaged curves are calculated every 5 cm between the loss locations. This is achieved by taking into account the distances from the two closest loss locations. The closer it is to one loss location, the more its shape is similar to the energy density distribution of the closest point. This is done through the coefficients:

$$k_1 = \frac{d_2}{d_1 + d_2} \tag{5.1}$$

and

$$k_2 = \frac{d_1}{d_1 + d_2} = 1 - k_1 \tag{5.2}$$

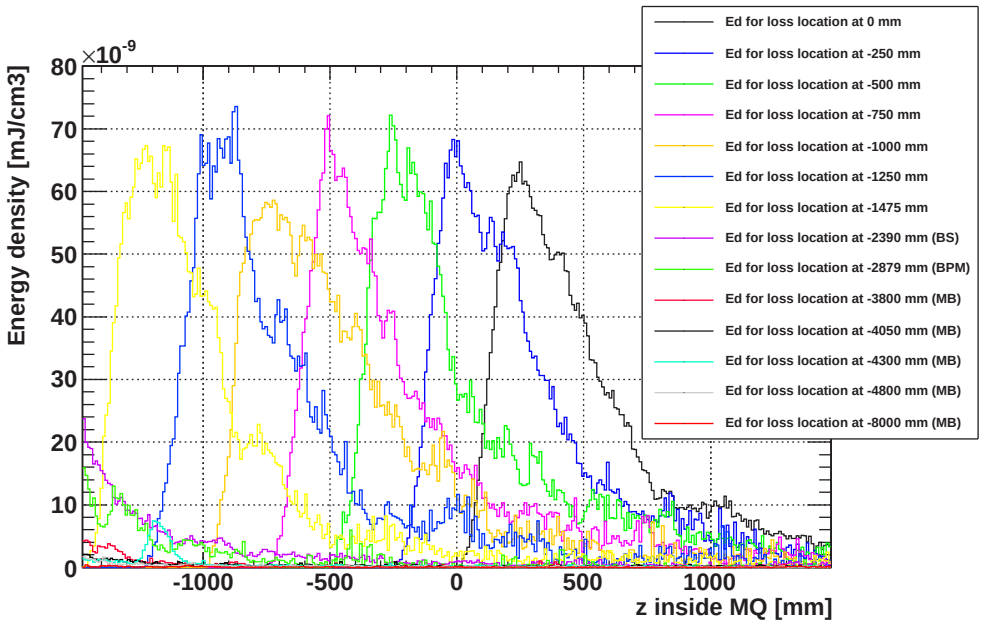

Figure 5.8: Energy density per proton in the MQ coil inner layer for the most exposed azimuth for different loss locations.

with:

d_1: Distance between the first loss location and the point at which the new curve is constructed

d_2: Distance between the second loss location and the point at which the new curve is constructed

k_1, k_2: Coefficients for the energy density distribution curve of the first and second loss location respectively

The results of this procedure will further be discussed.

5.5.2 Radial energy deposition

From the Geant4 simulations one now knows the energy density deposition in the single bins of the coil. Of interest is the value for the inner most exposed surface, which is the highest and should hence enable the calculation of a safe threshold. An analysis of the radial dependency of the energy density in the coil for the most exposed cross section has been done. As the transversal energy spread in the coil is depending on the location of the lost protons, this analysis needs to be done separately for the locations inside and outside the coil.

The highest energy density deposition is on the inner surface of the quadrupole coil. Through the simulations one can only see the average energy density over the distance of the first bin. To be able to find a reliable threshold, the radial energy deposition is analysed, hence the change between the inner surface and the three radial

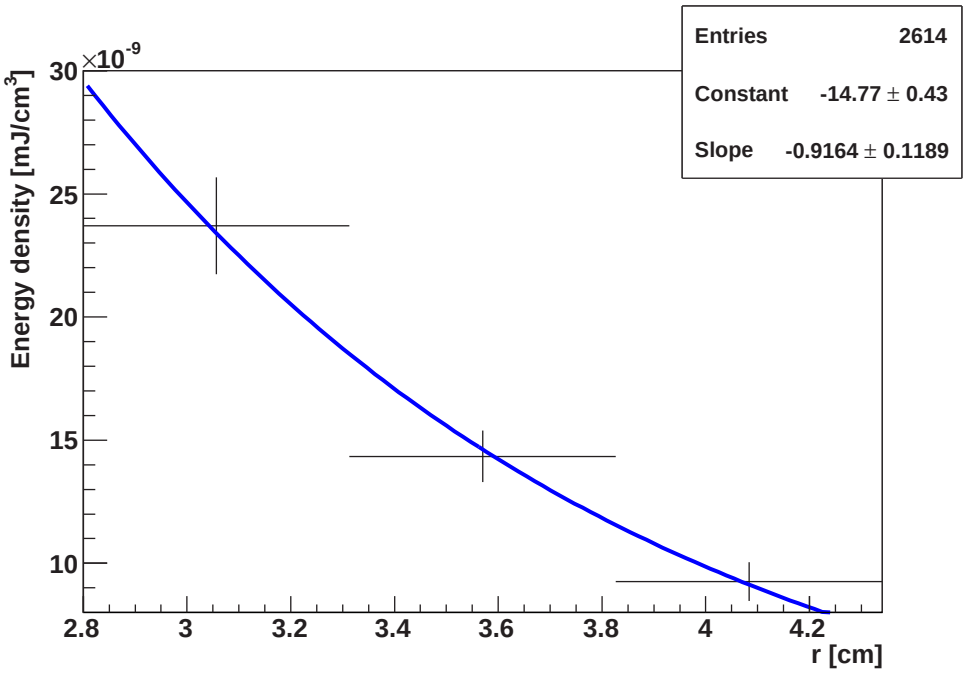

Figure 5.9: Energy density deposition in the coil at the most exposed region as a function of the bins in radial direction from a 450 GeV proton lost outside of MQ.

bins. The exponential fitting for the situation of losses outside and inside of the coil can be seen in figures 5.9 and 5.10 respectively. The used fitting function is:

$$E_{Dens}(r) = e^{a+br} \tag{5.3}$$

$E_{Dens}(r)$ is the energy density deposition, r is the radius, a is the fitting constant and b the slope.

The maximal energy density deposition in the first layer of the coil from a 450 GeV proton lost at the beginning of the beam screen is of $2.37 \cdot 10^{-08}$ mJ/cm^3, while the fitting provides a value of $2.96 \cdot 10^{-08}$ mJ/cm^3 on the inner surface. This leads to a ratio of 1.247 and corresponds to an augmentation of 24.7%.

The same is done for 450 GeV protons lost in the region of MQ and leads to an augmentation of 69% from the value recorded in the first bin to the inner surface of the coil.

The values for all considered beam energies are summarised in table 5.2. The losses happening before MQ have a more flat radial distribution than the ones happening inside the coil. Also the shower is more narrow for higher proton energies, which makes the radial augmentation more pronounced for higher energies.

5.5.3 Results

Figure 5.11 represents the energy density distribution per proton from the Twiss loss scenario. Comparing this graph with the one in figure 5.8, one can see the high weight of the loss location at the beginning of the beam screen at z = -2390 mm. The maxi-

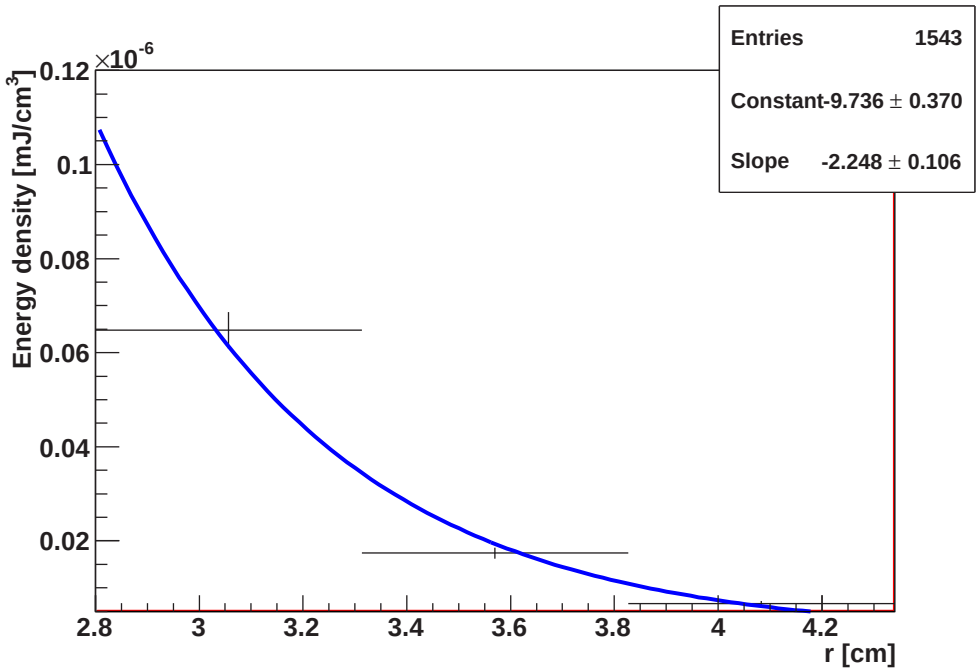

Figure 5.10: Energy density deposition in the coil at the most exposed region as a function of the bins in radial direction from a 450 GeV proton lost in the middle of MQ.

	Radial Augmentation [%] at		
Protons lost	450 GeV	5 TeV	7 TeV
before MQ	25	32	39
inside MQ	69	73	80

Table 5.2: Radial Augmentation of the maximum energy density deposition from the first bin to the inner surface of the coil for different beam energies.

mum energy density deposition is at the beginning of the superconducting coil and its value is $1.92 \cdot 10^{-08}$ mJ/cm^3.

For the SixTrack proton loss scenario the maximum energy density deposition is of $1.75 \cdot 10^{-08}$ mJ/cm^3 and located 30 cm after the beginning of MQ, see figure 5.12.

The following equation describes the relation between the calculated energy density deposition of an average lost proton and the simulated energy density deposition of one proton per loss location.

$$\int_{MQ} \overline{E_D(z)}\mathrm{d}z = \sum_{i=0}^{N} c_i \int_{MQ} E_{D_i}(z)\mathrm{d}z \tag{5.4}$$

with:

$\overline{E_D}$**:** Energy density deposition in the quadrupole coil of the average lost proton

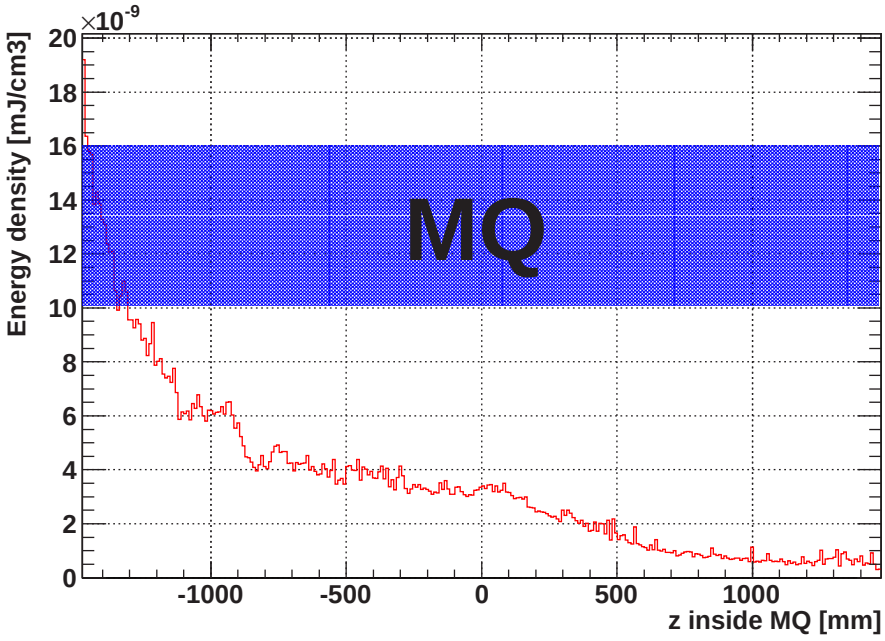

Figure 5.11: Energy density of the most exposed azimuth per proton after the weighted averaging for the Twiss loss pattern.

N: Number of simulated loss locations

E_{D_i}: Energy density deposition in the quadrupole coil of one proton lost at the ith loss location

c_i: weights for the loss locations

This means the total energy density deposition of the average lost proton is the same as the average energy density deposition of the separate protons, where the loss rates c_i have been taken into account.

The final results that take the radial augmentation into account, are summarised in table 5.3 for injection energy, in table 5.4 for 5 TeV and in table 5.5 for collision energy.

Knowing the maximum energy density deposition E^D_{max} per proton and the enthalpy limit H_{limit} of the coil (see section 3.2.1), one can calculate the critical number of protons $N_{critical}$ until a quench occurs:

$$N_{critical} = \frac{H_{limit}}{E^D_{max}} \tag{5.5}$$

For protons at 450 GeV the enthalpy limit is of 36.52 mJ/cm^3. Should the particles be lost according to the Twiss loss pattern, a critical number $N_{critical}$ of $1.52 \cdot 10^9$ protons would quench the main quadrupole magnet, depositing an average energy density of $2.40 \cdot 10^{-8}$ mJ/cm^3 per 450 GeV proton. Should instead the protons be lost according to the SixTrack loss pattern, a critical number $N_{critical}$ of $1.23 \cdot 10^9$ protons would

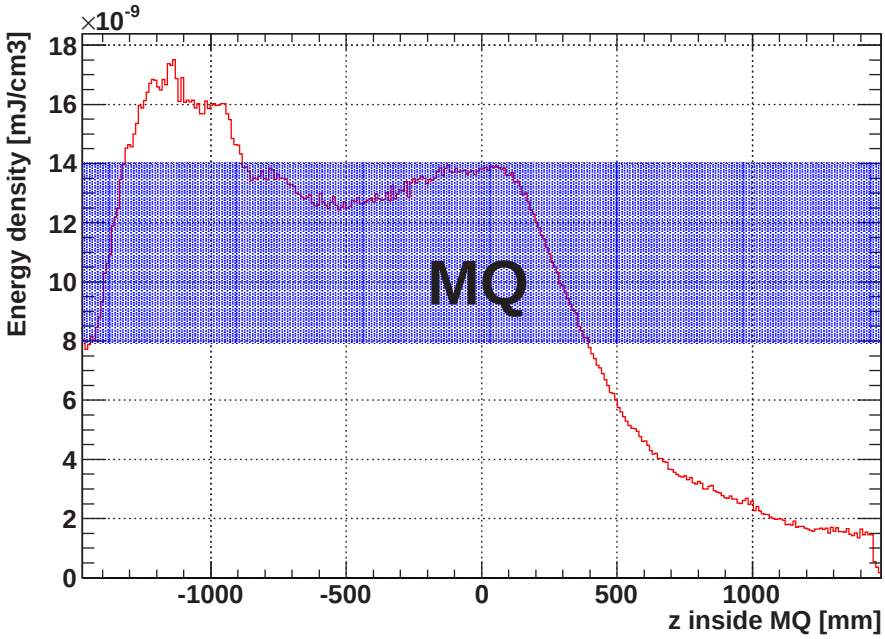

Figure 5.12: Energy density of the most exposed azimuth per proton after the weighted averaging for the SixTrack loss pattern.

quench the main quadrupole magnet, depositing an average energy density of $2.98 \cdot 10^{-8}$ mJ/cm^3 per 450 GeV proton.

The dependence of the energy density deposition in the superconducting coil from the beam energy is shown in figure 5.13 together with the linear regression curve and its equation.

5.5.4 Steady state case

While for transient losses the important parameter is the maximum energy density deposition inside the coil, the criteria for steady state losses is the power density, as heat exchange with the Helium cooling system needs to be taken into account. A method to deal with steady state losses is to take the averaged energy density from the entire thermal equilibrium volume of the superconducting cable [37]. Together with the power that can be dissipated before a quench [7] presented in section 3.2.2, this leads to the number of protons which can be lost locally per second:

$$\dot{n_q} = \frac{w_q}{E_{D,cable}} \tag{5.6}$$

where $\dot{n_q}$ is the quench limit in protons per second, w_q is the quench margin defined by the heat transmission capability and $E_{D,cable}$ is the energy density deposition in the cable. The critical power density before the occurrence of a quench is of 23 mW/cm^3 at collision and around 48 mW/cm^3 at injection energy.

The number of 450 GeV protons $\dot{n_q}$ that can be lost per second until a quench occurs is of $3.30 \cdot 10^{10}$ according to the Twiss loss pattern, while the one from SixTrack

loss location [mm]	E^D_{max} [mJ/cm^3]	No of critical protons
point losses:		
-8000	$1.40 \cdot 10^{-9}$	$2.60 \cdot 10^{10}$
-4800	$7.57 \cdot 10^{-9}$	$4.83 \cdot 10^{9}$
-4300	$8.06 \cdot 10^{-9}$	$4.53 \cdot 10^{9}$
-4050	$5.35 \cdot 10^{-9}$	$6.83 \cdot 10^{9}$
-3800	$8.00 \cdot 10^{-9}$	$4.56 \cdot 10^{9}$
-2879	$1.99 \cdot 10^{-8}$	$1.84 \cdot 10^{9}$
-2390	$2.96 \cdot 10^{-8}$	$1.23 \cdot 10^{9}$
-1475	$1.16 \cdot 10^{-7}$	$3.14 \cdot 10^{8}$
-1250	$1.03 \cdot 10^{-7}$	$3.56 \cdot 10^{8}$
-1000	$9.85 \cdot 10^{-8}$	$3.71 \cdot 10^{8}$
-750	$1.23 \cdot 10^{-7}$	$2.98 \cdot 10^{8}$
-500	$1.23 \cdot 10^{-7}$	$2.98 \cdot 10^{8}$
-250	$1.16 \cdot 10^{-7}$	$3.14 \cdot 10^{8}$
0	$1.10 \cdot 10^{-7}$	$3.32 \cdot 10^{8}$
loss patterns:		
Result Twiss	$2.40 \cdot 10^{-8}$	$1.52 \cdot 10^{9}$
Result SixTrack	$2.98 \cdot 10^{-8}$	$1.23 \cdot 10^{9}$

Table 5.3: Maximal energy density deposition per 450 GeV proton for the simulated loss locations. The radial augmentation has been taken into account.

loss location [mm]	E^D_{max} [mJ/cm^3]	No of critical protons
point losses:		
-3800	$6.63 \cdot 10^{-8}$	$1.80 \cdot 10^{8}$
-2879	$3.01 \cdot 10^{-7}$	$3.97 \cdot 10^{7}$
-2390	$4.03 \cdot 10^{-7}$	$2.97 \cdot 10^{7}$
-1475	$1.21 \cdot 10^{-6}$	$9.90 \cdot 10^{6}$
-1250	$1.21 \cdot 10^{-6}$	$9.85 \cdot 10^{6}$
-1000	$1.25 \cdot 10^{-6}$	$9.59 \cdot 10^{6}$
-750	$1.18 \cdot 10^{-6}$	$1.01 \cdot 10^{7}$
-500	$1.19 \cdot 10^{-6}$	$1.00 \cdot 10^{7}$
-250	$1.17 \cdot 10^{-6}$	$1.02 \cdot 10^{7}$
0	$1.24 \cdot 10^{-6}$	$9.68 \cdot 10^{6}$
loss pattern:		
Result Twiss	$3.43 \cdot 10^{-7}$	$3.48 \cdot 10^{7}$

Table 5.4: Maximal energy density deposition per 5 TeV proton for the simulated loss locations. The radial augmentation has been taken into account.

is of $2.61 \cdot 10^{10}$. The number of 5 TeV protons $\dot{n_q}$ that can be lost per second according to the Twiss loss pattern until a quench occurs is of $2.73 \cdot 10^{8}$.

For the main dipole magnet another more precise and complex method was developed to estimate the steady state quench limit. In this newer method the heat distribu-

loss location [mm]	E^D_{max} [mJ/cm^3]	No of critical protons
point losses:		
-2879	$4.42 \cdot 10^{-7}$	$7.79 \cdot 10^6$
-2390	$5.97 \cdot 10^{-7}$	$5.77 \cdot 10^6$
-1475	$1.81 \cdot 10^{-6}$	$1.90 \cdot 10^6$
-1250	$1.62 \cdot 10^{-6}$	$2.13 \cdot 10^6$
-1000	$1.84 \cdot 10^{-6}$	$1.87 \cdot 10^6$
-750	$1.86 \cdot 10^{-6}$	$1.85 \cdot 10^6$
-500	$1.69 \cdot 10^{-6}$	$2.03 \cdot 10^6$
-250	$1.93 \cdot 10^{-6}$	$1.78 \cdot 10^6$
0	$1.95 \cdot 10^{-6}$	$1.77 \cdot 10^6$
loss pattern:		
Result Twiss	$4.99 \cdot 10^{-7}$	$6.90 \cdot 10^6$

Table 5.5: Maximal energy density deposition per 7 TeV proton for the simulated loss locations. The radial augmentation has been taken into account.

tion inside the coil was taken into account [20]. Both approaches were compared and it was found that they lead to very similar results [38].

From the Geant4 simulations one obtains the values summarised in table 5.6, 5.7 and 5.8, for injection energy, 5 TeV and collision energy respectively. As those values correspond to an average of energy deposition, they are lower than those for transient losses, where the absolute maximum was of interest. Noticeable is furthermore that the difference between loss locations from outside of the coil and those from its inside is smaller than in the case of transient losses. This is due to the larger spread of the hadronic shower for losses coming from before the coil (see also figures 5.6 and 5.7). Is the spread still small, the first bin in radial direction will have much larger values than the others and an averaging over the bins will lower the energy deposition. For a larger spread the bins will have a similar amount of energy deposited and the difference will hence be smaller. This can be observed comparing the values from loss locations -2390 and -1475 in tables 5.6 and 5.3.

The energy density deposition in the cable depends linearly from the beam energy as shown in figure 5.14.

5.5.5 Error estimation

The procedure to obtain the maximum energy density deposition has different error sources:

- a systematic one, due to the errors in the fitting function,
- a statistical one, due to a limited number of loss events and loss locations and
- other systematic errors, neglected here, due to accuracy of physics description and geometry of the region.

To analyse the radial energy augmentation, an exponential fitting was used. The errors of the fitting parameters σ_a and σ_b are known and depicted in figures 5.9 and

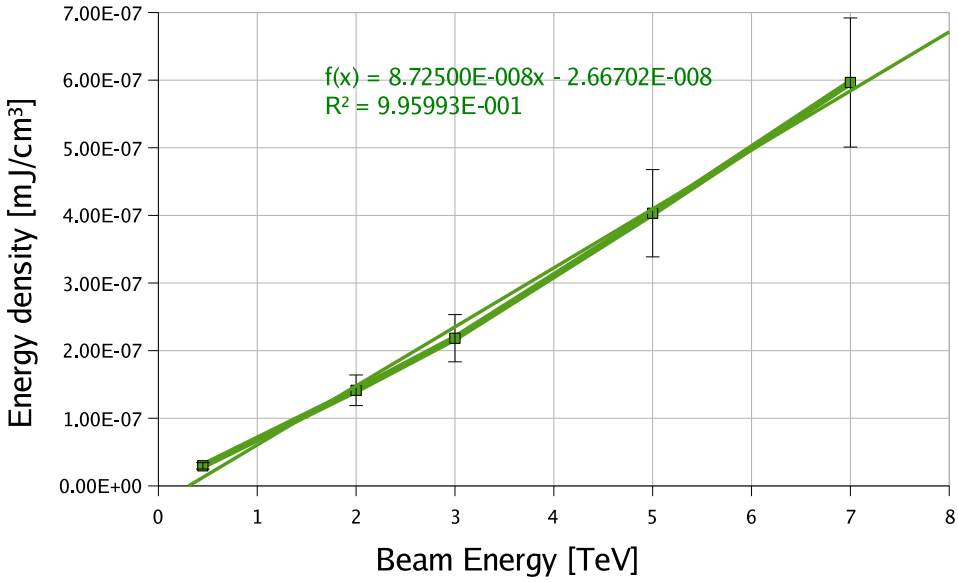

Figure 5.13: Maximum Energy density per proton as a function of the beam energy for the loss location at the beginning of the beam screen. R is the correlation coefficient, giving a measure of the reliability of the linear relationship. The closer R is to one, the better the linear regression describes the data.

5.10, where a corresponds to the constant and b to the slope. The expected energy density deposition E_1 is calculated with the fitting parameters a and b:

$$E_1 = e^{a+br} \tag{5.7}$$

The largest energy density deposition E_2 calculated with the extrema of the fitting parameters $a + \sigma_a$ and $b + \sigma_b$ is:

$$E_2 = exp((a + \sigma_a) + (b + \sigma_b)r) \tag{5.8}$$

The comparison between E_1 and E_2 leads to a relative error $\sigma_E^{fitting}/E$ of 9.0% for loss locations outside the coil and 8.6% for inside MQ.

Additionally for each loss location a different radial energy density augmentation ΔE was found. This statistical variation between the L loss locations can be quantified through:

$$\sigma_{\Delta E}^{stat} = \sqrt{\frac{1}{L-1}\sum_{i=1}^{L}(\Delta E_i - \overline{\Delta E})^2} \tag{5.9}$$

This calculation is done separately for the loss locations inside and outside MQ and lead to a relative standard deviation $\sigma_{\Delta E}^{losslocation}/\Delta E$ of 10.9% for loss locations outside MQ and of 9.3% for those inside the coil.

The accuracy of the radial energy dependence $\sigma_E(r)/E(r)$ can hence be estimated through adding the relative errors in quadrature [39]:

$$\left(\frac{\sigma_E(r)}{E(r)}\right)^2 = \left(\frac{\sigma_E^{fitting}}{E}\right)^2 + \left(\frac{\sigma_E^{losslocation}}{E}\right)^2 \tag{5.10}$$

loss location [mm]	$E_{D,cable}$ [mJ/cm^3]	No of critical protons/s
point losses:		
-8000	$1.15 \cdot 10^{-10}$	$4.01 \cdot 10^{11}$
-4800	$1.03 \cdot 10^{-9}$	$4.46 \cdot 10^{10}$
-4300	$2.67 \cdot 10^{-9}$	$1.73 \cdot 10^{10}$
-4050	$1.42 \cdot 10^{-9}$	$3.24 \cdot 10^{10}$
-3800	$2.42 \cdot 10^{-9}$	$1.90 \cdot 10^{10}$
-2879	$7.03 \cdot 10^{-9}$	$6.54 \cdot 10^{9}$
-2390	$1.12 \cdot 10^{-8}$	$4.10 \cdot 10^{9}$
-1475	$2.96 \cdot 10^{-8}$	$1.55 \cdot 10^{9}$
-1250	$2.71 \cdot 10^{-8}$	$1.70 \cdot 10^{9}$
-1000	$2.56 \cdot 10^{-8}$	$1.79 \cdot 10^{9}$
-750	$2.81 \cdot 10^{-8}$	$1.64 \cdot 10^{9}$
-500	$2.98 \cdot 10^{-8}$	$1.55 \cdot 10^{9}$
-250	$2.78 \cdot 10^{-8}$	$1.66 \cdot 10^{9}$
0	$2.82 \cdot 10^{-8}$	$1.63 \cdot 10^{9}$
loss patterns:		
Result Twiss	$9.08 \cdot 10^{-9}$	$5.07 \cdot 10^{9}$
Result SixTrack	$1.15 \cdot 10^{-8}$	$4.00 \cdot 10^{9}$

Table 5.6: Maximum in longitudinal and azimuthal direction of the energy density deposition in the cable per 450 GeV proton for each simulated loss locations.

assuming no correlation between the two errors. The obtained results for the relative error are of about 14.1% for outside the coil loss locations and 12.7% for the ones inside MQ. For further calculations the relative error due to the radial energy augmentation procedure for both groups of loss locations will be simplified to be of 14%.

The relative statistical error σ_E^{stat}/E due to limited Monte Carlo samples N can be calculated using:

$$\sigma_E^{stat} = \sqrt{\frac{1}{N-1}\sum_{i=1}^{N}(E_i - \overline{E})^2} \tag{5.11}$$

and was found to be of about 7%. Its variation between beam energies is negligible compared to its absolute value and the height of the other mentioned error sources.

Hence the final relative error $\Delta E_{max}^D/E_{max}^D$ of the maximum energy density deposition was calculated, taking into account the accuracy of the radial energy dependence and the error due to limited Monte Carlo samples:

$$\left(\frac{\Delta E_{max}^D}{E_{max}^D}\right)^2 = \left(\frac{\sigma_E(r)}{E(r)}\right)^2 + \left(\frac{\sigma_E^{stat}}{E}\right)^2 \tag{5.12}$$

assuming no correlation between the two errors. The found result is of about 16%.

loss location [mm]	$E_{D,cable}$ [mJ/cm^3]	No of critical protons/s
point losses:		
-3800	$3.18 \cdot 10^{-8}$	$9.43 \cdot 10^{8}$
-2879	$1.11 \cdot 10^{-7}$	$2.71 \cdot 10^{8}$
-2390	$1.35 \cdot 10^{-7}$	$2.22 \cdot 10^{8}$
-1475	$2.94 \cdot 10^{-7}$	$1.02 \cdot 10^{8}$
-1250	$3.02 \cdot 10^{-7}$	$9.94 \cdot 10^{7}$
-1000	$3.05 \cdot 10^{-7}$	$9.83 \cdot 10^{7}$
-750	$2.91 \cdot 10^{-7}$	$1.03 \cdot 10^{8}$
-500	$2.98 \cdot 10^{-7}$	$1.01 \cdot 10^{8}$
-250	$2.90 \cdot 10^{-7}$	$1.03 \cdot 10^{8}$
0	$3.08 \cdot 10^{-7}$	$9.73 \cdot 10^{7}$
loss patterns:		
Result Twiss	$1.10 \cdot 10^{-7}$	$2.73 \cdot 10^{8}$

Table 5.7: Maximum in longitudinal and azimuthal direction of the energy density deposition in the cable per 5 TeV proton for each simulated loss locations.

5.6 Signal in the BLM

Along the LHC main quadrupole magnet six BLMs have been installed, three for each beam. The signal collected at the beam line two, when losses occurred in the first line will be referred to as crosstalk.

The BLM location relative to the middle of the MQ coil is summarised in table 5.9 and depicted in figure 5.15. From the simulation not only the energy deposition in the coil is known, but also the characteristics of particles entering the BLM region are saved: kinetic energy, momentum, position and type.

In figures 5.16 and 5.17 one can see the angular distribution of the particles entering the BLMs after the simulated loss of a proton at the different predefined loss locations. The angle is the one between the z-component of the momentum and the total momentum of the particle. Of special interest is the situation for the locations outside of MQ, for example at -3800 mm corresponding to the yellow curve in the figures. In the asymmetry of the plot from these locations one can see the particles coming from the interconnection.

In figure 5.18 the angle distribution of the individual particle types from the loss location at the beginning of the beam screen is shown. The asymmetry is mainly due to the photons, that together with the neutrons build the major part of the detected particles.

In the spectra of the particles the dominating ones are neutrons and photons. In figure 5.19 is the energy distribution of the particles entering BLM1 and BLM2, where thermal neutrons have been taken into account. Those neutrons contribute to the signal in the ionisation chamber through processes of capture and de-excitation. Their total contribution is below 10%. Pions are the most energetic ones. This information is needed to conclude on the signal the BLM will produce. Knowing how the BLM will respond to a special particle with a certain energy and under a certain angle enables further conclusions. Those response functions are well known and an example is

loss location [mm]	$E_{D,cable}$ [mJ/cm^3]	No of critical protons/s
point losses:		
-2879	$1.49 \cdot 10^{-7}$	$1.54 \cdot 10^{8}$
-2390	$1.87 \cdot 10^{-7}$	$1.23 \cdot 10^{8}$
-1475	$4.28 \cdot 10^{-7}$	$5.38 \cdot 10^{7}$
-1250	$3.79 \cdot 10^{-7}$	$6.07 \cdot 10^{7}$
-1000	$4.32 \cdot 10^{-7}$	$5.33 \cdot 10^{7}$
-750	$4.31 \cdot 10^{-7}$	$5.33 \cdot 10^{7}$
-500	$3.97 \cdot 10^{-7}$	$5.79 \cdot 10^{7}$
-250	$4.11 \cdot 10^{-7}$	$5.60 \cdot 10^{7}$
0	$4.22 \cdot 10^{-7}$	$5.45 \cdot 10^{7}$
loss patterns:		
Result Twiss	$1.22 \cdot 10^{-7}$	$1.89 \cdot 10^{8}$

Table 5.8: Maximum in longitudinal and azimuthal direction of the energy density deposition in the cable per 7 TeV proton for each simulated loss locations.

BLM No	Observed beam	Location [mm]
BLM1	B1	-1143
BLM2	B1	1337
BLM3	B1	6007
BLM1	B2	1143
BLM2	B2	-1337
BLM3	B2	-6007

Table 5.9: BLM locations in the region of MQ relative to the middle of the coil [40]. The corresponding map with the main magnets is shown in figure 5.15.

shown in 4.3.

Folding the response functions with the information coming from the simulation then leads to the final BLM signal:

$$Q_{BLM} = \sum_{part=p,n,e^-,\gamma,...} \Bigg[\sum_{i=1...3} R_{i,part} N_{i,part} + w_\alpha R_{30,part} N_{\alpha,part} + (1 - w_\alpha) R_{0,part} N_{\alpha,part} \Bigg] \quad (5.13)$$

Where the main sum goes over the detected particles. Four response functions were used: 0° , 30° , 45° and 75°. The response functions $R_{i,j}$ are folded in different angle intervals with the particle fluence for the total detector surface $N_{i,part}$ and the final BLM signal is obtained.

Four different intervals were defined for the impacting angles:

1. i = 1: for impacting angles between 50° and 90° the 75° response function is used, as the variation between those angles is small.

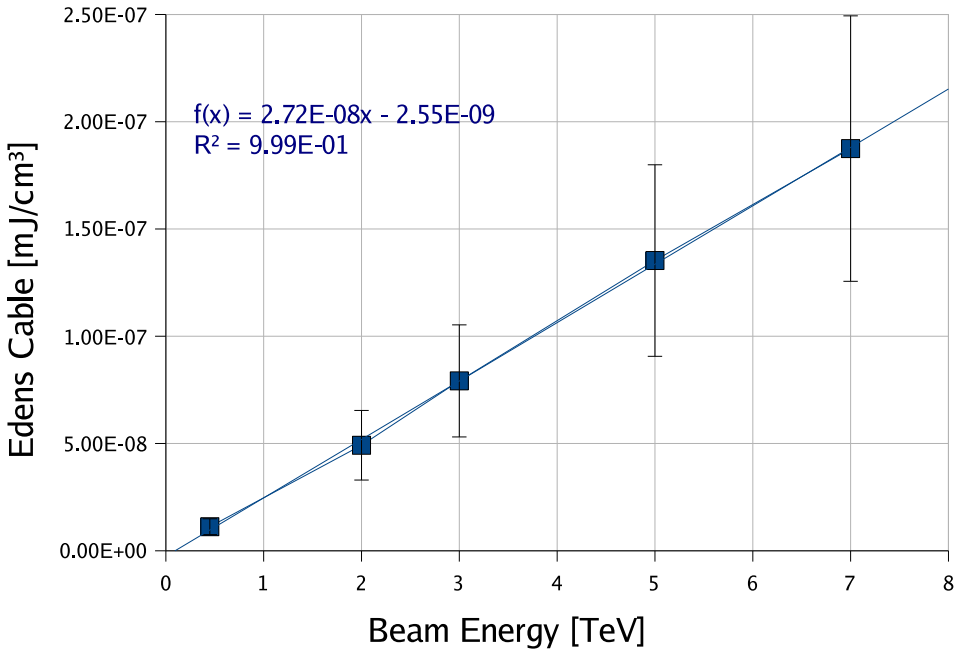

Figure 5.14: Energy density in the cable as a function of the beam energy.

2. i = 2: Particles with incoming angles between 30° and 50° are folded with the 45° response function.

3. i = 3: Particles with incoming angles between 30° and 35° are approximated with results for 30°.

4. As between an impacting angle α of 0° and 30° high variations occur, a linear interpolation was done, with the coefficient w_α being:

$$w_\alpha = \frac{\alpha}{30} \tag{5.14}$$

This is the last part in equation 5.13.

Particles entering through the endings of the monitors have been taken into account, under the simplified assumption that the particles do not interact with the electronic component at the end of the BLM.

The systematic error on the signal due to the choice of a response function not corresponding to the real particle angle is estimated to be around 10%.

The results at injection energy for each BLM and each loss location is shown in table 5.11 and plotted in figure 5.20. From the Geant4 simulations both BLMs at the position three do not show meaningful signals. For BLM3 at the first beam line, the signal is not only very low, but moreover the variations with respect to the loss locations are not statistically significant. Having in mind earlier analyses of critical loss locations the BLM3 can be considered as too far away to detect dangerous situations for MQ. The placement was chosen to be able to analyse the tail of the shower. For crosstalk studies the BLM at position 3 brought even lower, mostly negligible signals.

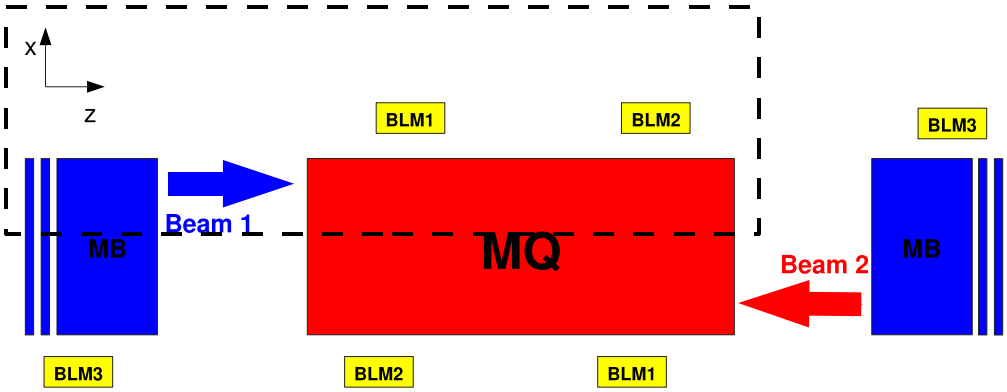

Figure 5.15: Map of the BLM positions for both beam lines. MQ designates the superconducting coil and not the entire cold mass with corrector magnets. The region inside the dashed line corresponds to the overview of the interconnection given in figure 5.2.

Only the loss location in MB at -8 m from the middle of the quadrupole coil reached a significant dose, which can been seen together with the other crosstalk BLM signals in table 5.11.

To again create a realistic loss scenario with the aim to set the final threshold, an averaging with respect to the loss locations is done for the signals inside the BLMs. The BLM signals are multiplied by their corresponding weights:

$$Q_{BLM} = \sum_{i=0}^{N} c_i Q_{BLM_i} \tag{5.15}$$

The final results have been introduced in the end of the table 5.10 for beam 1 and table 5.11 for beam 2.

In the table 5.12 one finds the BLM signals for beam line 1 at a beam energy of 5 TeV and in table 5.13 for collision energy.

The beam energy dependence of the BLM1 and BLM2 signals is shown in figures 5.21 and 5.22 respectively. A linear relation was found.

5.6.1 Error estimation

The statistical error due to limited Monte Carlo samples N is calculated using:

$$\sigma_{BLM} = \sqrt{\frac{1}{N-1}\sum_{i=1}^{N}(Q_{BLM,i} - \overline{Q_{BLM}})^2} \tag{5.16}$$

For 450 GeV this error was found to be of about 6%. For higher energies the error is smaller, which is due to the fact that with increasing proton energy a larger number of particles is detected in the ionisation chamber per loss event. The determined error for 450 GeV is the one kept for all beam energies, which will further mean to rather overestimate this error for higher proton energies.

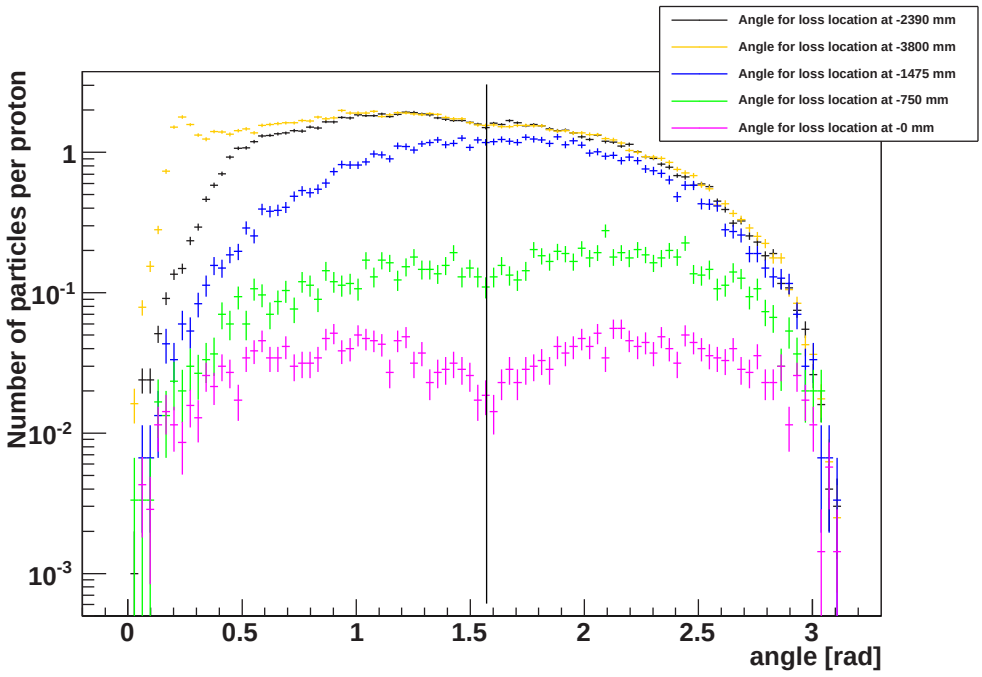

Figure 5.16: Impacting angle of particles entering the BLM1 from different loss locations. Points on the black line correspond to particles with a perpendicular impacting angle.

The Geant4 cascade tail simulation has an estimated accuracy of about 20% [27]. The reproduction of the response function together with the algorithm to retrieve the signal give an error of around 20% [41].

Therefore the relative error of the BLM signal $\Delta Q_{BLM}/Q_{BLM}$ is of about 29%, obtained using the formula for propagation of errors (see equation 5.12) without correlations between the three mentioned errors sources for the BLM signal.

5.7 Summary

The Geant4 geometry of the interconnection and its surroundings, used for the particle shower simulations, was presented.

The method is to simulate several loss events at 14 predefined loss locations. The energy deposition in the coil together with the signals in the ionisation chambers are recorded for each case. The detailed knowledge about the results for pointlike losses at every loss location was combined with the proton impact maps, in order to create a realistic loss scenario.

With the objective of protecting the sensitive element, one needs to investigate the maximum energy density deposition in the coil. To do this a radial augmentation between 25 and 80%, depending on the loss location and the beam energy, was taken into account. Furthermore a linear interpolation between the loss locations was applied, in order to augment the precision and smoothen the variations. Together with the coefficients of the loss patterns, the maximum energy density deposition from realistic loss

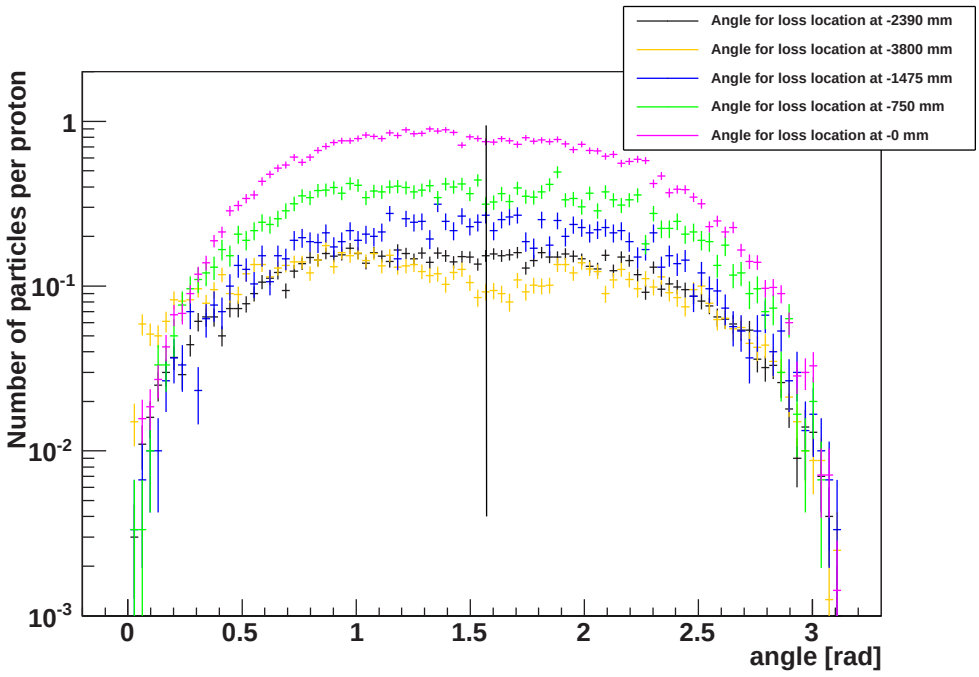

Figure 5.17: Impacting angle of particles entering the BLM2 from different loss locations. Points on the black line correspond to particles with a perpendicular impacting angle.

scenarios could be identified.

A special method was used to deduce from the Geant4 data the BLM signals. For each loss scenario the weighted average of the signal in the chambers was calculated.

The link between the maximum energy density deposition in the coil and the BLM signals is now known for each loss location, beam energy and the two proposed loss patterns. Together with the enthalpy margin for transient losses and the critical power density for steady state ones, it is hence possible to estimate the quench-protecting thresholds for each ionisation chamber.

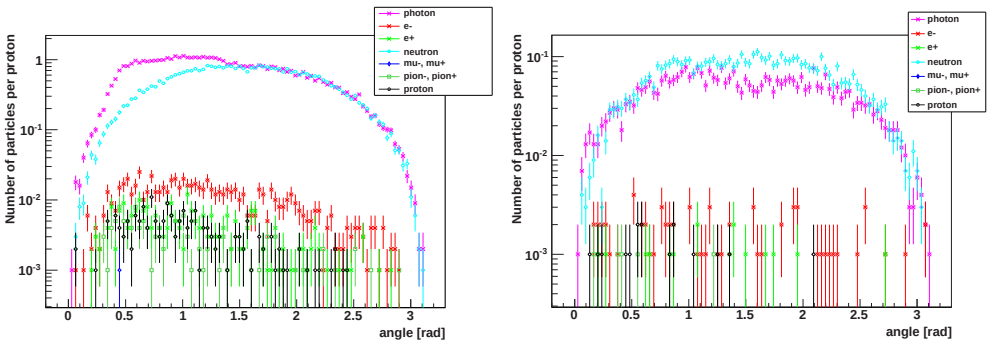

Figure 5.18: Impacting angle of the individual particle types entering the BLMs from the loss location at the beginning of the beam screen at z = -2390 mm. The left plot shows the situation for the first BLM, while the right one is for the second BLM.

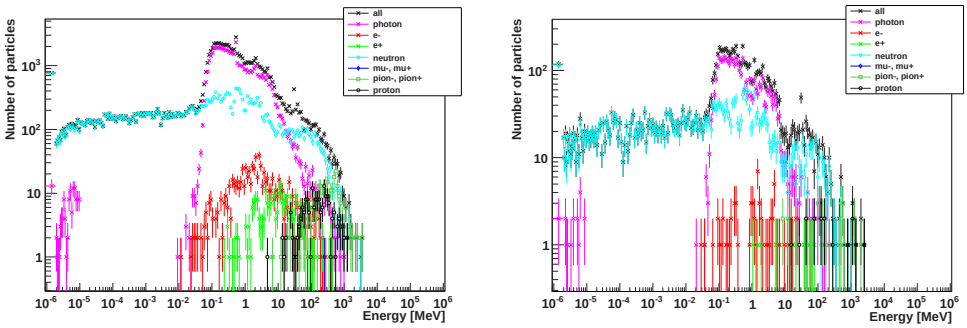

Figure 5.19: Energy distribution of the individual particle types entering the BLMs after the loss of a 450 GeV proton from the location z = -2390 mm. Left plot: for BLM1. Right plot: for BLM2.

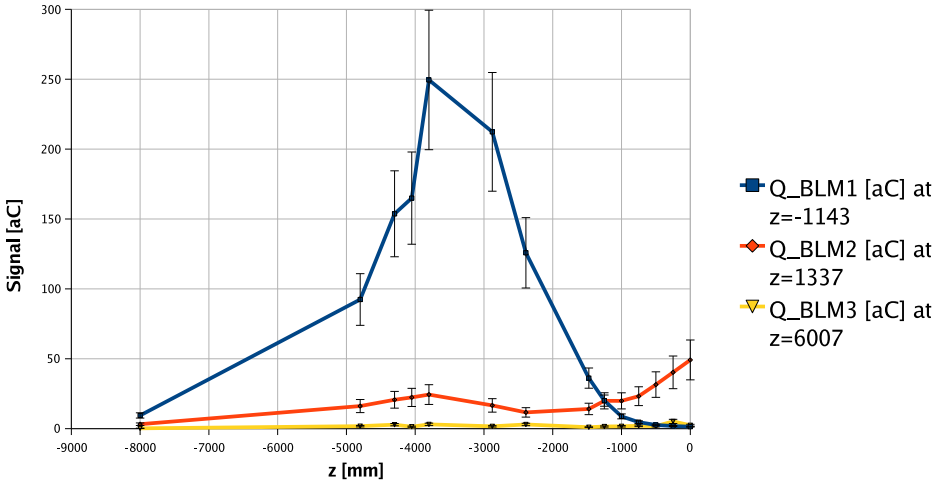

Figure 5.20: BLM signals at each loss location. Higher signals are coming from the interconnection, as particles are less shielded by the cold mass.

loss location [mm]	Q_{BLM1} [aC]	Q_{BLM2} [aC]	Q_{BLM3} [aC]
point losses:			
-8000	9.43	3.18	0.23
-4800	92.4	16.1	1.77
-4300	154	20.7	2.83
-4050	165	22.4	1.40
-3800	249	24.4	3.06
-2879	212	16.6	1.66
-2390	126	11.6	2.98
-1475	36.2	14.1	1.01
-1250	20.1	19.9	1.54
-1000	8.77	19.9	1.70
-750	4.63	23.2	2.02
-500	2.63	31.5	1.77
-250	1.87	40.3	5.18
0	1.40	49.2	2.41
loss patterns:			
Result Twiss	111	14.4	2.77
Result SixTrack	53.3	24.7	2.36

Table 5.10: Beam 1 BLM signals per 450 GeV proton for the simulated loss locations

loss location [mm]	Q_{BLM1} B2 [aC]	Q_{BLM2} B2 [aC]	Q_{BLM3} B2 [aC]
point losses:			
-8000	0.6	2.13	10.04
-4800	1.76	32.7	0.97
-4300	5.16	56.1	1.36
-4050	3.43	49.2	0.4
-3800	3.02	54.4	0.45
-2879	1.75	35.3	0.19
-2390	1.67	23.8	0
-1475	2.75	4.9	0
-1250	4.28	2.86	0
-1000	4.27	1.64	0
-750	5.29	1.45	0
-500	6.03	0.95	0
-250	7.45	0.78	0
0	7.42	0.54	0
loss patterns:			
Result Twiss	2.27	22.4	0.27
Result SixTrack	4.48	13.1	0.21

Table 5.11: Crosstalk: Beam 2 BLM signals per 450 GeV proton for the simulated loss locations. Q_{BLM3} barely detects particles, only the location at -8000 mm brings a noticeable signal.

loss location [mm]	Q_{BLM1} [aC]	Q_{BLM2} [aC]	Q_{BLM3} [aC]
point losses:			
-3800	2183	175	25.6
-2879	1777	154	14.6
-2390	942	90.5	17.0
-1475	198	116	18.7
-1250	111	133	17.0
-1000	51.7	165	16.2
-750	26.9	182	19.7
-500	17.9	256	21.8
-250	11.3	287	25.1
0	9.08	347	22.3
loss pattern:			
Result Twiss	841	110	17.7

Table 5.12: Beam 1 BLM signals per 5 TeV proton for the simulated loss locations. SixTrack simulation were done for higher energies than 450 GeV, but their loss statistic is too low to be able to deduce a loss pattern.

loss location [mm]	Q_{BLM1} [aC]	Q_{BLM2} [aC]	Q_{BLM3} [aC]
point losses:			
-2879	2123	260	19.4
-2390	1283	117	23.6
-1475	241	139	30.8
-1250	153	167	12.5
-1000	73.3	224	43.4
-750	33.0	223	23.0
-500	19.8	340	32.9
-250	13.4	371	20.4
0	10.9	491	41.5
loss pattern:			
Result Twiss	1082	138	23.9

Table 5.13: Beam 1 BLM signals per 7 TeV proton for the simulated loss locations. SixTrack simulation were done for higher energies than 450 GeV, but their loss statistic is too low to be able to deduce a loss pattern.

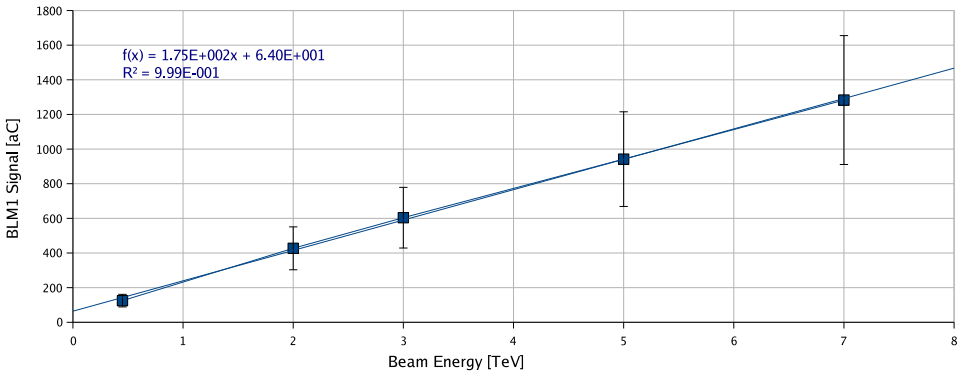

Figure 5.21: BLM1 signals as a function of the beam energy.

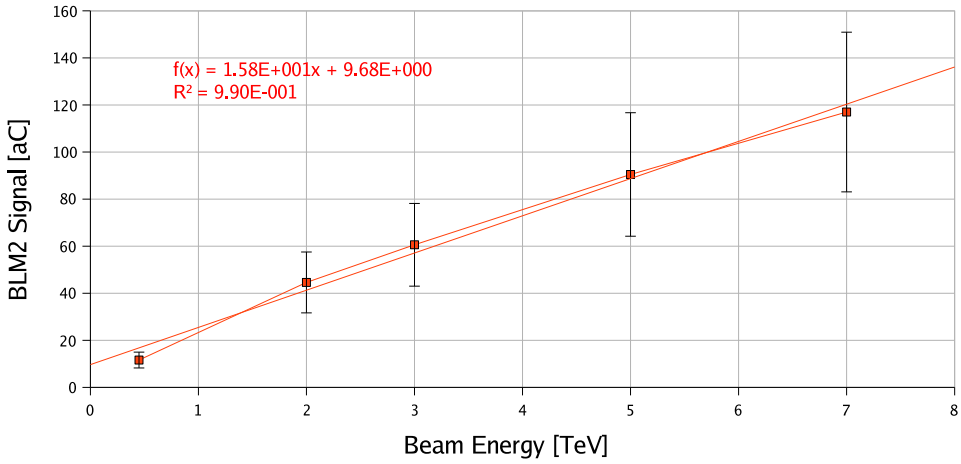

Figure 5.22: BLM2 signals as a function of the beam energy.

Chapter 6

Quench-protecting Threshold

In the previous chapter the link was made between Geant4 simulation of the signals in the chambers and the energy deposition in the superconducting magnet coil. The threshold now defines the limit between safe losses and losses at which equipment is considered to be in danger. In this study the considered equipment is the main quadrupole magnet and the danger is the transition from a superconducting to a normal conducting state. If the threshold is exceeded, the beam will be dumped to ensure machine protection. In the case of the BLMs on the main quadrupole magnet, one is interested in the protection of the superconducting coil from quenches.

An important point that needs to be taken into account for the threshold setting is the operational efficiency: the threshold needs to be set in a way that the magnet is protected from quenches, but at the same time unnecessary down-times of the LHC should be avoided. This down-time is among other things due to the fact, that the dump system needs to be rearmed, the magnet currents have to be trimmed down and their pre-cycling has to be done. If the BLM request a beam dump for the slightest losses, a optimal operation would be impossible. The energy could not be ramped up to interesting domains and no luminosity would be possible so that for physics no new results could be found. A too high threshold setting on the other hand could have the consequences of quenching or even damaging the superconducting coils before a reaction of the BLM system. Therefore an initial accuracy of a factor of in the threshold setting is requested.

In order to achieve this accuracy different parameters need to be investigated:

1. how much energy can be deposited in the magnet without the induction of a quench?

2. how much energy is deposited in the superconducting magnets?

3. how high is the corresponding signal in the BLMs?

Those parameters were analysed in earlier sections (3.2.1, 3.3, 5.5 and 5.6). The combination between them is done in this chapter: their information is combined in order to calculate the quench protecting thresholds for BLMs on the superconducting MQ magnet.

All three points are depending on the energy of the circulating beam. Additionally the first parameter also depends on the time-scale at which the beam is considered to

be lost and the last two parameters vary with the loss location and hence with the loss pattern.

The effect of different time scales of beam losses will further be analysed through two extrem cases:

- transient losses and
- steady state losses.

Transient losses are faster than any time depending mechanism in the considered situation, while for steady state losses a heat flow needs to be taken into account.

6.1 Transient Losses

6.1.1 Threshold calculation

The threshold defines the limit between BLM signals from innocuous losses and the ones for which machine consequences have do be feared. In this study the goal is to determine the threshold for the Short Straight Section BLMs such that the superconducting quadrupole magnet will be protected from quenches in case of transient losses. As the time scale for this type of loss is very small compared to the duration of heat exchange with the cooling system, no time depending mechanism needs to be taken into account and the parameter of interest is hence the total radiation dose in Gy.

The following equation defines the threshold $T_{transient}$ for transient processes:

$$T_{transient} = \frac{H_{limit}}{E^D_{max}} Q_{BLM} = N_{critical} Q_{BLM} \tag{6.1}$$

with:

E^D_{max}: Maximum energy density deposition in the coil of the average lost proton in mJ/cm^3. This term was discussed in section 5.5, where its results are presented for each loss location, loss scenario and various beam energies.

H_{limit}: Enthalpy limit of the coil in mJ/cm^3. This term was discussed in section 3.2.1, where its results are depicted for various beam energies.

Q_{BLM}: Signal in the detector in Gy. The signals are initially expressed in aC. To convert them into units used for the expression of the threshold the following conversion factor is used: $5.4 \cdot 10^{-5}$ C/Gy[1]. The detector signals were investigated in section 5.6 and there results are summarised for each loss location, loss scenario and various beam energies.

$N_{critical}$: Number of critical protons. For the calculation of the operational thresholds, the number of critical protons is not a fundamental parameter. Nevertheless the knowledge of those critical numbers is essential for practical reasons and can be found in section 5.5 for each loss location, loss scenario and various beam energies.

The threshold calculations can hence be done for the realistic loss scenarios and for each loss location in order to compare and analyse the obtained results.

[1]This conversion factor is calculated using the W-factor and the mass of the detector gas in the ionisation chamber.

6.1.2 Thresholds for each loss location

To obtain the thresholds for each loss location, equation 6.4 is applied for every loss location using the results of the maximum energy density deposition and the signals summarised in the tables 5.3 and 5.10 respectively. Furthermore the enthalpy limit presented in table 3.2 is utilised for the beam energy for which the threshold is estimated.

The resulting thresholds for injection energy are shown in table 6.1 and figure 6.1, demonstrating the high variation of the BLM thresholds with the loss location for punctual losses. This counts specially for the BLM at position 1. It is due to the fact, that from outside of the MQ a low energy deposition in the coil together with a high BLM signal is obtained, while it is the opposite for losses inside the MQ, as the particles almost directly hit the coil, but are shielded through the cold mass until they reach the BLM. Hence thresholds corresponding to losses from outside the superconducting coil are higher than the ones from losses inside MQ, which is true for all three ionisation chambers. This further means that the criticality of a lost beam depends on its impact location. Simply taking the lowest found threshold as the final one, would be the safest. At the same time it would make beam operation impossible, as already slight innocuous losses coming from the interconnection would trigger a beam dump. As mentioned earlier such unnecessary downtimes are unacceptable. To set a correct threshold it is therefore critical to find the realistic loss patterns (see section 3.3).

	Threshold [μGy]		
Loss location [mm]	BLM1	BLM2	BLM3
-8000	4543	1530	112
-4800	8260	1443	158
-4300	12894	1733	237
-4050	20856	2826	177
-3800	21083	2059	259
-2879	7230	566	56.4
-2390	2871	265	68.0
-1475	210	82.0	5.85
-1250	132	131	10.2
-1000	60.2	137	11.7
-750	25.5	128	11.1
-500	14.5	174	9.73
-250	10.9	235	30.2
0	8.61	302	14.8

Table 6.1: Transient thresholds at each loss location for 450 GeV beam

A method to augment the accuracy of the BLM system could be to develop a conditional threshold setting. An example would be: conditional threshold for BLM2 at 140 μGy if the signal in BLM1 is smaller than 210 μGy. High signals at position 2 in comparison to position 1 would mean, that the losses happened inside MQ and a higher energy deposition occurred, so that the threshold should be low. On the other hand if the BLM1 and BLM2 signals are both high, the losses would come from the

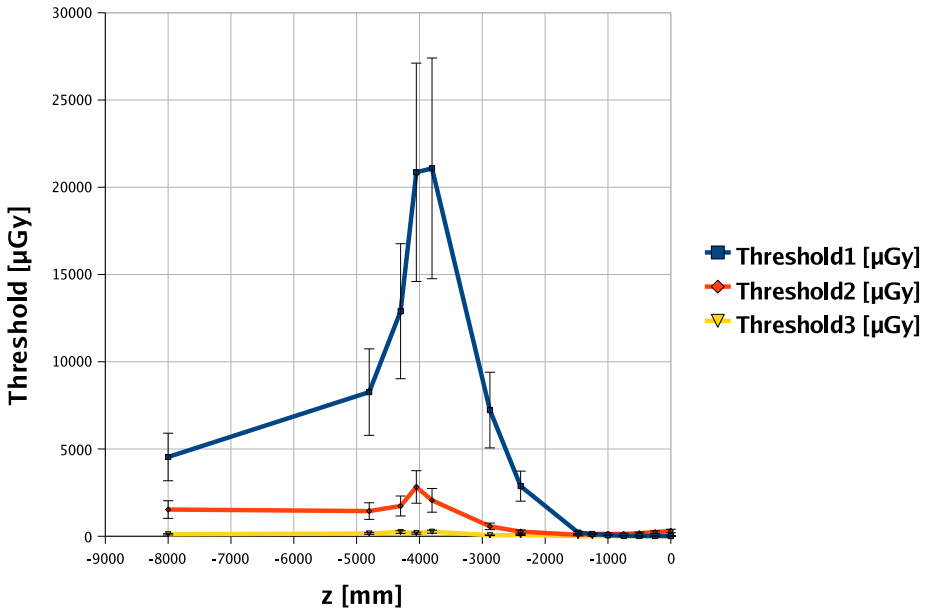

Figure 6.1: Calculated thresholds for each loss location.

interconnection and a higher threshold could be taken. This conditional threshold could be done through electronic logic and would increase the precision of the system for a beam dump. But it would also prolongate the reaction time. Yet the BLM system needs to be very fast and reliable, this is why such conditional thresholds can not be used.

6.1.3 Protection strategy for the BLMs

For the final threshold further considerations are done. Not only for all three BLMs the results from two loss patterns have to be compared:

- Twiss parameter calculations and
- SixTrack simulations

but also other specifications can be chosen: one needs to decide on the region and the sensitive element each BLM should protect. Initially the BLMs have been installed in this region to protect MQ, but the analysis showed, that also MB can and should be considered for protection. Those protection strategies for each BLM has the advantage of a higher accuracy, but also signifies a lowered redundancy of the system, in case of failures.

Those considerations will further be explained for each BLM, as their situation is different.

BLM1:

Due to its position after the interconnection, the BLM1 threshold can be set according to different options. Protons lost in MB still leave a high signal in BLM1, therefore the following sensitive elements can be protected:

- MQ or
- Bus bars in the interconnection or
- MB.

One needs to find which one of the superconducting elements is more sensitive to losses.

It was quickly shown through the Geant4 simulations, that the energy deposition from losses in direction of the bus bars inside those is much lower than the one in the main quadrupole. This is mainly due to the fact that the superconducting bus bars are about 50 times farther away from the beam trajectory than the quadrupole magnet[2]. Hence a protection of MQ is also guaranteeing a protection of the bus bars.

Furthermore loss locations situated behind the BLM1 position could be considered as not seen by the chamber, as only few particles reach the BLM from those loss events. Hence following regions can be though of for the threshold setting of BLM1:

- the whole region from -8000 to 0 mm is taken into account,
- only losses before the BLM1 position from -8000 to -1250 mm (see figure 5.2) are taken into account and
- only losses before MQ from -8000 to -2390 mm are taken into account. This would mean a regional specialisation of BLM1 for the interconnection, while BLM2 would still protect from losses occurring inside the coil region.

The calculated thresholds for each case can be found in table 6.2. The calculation was done using equation 6.4. The used values for the enthalpy margin do only depend on the beam energy and the protected magnet. The BLM signal depends on the regional specialisation of the detector, the beam energy and the considered loss pattern. The maximum energy density deposition depends on all the mentioned factors, being: the regional specialisation of the detector, the beam energy, the protected magnet and the considered loss pattern.

The values used for the protection of MQ without a regional specialisation of BLM1 are presented in section 5.6 and 5.5. For example the first threshold in table 6.2 was obtained with a maximum energy density deposition of $2.40 \cdot 10^{-8}$ mJ/cm^3 per 450 GeV proton (from table 5.3), a BLM signal of 111 aC/proton (from table 5.10) and an enthalpy margin equal to 36.52 mJ/cm^3 (from table 3.2).

In order to calculate the thresholds for the protection of MB, one needs to know that the maximal energy density deposition in MB. From a 450 GeV proton it was found to be around $1.4 \cdot 10^{-7}$ mJ/cm^3 on the inner surface of the coil at 35 cm after the loss location [41]. This value was used and adapted for the loss locations situated inside MB.

For the threshold calculation with regional specialisation of the BLM coefficients for the two loss patterns from table 3.3 need to be adapted to the considered region.

[2]The MQ radius is of 2.8 cm, while the distance between the bus bars and the centre of the beam screen is about 14.5 cm.

For each loss location i inside the protected region A, the new coefficients w_i^A can be obtained from the coefficients w_i^Ω of the whole region Ω:

$$w_i^A = \frac{w_i^\Omega}{\sum_{n \in A} w_n^\Omega} \tag{6.2}$$

Those coefficients w_i^A are used to redo the steps described in section 5.5 and 5.6 and hence recalculate the maximum energy density deposition and the BLM signal corresponding to the regional specialisation of the detector for each loss scenario, beam energy and protection strategy.

Protected region	Loss pattern	Threshold BLM1 [μGy]	
		MQ Protection	MB Protection
Whole Region	Twiss	3134	6527
	SixTrack	1210	1682
Region before BLM1	Twiss	3264	7187
	SixTrack	1521	3075
Region before MQ	Twiss	3228	7431
	SixTrack	5311	4902

Table 6.2: BLM1 threshold at 450 GeV for the two considered loss patterns and various protection strategies.

Results from SixTrack lead generally to lower thresholds than the ones from Twiss calculations, which can be explained through the different weighting of the loss locations in table 3.3. The observed variation of the thresholds with the loss location shown in table 6.1 imply a high dependency of the final threshold on the weight each loss location is given. This is specially the case for BLM1, where the highest threshold is of 21 mGy at z = -3800 mm, while the lowest is about 9 μGy at z = 0 mm. This corresponds to a factor of about 2300. For the SixTrack loss pattern, losses in the middle of MQ are given a higher importance than for the Twiss proton impacts. Lower thresholds for losses inside MQ together with a higher weighting of those, lead to a lower threshold for the SixTrack loss pattern than for the Twiss one[3]. The exception is the regional specialisation of BLM1 to the area before MQ, where losses inside the coil are not taken into account.

The results for the Twiss loss patterns are very similar for the different considered regions. The reason for this is the domination of the loss location z = -2390 mm at the beginning of the beam screen, which is taken into account for every proposed regional specialisation.

The thresholds for the protection of MB are in general higher than the ones for MQ. This does not mean that in general the protection of the main dipole is assured, when the quadrupole is protected. But it means that under considered circumstances the BLM1 is better placed for the protection of MQ than of MB.

[3]Please note: the explanation through the variation of the thresholds with the loss locations is an intuitive one. The mathematical procedure to obtain the final thresholds is not based on those, but on the BLM signals and the maximum energy density deposition in the coil for each case. This is due to the fact, that one is not interested in a weighted average energy density deposition, but needs to investigate its maximum (as shown in figures 5.11 and 5.12) for each of the discussed cases.

Furthermore one can dismiss the intention to protect the whole region: BLM1 is not able to protect from losses happening in the middle of MQ. As the monitor would be situated upstream of those losses, they would lead to a very low signal in the chamber. The option to assign BLM1 on the interconnection would signify to renounce the possibility of protecting the main quadrupole from losses happening at its beginning, although BLM1 would be well placed for such an event. Furthermore the system would lose in its redundancy, which was defined as a high priority.

For the quench protection of the quadrupole coil by BLM1 the best region to take into account is therefore the one before the position of the monitor.

Important to notice is that the first running sum RS01 is electronically saturated at a dose of 948 μGy. The major part of the presented thresholds exceed this value. Solutions could be:

- the installation of a capacitor reshaping the signal and adopting it to more 40 μs bins or
- the installation of smaller chambers, creating less charges and therefore saturating at a higher level.

BLM2:

The position of BLM2 is situated perfectly to detect losses happening inside MQ. Hence the option of a protection of MB by BLM2 is not reasonable. Furthermore the signal in BLM2 from losses inside MB are not significant compared to the ones measured by BLM1. Therefore a regional specialisation of BLM2 on the MQ region only could be an alternative worth achieving. Hence concerning the region two cases are interesting:

- the whole region needs to be taken into account and
- only the region inside MQ delivers the most suitable threshold.

The calculated thresholds for each case can be found in table 6.3. The calculation was done through the equation 6.4 and the intermediate values for a regional specialisation of BLM2 are obtained the same way as described for BLM1.

The difference between the two loss patterns is less significant than it was for BLM1, which can be explained through the fact that the highest local threshold for BLM2 in table 6.1 is of 2830 μGy at z = -4050 mm, while the lowest is of 26.5 μGy at z = -2390 mm. This corresponds to a factor of 107, which is much lower than for the first detector. Additionally both extreme thresholds come from loss locations outside the coil, so that their effect is less visible when performing the regional specialisation compared to BLM1.

BLM2 thresholds obtained from SixTrack loss patterns are similar, while the ones from Twiss calculations have almost a factor of 2 between each other. The reason is that the high weighted loss location at the beginning of the beam screen is taken into account for the whole region, while it is excluded in the second protection strategy.

The thresholds for a regional specialisation of BLM2 on the superconducting coil are higher than the ones where the whole region is taken into account. This can be understood through the signals in the chambers, that are in general higher for losses inside the coil, than the ones from losses before the magnet. The difference is larger for

Protected region	Loss pattern	Threshold BLM2 [μGy] MQ Protection
Whole Region	Twiss	405
	SixTrack	560
Region inside MQ	Twiss	772
	SixTrack	575

Table 6.3: BLM2 threshold at 450 GeV for the two considered loss patterns and two protection strategies.

the Twiss loss scenario. This is again due to the high importance of the loss location at the beginning of the beam screen, which is excluded in the case of only taking the region inside MQ into account.

From its location, BLM2 is perfectly suitable for the purpose to only protect from losses inside the coil. Although this means choosing the higher thresholds, it is possible, as BLM1 still protects from losses coming from locations upstream to the superconducting quadrupole magnet. This proposed separation of the monitors observation range leads to a gain of accuracy but at the expense of a loss in redundancy.

BLM3:

The purpose of the third monitor is the detection of secondaries coming from the interconnection downstream of the main quadrupole [23]. Like in the interconnection upstream of MQ, studied in detail in this study, an aperture limitation is present.

Unfortunately the values found for BLM3 are not conclusive. Each of the investigated loss locations brought low signals in this ionisation chamber. The closest to the BLM3 position is the loss location in the middle of MQ at z = 0 mm. Even at this position the signal in the monitor was found to be low in the simulation. This together with the fact that the simulations from SixTrack do not expect losses after the middle of MQ (both results also found in [23]) leads to a possible reevaluation of the monitors position. Further discussion about BLM3 will be done in section 7.1.

The general case for MQ protection and considering the whole region brought the results for the thresholds of BLM3 shown in table 6.4.

Loss pattern	Threshold BLM3 [μGy]
Twiss	78
SixTrack	54

Table 6.4: BLM3 thresholds for injection energy.

6.1.4 Proposition for final transient thresholds

The decision about which threshold should be set for each BLM needs to be done. Two different loss patterns were described and their implication on the quench protection was calculated. Moreover a regional specialisation of the BLMs was proposed and is considered for some cases to be worth achieving.

As a reminder: the main difference between the two loss patterns was that for one the assumption of a Gaussian beam was done, while for the SixTrack simulations the

losses came from off-momentum and off-orbit particles from the halo of the beam at injection energy. Second one can be considered as a realistic loss scenario at injection and the thresholds for 450 GeV should therefore be set according to its results. With higher beam energy the loss pattern changes and is supposed to become more similar to the one obtained through Twiss calculations. Therefore the quench-protecting thresholds for 5 and 7 TeV are estimated according to the Twiss loss pattern. This assumption needs further checking with more LHC operation experience.

For all the detectors a protection of the main quadrupole was found to be the optimal strategy. Additionally a regional specialisation for BLM1 and BLM2 was discussed. The conclusion was that the first detector can ideally protect from losses coming from the end of the upstream MB, the interconnection and the beginning of MQ, while BLM2 protects optimally from losses happening inside the quadrupole coil.

The thresholds for 450 GeV are in the tables 6.2, 6.3 and 6.4. The optimal threshold values at injection energy are in table 6.5 and correspond to the SixTrack loss scenario, with protection of MQ and the chosen specialisation of the BLMs. For higher beam energies the calculations and methods mentioned in sections 6.1.1 and 6.1.3 are done again. The discussed protection strategies are the same for each BLM as for injection energy. Only the loss pattern is expected to change with higher energies, becoming more similar to the Twiss loss scenario, as a Gaussian beam halo is then conjectured. This is therefore the one chosen for 5 and 7 TeV beam energy.

The final thresholds are summarised in table 6.5.

	Threshold [μGy]		
Beam Energy [TeV]	BLM1 [μGy]	BLM2 [μGy]	BLM3 [μGy]
0.45	1521	575	54
5	588	118	11.4
7	178	29.4	3.05

Table 6.5: Final quench protecting thresholds for MQ for transient losses. BLM1 was assigned to the region before its position and BLM2 on the MQ area, whereas the third monitor takes the whole region into account. One should keep in mind that for injection energy the values from the SixTrack loss pattern were found to be more adequate, whereas for 5 and 7 TeV the Twiss values were the chosen ones, which is together with the enthalpy margin (see figure 3.4) the main reason why the thresholds are not linear with the beam energy.

To verify those results and find out which options are best suited, a loss distribution with a quench of the MQ in the first running periods would have been ideal. The perfect quench for the calibration of the BLM system is when the QPS detects a voltage above its threshold and while the magnet could recover by itself, the QPS is heating up the coil. A controlled quench is induced. This situation would be specially interesting, as it defines the limit between safe BLM signals and the ones, where magnet quenches could happen. Those could be observed four times for MB already and never for MQ. Nevertheless important information can be gained for the situation in the interconnection.

The variation of the BLM1 threshold (without regional specialisation of the monitor and for a loss coming from the beginning of the beam screen at z = - 2390 mm)

with the beam energy is shown in figure 6.2.

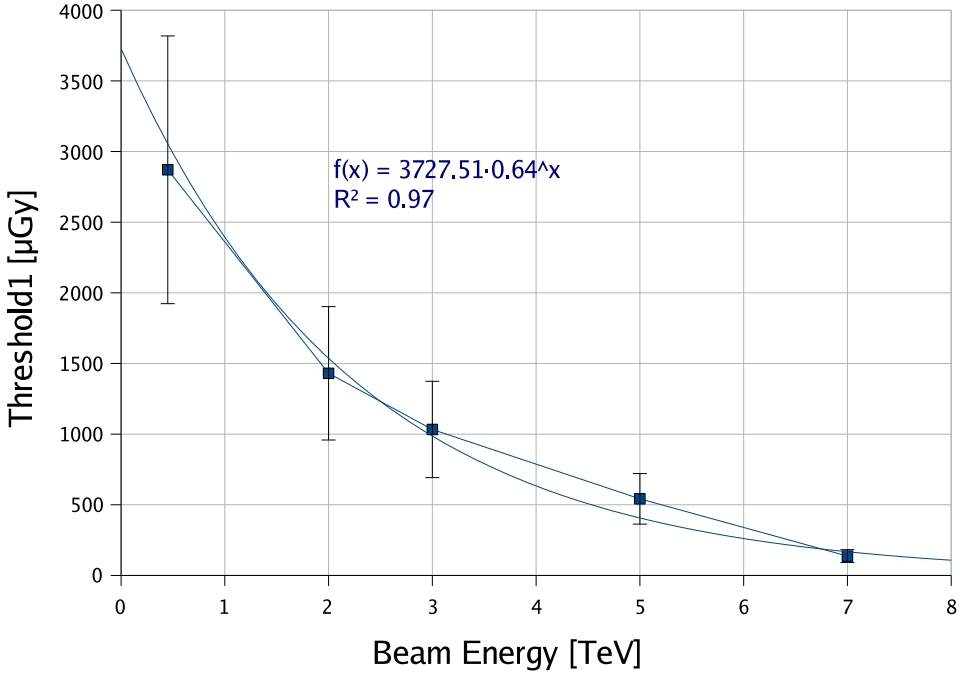

Figure 6.2: Threshold of BLM1 as a function of the beam energy for the loss location at the beginning of the beam screen. The plotted values are the initial ones, unprocessed through loss patterns and regional specialisation of the monitors.

6.1.5 Comparison with MB threshold

The thresholds of BLM2 of the main quadrupole can be compared to the ones of MB BLMs, as they have a similar position relative to coil and beam. Further significant conclusions through the comparison can also be drawn for BLM1.

The thresholds for the main dipole magnet were investigated in [41]. The main dipole is 14.3 m long and 1232 of them are used in the LHC. Therefore around 66 % of the LHCs cicumference is made of those dipoles, with a magnetic field of up to about 8.56 T. This is needed to keep the high energy particles on the circular trajectory. The MB is expected to be less exposed to beam losses than MQ, as betatron and dispersion functions are smaller. Therefore only a few main dipoles in special situations are protected with BLMs. Those exceptions are due to a positioning downstream of collimators and for losses specific to ion beams.

Pointlike losses along MB have been simulated and distributed losses were obtained by convoluting with a broad gauss distribution, knowing that the loss distribution of a Gaussian beam along the beam screen is Gaussian too, because the physical aperture stays constant. This is one of the main differences to the assumption of the situation in MQ, where distributed losses were obtained through the construction of loss patterns. The standard deviation of the proton loss distribution was chosen to be σ_{loss} = 4 m at injection energy. This has been observed during the first MB quench and

corresponds to a beam with σ_{beam} = 1 mm lost with an impacting angle of 250 μrad, as it would be expected for 450 GeV proton beam. The obtained results are shown in table 6.6

The energy dependence of the BLM2 threshold (without regional specialisation of the monitor and for a loss coming from the beginning of the beam screen at z = - 2390 mm) can be seen together with the MB thresholds in figure 6.3. This comparison is informative, as their placement relative to beam and coil is similar.

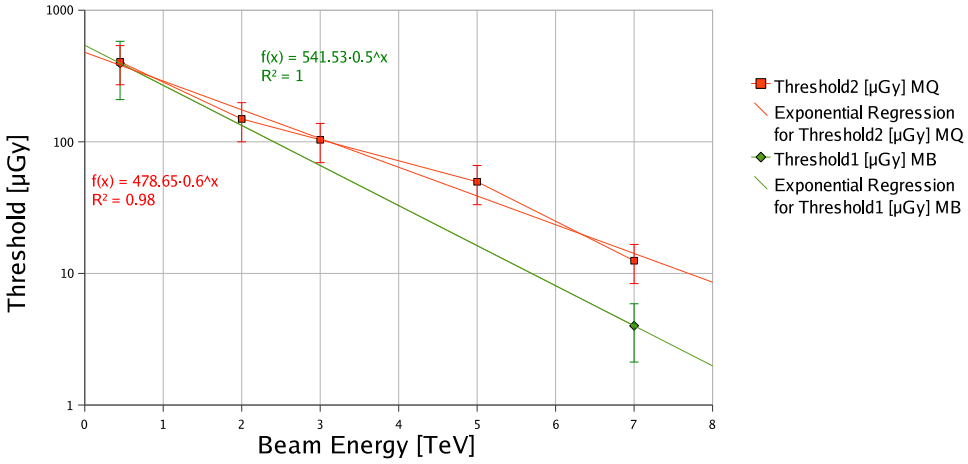

Figure 6.3: Thresholds of MB according to [41] and threshold of BLM2 as a function of the beam energy for the loss location at the beginning of the beam screen. The plotted values are the initial ones, unprocessed through loss patterns and regional specialisation of the monitors.

In the case of the monitors on the main quadrupole magnets the interconnection plays an important role. Losses happening there lead to high BLM signals due to less shielding material in this zone and a lower energy deposition compared to losses inside the region of the coil. This argument suggests a higher threshold for MQ than for MB, which is especially the case for BLM1, situated even closer to the interconnection.

Furthermore the results from ROXIE show a higher enthalpy margin for MQ than for MB, the difference being small at 450 GeV but increasing with higher energies until reaching a factor of about three at collision energy. This effect is perfectly identifiable in figure 6.3, where the values are similar at the beginning and spread out for higher beam energies.

With a σ_{loss} = 4 m, 95 % of the losses are expected to happen over a length of 16 m in the case of MB. For MQ the assumption in the loss patterns is that 100 % of the losses happen in a region of 8 m, with a major part of them concentrated in the interconnection and the beginning of MQ. The losses are hence expected to happen more locally for MQ than for MB.

In the case of MB one found that higher spread leads to higher thresholds, while a more narrow spread leads to lower thresholds. This is mainly due to the fact that the energy deposition in the coil was found to decrease faster than the signal inside the chambers with higher spread of the losses. For BLM1 and BLM2 of MQ actually

the contrary is the case, which can be seen through the regional specialisation of the monitors, corresponding to scaling down the considered region. For BLM1 this is simply due to the fact that through the regional specialisation of BLM1 losses behind the monitor leading to very low thresholds are excluded. The situation for BLM2 is similar: narrowing down the region to points where the chamber signals are significant again leads to higher thresholds.

For the main quadrupole one has the opportunity to assign the ionisation chambers to regions considered as critical from the loss patterns and for which the monitors detect a considerable amount of particles. The thresholds can hence be set to a higher level and a better accuracy is reached.

In table 6.6 the thresholds for MB and BLM2 of MQ are summarised for injection and collision energy. For 7 TeV the major effect of the higher enthalpy margin of the main quadrupole is visible.

	MB Thresholds [μGy]	MQ BLM2 Thresholds [μGy]
Injection Energy	395 ± 194	575 ± 189
7 TeV Collision Energy	4.0 ± 2.3	29.4 ± 9.7

Table 6.6: MB and MQ BLM2 final thresholds for distributed and transient losses.

6.2 Steady state losses

6.2.1 Threshold Calculation

For transient losses a central parameter was the energy deposition inside the superconducting coil, the criteria for steady state losses is the power density. Futhermore a heat transition to the Helium cooling system needs to be taken into account.

The following equation defines the threshold $T_{steadystate}$ for steady state losses:

$$T_{steadystate} = \frac{w_q}{E_{D,cable}} Q_{BLM} = \dot{n_q} Q_{BLM} \tag{6.3}$$

where $\dot{n_q}$ is the quench limit in protons per second, w_q is the quench margin defined by the heat transmission capability, $E_{D,cable}$ is the energy density deposition in the cable and Q_{BLM} is the signal inside the chamber. The dimension of the thresholds for steady processes is given in μGy/s, as time depending mechanisms need to be taken into account.

The quench margin was discussed in section 3.2.2 and its results presented for different beam energies. The values of the energy density deposition in the cables for each loss location, each loss pattern and various beam energies can be found in section 5.5.4.

6.2.2 Thresholds for each loss location

To obtain the thresholds for each loss location, equation 6.3 is applied for every loss location using the results of the maximum energy density deposition in the cable and the signals summarised in the tables 5.6 and 5.10 respectively.

The resulting thresholds for injection energy are shown in table 6.7, depicting the high variation of the BLM thresholds with the loss location for punctual steady state losses. As for the transient case this counts specially for the BLM at position 1. The reasons are the same as discussed in the section for transient losses.

	Threshold [μGy]		
Loss location [mm]	BLM1	BLM2	BLM3
-8000	70100	23600	1730
-4800	76400	13300	1460
-4300	49100	6700	904
-4050	99000	13400	837
-3800	87600	8560	1080
-2879	25700	2010	201
-2390	9550	882	226
-1475	1040	406	28.9
-1250	630	625	48.5
-1000	291	660	56.4
-750	141	704	61.3
-500	75.2	902	50.5
-250	57.3	1240	159
0	42.4	1490	72.8

Table 6.7: Steady state thresholds at each loss location for 450 GeV beam.

6.2.3 Protection strategy for the BLMs

For steady state losses the same protection strategies as for transient ones are presented. One will see through the results that also the major conclusions stay the same. Due to the possibility of heat exchange the thresholds are in general much larger than for the case of transient losses.

BLM1

As the protection of MB through the first monitor was found to be less reasonable than the one for MQ, its results are skipped in table 6.8.

One again observes that the thresholds from Twiss loss scenarios are very similar, while the ones in the case of losses according to SixTrack undergo higher variation. The explanations for those observations are the same as the ones for the transient case and can again optimally be illustrated with table 6.7 and the observation of its high variations. Specially the last strategy for taking into account only losses before the coil has a large threshold, which can be explained through the falling away of high weighted losses inside the magnet.

BLM2

The results for BLM2 for the two considered loss patterns and different protection strategies are in table 6.9.

BLM3

For BLM3 again no region specification was done and the steady state threshold values for each loss pattern are in table 6.10.

protected region	Loss pattern	Threshold BLM1 [μGy/s]
Whole Region	Twiss	10430
	SixTrack	3945
Region before BLM1	Twiss	10870
	SixTrack	4960
Region before MQ	Twiss	10750
	SixTrack	17320

Table 6.8: BLM1 steady state threshold at 450 GeV for the two considered loss patterns and various protection strategies.

Protected region	Loss pattern	Threshold BLM2 [μGy/s] MQ Protection
Whole Region	Twiss	1349
	SixTrack	1827
Region inside MQ	Twiss	2569
	SixTrack	1876

Table 6.9: BLM2 steady state threshold at 450 GeV for the two considered loss patterns and two protection strategies.

Loss pattern	Threshold BLM3 [μGy/s]
Twiss	260
SixTrack	175

Table 6.10: BLM3 steady state thresholds for injection energy.

6.2.4 Proposition for final steady state thresholds

The arguments for the choice of the final thresholds are the same as the ones for transient losses. The table 6.11 summarises the results for the three considered beam energies. Noteworthy is that thresholds, specially for BLM1, have no high variation with the beam energy. This is due to the assumption that with the beam energy the loss pattern changes. Thus for 450 GeV the results from SixTrack weights were taken, while for higher energies a transition to Twiss loss patterns is expected. This needs further investigation and particularly more experience.

	Threshold [μGy/s]		
Beam Energy [TeV]	BLM1	BLM2	BLM3
0.45	4960	1876	175
5	4619	1215	89.5
7	3789	805	83.5

Table 6.11: Final quench protecting thresholds for MQ in the steady state case. BLM1 was assigned to the region before its position and BLM2 to the MQ area. The third monitor takes the whole region into account.

6.3 Error estimation

The threshold T_{BLM} is depending on four parameters:

1. the cable quench margin H_{limit},
2. the conversion factor $C_{aC \rightarrow Gy}$,
3. the BLM signal Q_{BLM} and
4. the maximum energy deposition E_{max}.

$$T_{BLM} = \frac{H_{limit}}{E_{max}} C_{aC \rightarrow Gy} Q_{BLM} \tag{6.4}$$

For the enthalpy margin found with ROXIE the error is not exactly known. The calculations are done by numerical integration of the specific heat of the cable materials: copper and superconducting NbTi, as discussed in section 3.2.1. The specific heat of those materials, depending on the temperature and the magnetic field, was subject for precise studies and its error is negligible compared to the other present error sources. The mentioned studies [17] and [19] found similar coherent results at injection energy, but at 7 TeV beam energy the difference is higher depending on the assumptions. A comparison of the results from the different studies was done in [41].

The conversion constant $C_{aC \rightarrow Gy}$, based on the W-factor and the mass of the detector gas, can be considered as exactly known. Its error is negligible compared to the other present error sources.

The error of the BLM signal was found to be of about 29%, while the error of the energy density deposition was of 16%. Hence the accuracy of the calculated thresholds is of about 33%, found through the formula for the propagation of errors. One is therefore inside the margin defined as smaller a factor 5 by the BLM functionality specifications [42]. It was further specified that with more experience the factor should come below a value of 2.

6.4 Summary

The threshold calculation was done for:

1. three BLMs of the same beam line (due to symmetry the discussions and calculations are equivalent for the opposite beam line),
2. three beam energies: injection energy, 5 TeV and collision energy,
3. two time scales of beam losses (transient and steady state ones),
4. 14 loss locations,
5. four proposed regional specialisations of the ionisation chambers,
6. two protected elements (MQ and MB) and
7. two loss patterns: one from optical Twiss parameter calculations and the other from SixTrack simulations.

For each of the first three points and their combination a threshold needs to be estimated, resulting in a total of 18 final thresholds[4]. The fourth point was added to depict the high variation of the thresholds with the loss locations, particularly for the first monitor. This further demonstrates that the criticality of a lost beam depends on its impact location. The thresholds for point 5, 6 and 7 were presented. Knowing that the results inside each of the last points are redundant, decisions for respectively one of the discussed options are required (which element should be protected, which loss pattern is expected and from losses at which region should be protected).

All three ionisation chambers were found to be better placed for the protection of the superconducting quadrupole, than for the dipole. Furthermore a regional specialisation was decided to be optimal for the first two BLMs. The first detector can ideally protect from losses happening at the end of the upstream dipole, in the interconnection and at the beginning of MQ, while the second chamber is well placed to protect from losses occurring inside the quadrupole coil. For the threshold setting of the third BLM, the entire region was taken into account. The thresholds for injection energy were set according to the SixTrack loss scenario, whereas for higher energies a transition to a Gaussian beam halo is expected and hence the results from Twiss loss patterns are chosen for 5 and 7 TeV beam energy.

[4]With all mentioned cases and protection strategies a total of almost 200 potential thresholds was produced.

Chapter 7

Verification of simulation results with measurements

The operational thresholds are found through the combination of results from:

1. Geant4 simulations,
2. quench limit simulations and
3. loss patterns (proton impact locations).

To verify those results with measurements, it would be optimal to test each point separately.

It was planed to install a MQ magnet with its components and surroundings for a test beam line. There measurements with well known and defined initial conditions (particle energy, particle type, impact location, impacting angle, beam intensity) would be possible. The beam intensity could be increased till the occurrence of a quench of the superconducting coil (verification of point 2). In parallel, the corresponding BLM signals could be monitored (verification of point 1). Additionally the proton impact location could be varied according to the simulated loss locations in Geant4. This installation would be ideal, but was never realized.

For the verification of the loss patterns, the setup with MQ in the beam line is unusable. To investigate the proton impact locations one would need to place tracking detectors in the LHC beam pipe. Then, again under known initial conditions (beam energy, intensity, collimator settings), one could detect the lost protons and measure precisely the loss pattern (verification of point 3). A direct comparison between the SixTrack simulations, Twiss calculations and measurements could be done.

Unfortunately both proposals are not feasible and one needs to face the real situation, which is that no separation between the three points is possible, for the interconnection with beam losses. Furthermore the initial conditions (how many protons got lost, at which impacting angle, at which location) are not known for the interconnection[1]. The creation of well controlled conditions with impacts on the coils is not

[1]By accident a situation with well known initial conditions occurred once for MB. This situation corresponds to the second MB quench, where a corrector magnet was set to 750 μrad. This angle corresponds to the impacting angle, as no major manipulation to the beam was done in between. Further a Beam Position Monitor is placed right before the MB, giving the position of the beam. Also the beam intensity was known, being of $2 \cdot 10^9$ protons with an error of 10%.

allowed, as the magnets are fragile. One is therefore not able to make a direct comparison between results from the simulations and the measurements, which complicate the drawing of precise conclusions.

Nevertheless some comparisons are possible through measurements performed during the first runs of the LHC with beam. These runs are the injection tests in August and September 2008 and in October 2009 as well as periods with circulating beams in September 2008 and in November-December 2009. During these periods the beam had low intensity (up to $2 \cdot 10^{11}$ protons) and could not provoke any damage to accelerator elements.

These conditions have been used to perform numerous tests of the accelerator itself. For example the polarity checks of the corrector magnets or aperture scans. The losses occurring during this period might be very different from the ones which will be observed for normal operation of the LHC.

In particular no quenches of the MQ magnet have been observed and therefore the ultimate test of the proposed protection scenario for the Short Straight Section could not be directly tested.

Furthermore it should be mentioned that this operation period of the LHC is not devoted to optimise the luminosity in the experiments. Although collisions have been successfully managed and observed, the luminosity and the beam energy are still to low to gain new particle physics results. The period for physics and new discoveries starts in the first months of 2010.

An additional imprecision of later analyses comes from the fact, that point-like losses have been simulated at certain distances from each other and need to be compared to real losses, where a spread is existent.

7.1 Accuracy estimation through maximum values

The first attempt to verify if the results from the Geant4 simulations in combination with the loss patterns are correct, was to search for the highest values on the MQ BLMs, while the running periods of the LHC. Moreover one knows that never a quench of MQ occurred, which means that in theory the threshold should not have been reached.

BLM1

The first BLM on the MQs of the LHC arc reached in rare situations a total dose above 1500 μGy, going up to 2200 μGy without observing any quenches in the superconducting coils. For each of those events the beam would be dumped, although no quench occurred. One example is shown in figure 7.1. The opposite situation, that an MQ quenched without the BLM signals reaching the threshold was never observed, but would have been essential for a further analysis and evaluation of this study.

A special case is the third MB quench, where the signal of BLM1 could reach a dose of over 4 mGy without quenching the main quadrupole magnet. This is due to the fact that losses with an irregular mechanisms occurred somewhere close to the end of MB. There a high signal in the BLM is measured, whereas the energy deposition in the quadrupole magnet is low.

BLM2

The second BLM on the MQs of the LHC arc reached in rare situations a total

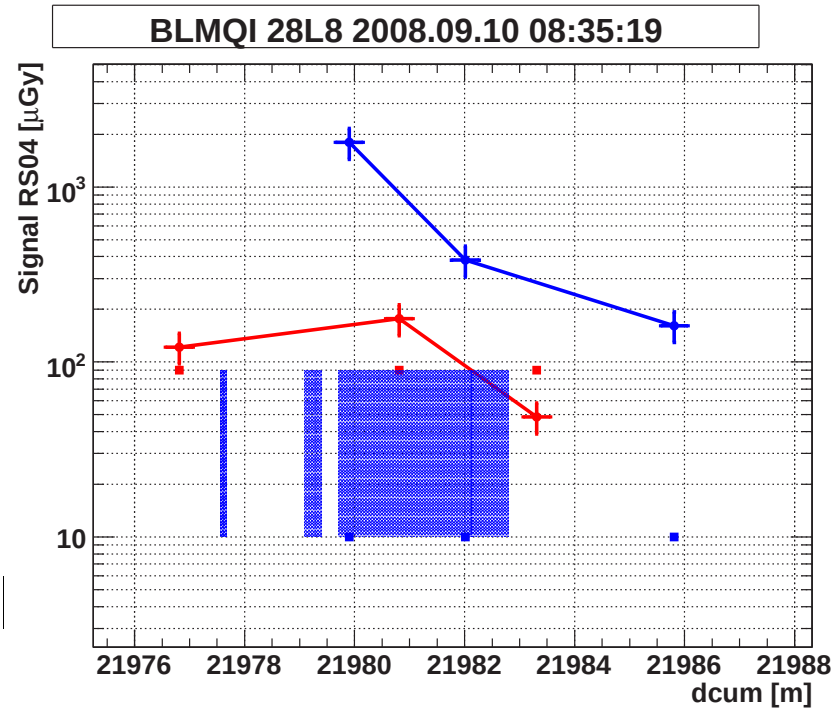

Figure 7.1: Loss profile of an example event with a high BLM1 signal, without a quench of MQ. The blue rectangles are the superconducting magnets. The large one in the middle is the main quadrupole coil, whereas the smaller ones are corrector magnets.

dose above 500 μGy, going up to 1100 μGy without observing any quenches in the superconducting coils. The case with 1100 μGy corresponds to the one shown in figure 7.12. The majority of the other cases correspond mainly to the same events as the ones leading to high BLM1 signals.

BLM3

For BLM3 many situations were found, where the signal came over the level of the threshold presented in this study. The majority of the situations stayed under a dose of 200 μGy though, which is still low compared to the other monitors. Still each time the threshold for BLM3 in table 6.5 is exceeded, a beam dump is induced. Those unnecessary downtimes of the LHC without any endangering of the machinery would make a correct beam operation impossible and is therefore unacceptable. The threshold setting for this monitor hence needs to be reviewed.

The Geant4 simulations have shown that losses inside MQ lead to very low BLM3 signals. A high signal in BLM3 can occur due to the following reasons:

1. the beam is lost after the middle of MQ,
2. the longitudinal scale of the losses is large, with a maximum inside MQ and still considerable losses after the coil or
3. high losses happend in the opposite beam and the BLM3 particle detection is due to crosstalk.

In the first situation MQ is at risk of quenching, but still for a major part protected by BLM2. Such a case is considered as rare according to the loss patterns, mainly accidental losses could lead to such an event, by for example missteering the beam.

The second case is supposed to be the one leading to the majority of the observed high signals in BLM3. The major part of the losses would still be inside MQ, but some protons would get lost in the aperture limitation of the interconnection downstream of main quadrupole, due to the longitudinal scale of the losses. Those losses would then lead to a high signal inside BLM3. Still BLM2 protects from such a situation as according to the loss patterns the maximum of the losses is expected to be inside or before MQ.

The situation is similar for the third case, where again MQ is endangered, but perfectly protected by the first monitor of the opposite beam line.

Therefore BLM3 plays a less important role for the protection of MQ, as the other BLMs are better situated to reliably compare their signals with the energy density in the coil. Its position is mainly used for later analysis of important events, as the tail of the hadronic cascade is measured. For the protection of the superconducting coils a position at the end of MB could be more serviceable according to the considered loss patterns. This new position would allow the protection of the upstream MB where higher losses are expected than in the MB downstream of MQ. A further argument for this proposition is the fact that already three quenches of the main dipoles upstream of MQ were observed.

7.2 Evaluation through the BLM signal ratios

Another criteria to check the validity of the results from Geant4 simulations in combination with the proton impact scenarios is to analyse the ratios of the signal between the BLMs. From the analysis of the BLM signal ratios, one can conclude on the BLM position at which the highest doses are reached. Not only the goodness of the BLM placements can be verified, but also the validity of the simulations and loss rate estimation can roughly be checked. Furthermore conclusions on the loss location can be done.

7.2.1 Signal ratios of BLMs for the same beam

Most information is contained in the ratio between the BLM on position 1 and the BLM on position 2. BLM3 not only had low signals in the Geant4 simulations, but it was furthermore also difficult to get high statistics from LHC data. Therefore further emphasis will lie on the ratio between BLM1 and BLM2.

In figure 7.2 one can see the BLM signal ratios for the loss locations from the Geant4 simulation. Both curves have a flat part and a steep one. For losses in the interconnection and before, BLM1 has the highest signals. This changes once the simulated loss location is after the placement of BLM1. Then BLM2 detects the major part of the losses. For the steep parts of the curve one can more easily deduce from the observed ratio on the location of the losses, whereas the flat part make such a conclusion very difficult and imprecise. For locations before around z = -2000 mm one has hence a lack of sensibility. Therefore one can through both ratios only deduce

if the losses happend in the inside of the coil or before.

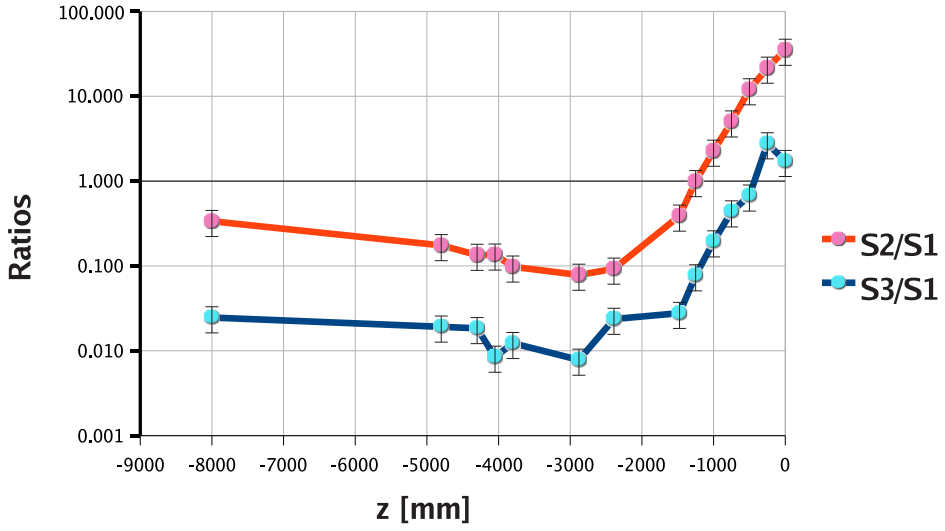

Figure 7.2: BLM signal ratios from the Geant4 simulations.

The next step is to compare the ratios from the Geant4 simulation with the measurements from the LHC injection tests from October the 26th 2009 at 02:00 until 06:00 local time in sector 2 and 3 for beam line 1. During this injection test an aperture scan has been done. The event selection for further analysis concerning the ratios of the signals is the following:

- BLMs are from the same quadrupole,
- at least one of the two signals is above 0.01 Gy/s in RS01 and
- the signals have the same timestamp.

It is therefore assured, that data satisfying those conditions are coming from the same loss event. RS01 was used for the analysis.

The distribution of the points comparing the signals from BLM2 with the ones from BLM1 is shown in the left plot of figure 7.3. The distribution seems to have two populations. One with a maximum around 0.2 and the other one around 0.7. Comparing those values with the ones from figure 7.2, the first maximum could be due to losses coming from before the coil, while a ratio of 0.7 from the second maximum would correspond to losses closer to the superconducting quadrupole around z = -1250 mm.

To augment the statistics, further analyses were done including injection tests data from 2008. Those are shown in the right plot of figure 7.3 and in 7.4. The second population disappears and also the maximum is slightly displaced in each case, staying around 0.1 to 0.5. In the two situations of figure 7.4 a much larger tail with higher ratios is observed, than in the other two cases.

The distributions corresponding to the ratios S3/S1 can be seen in figure 7.5 and 7.6. Here the maximum value is in general smaller than for the ratio S2/S1. Also the

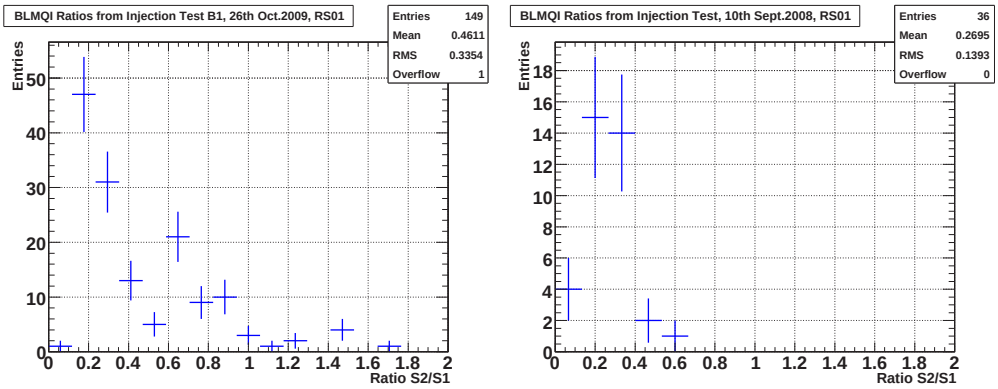

Figure 7.3: Distribution of the ratios between BLM2 and BLM1 on MQ. The left plot corresponds to an aperture scan.

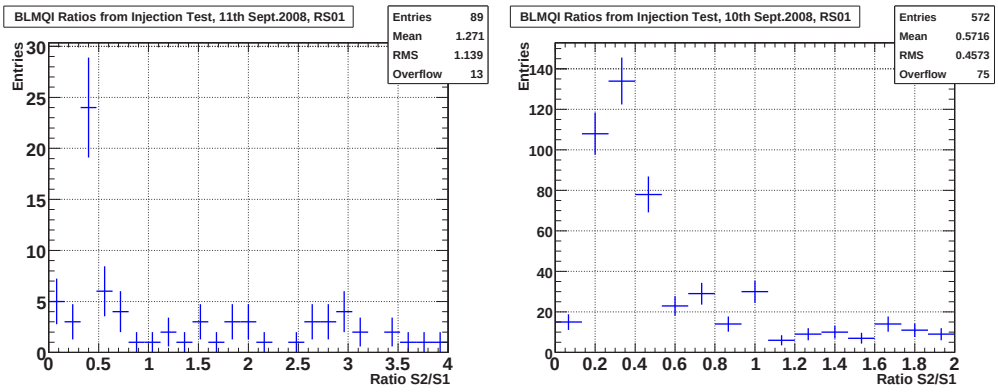

Figure 7.4: Distribution of the ratios between BLM2 and BLM1 on MQ for two different days.

tail to higher values is much smaller. It therefore is a rough confirmation of earlier estimations and of the fact that BLM3 plays a secondary role compared to the other BLMs in the protection of MQ.

In table 7.1 the maximum values from the distribution of the measured data is compared to the most probable ratios for the two analysed loss patterns. The large difference between Twiss and SixTrack loss scenarios for the ratio S2/S1 is due to the high variations of the signals with the loss location (see table 5.10), specially for the first ionisation chamber, and the fact that from SixTrack simulations high losses are expected inside MQ (signals high for BLM2 and low for BLM1), while from Twiss calculations losses occur for a majority in the interconnection (signals high for BLM1 and low for BLM2). As a result a factor of 3.5 is obtained between the Twiss S2/S1 ratio and the one from SixTrack. Through the regional specialisation of the BLMs this large difference becomes less problematic for the threshold setting, as the protection strategy corresponds to a separation between losses inside and outside MQ.

The measured S2/S1 ratio has its most probable value between the two loss scenarios, which makes it difficult to estimate which loss pattern better describes the real situation. Taking into account the errors, one finds a greater overlap between mea-

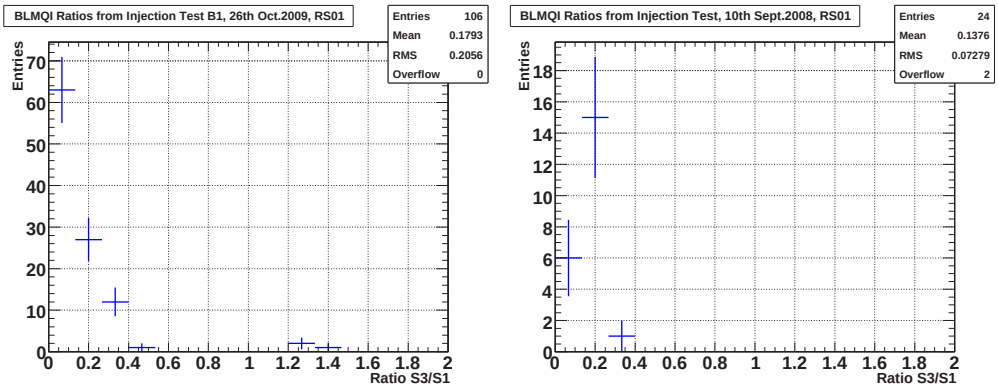

Figure 7.5: Distribution of the ratios between BLM3 and BLM1 on MQ.

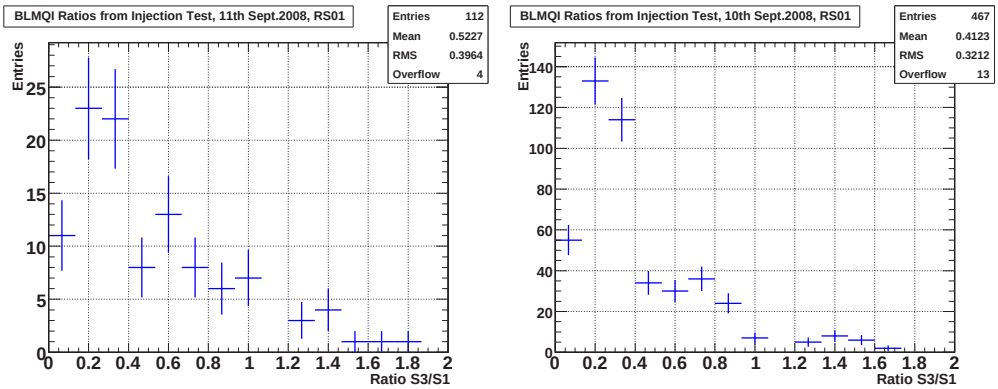

Figure 7.6: Distribution of the ratios between BLM3 and BLM1 on MQ.

surements and SixTrack ratios (S2/S1 and S3/S1), than for measurements and Twiss ratios. This can be considered as a rough confirmation of the threshold setting with the SixTrack loss scenario at injection energy.

Moreover the simulation in combination with the loss patterns seem to underestimate the signal in BLM3. The possible explanations for this observation were discussed earlier in section 7.1.

	S2/S1	S3/S1
Measurements	0.3 ± 0.2	0.225 ± 0.175
Twiss	0.13 ± 0.05	0.02 ± 0.008
SixTrack	0.46 ± 0.18	0.04 ± 0.016

Table 7.1: Comparison of the most probable ratios for each case.

7.2.2 Crosstalk ratios

Along the LHC main quadrupole magnet six BLMs have been installed, three for each beam. The signal collected at the beam line opposite to the one where losses occurred, is referred to as crosstalk.

To analyse the crosstalk ratios is interesting for practical reasons: in some cases it can be worth analysing to conclude on the reasons of some major loss events and to have some additional information, yet it can also be considered as parasitic background. Understanding from the simulation how high the signal crosstalk is expected, is an important information for future deductions from LHC measurements. In this study the crosstalk ratios are analysed to have an additional verification of the simulation and loss pattern assumptions.

The used nomenclature is the following:

- BLM1 from beam line 1: S1B1 (for Signal1 Beam1) and B1I1 (for Beam1 Internal1)
- BLM2 from beam line 1: S2B1 (for Signal2 Beam1) and B1I2 (for Beam1 Internal2)
- BLM1 from beam line 2: S1B2 (for Signal1 Beam2) and B2E1 (for Beam2 External1)
- BLM2 from beam line 2: S2B2 (for Signal2 Beam2) and B2E2 (for Beam2 External2)

Internal and external refere to the BLM placement inside and outside respectively of the LHC circle. For Sector 2/3 of the LHC external corresponds to beam line 2 and internal to beam line 1, but this changes for other sectors due to the interaction points, where the beams can collide and the beam lines change place.

BLM1 of beam line1 and BLM2 of beam line 2 are interesting to compare, as well as BLM2 of beam line 1 with BLM1 of beam line 2. This is due to their close placement in longitudinal direction.

The crosstalk ratios from Geant4 simulations are shown in figure 7.7. For some ratios multiple very different loss locations are possible.

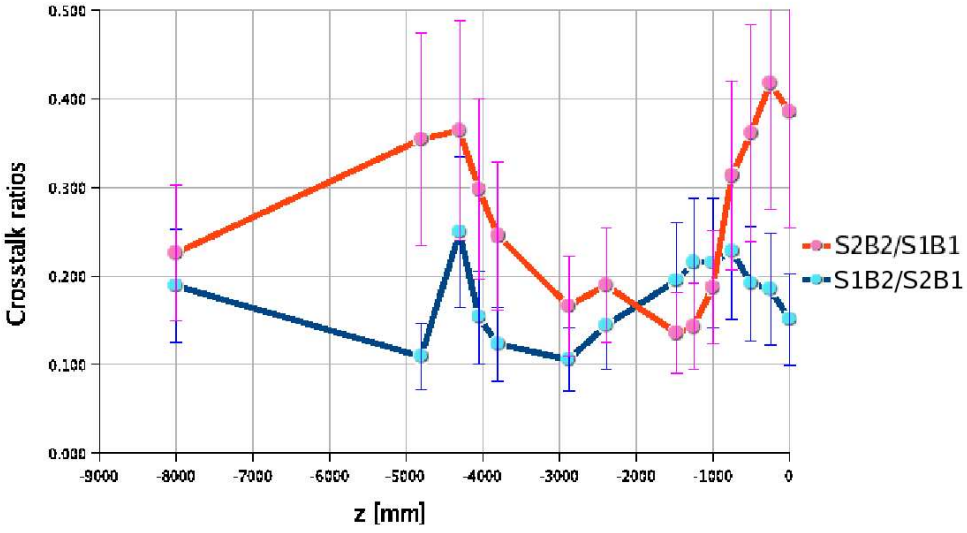

Figure 7.7: BLM crosstalk ratios for each loss location from the Geant4 simulations.

The data collection again happens from the injection tests in IP2-3 on October the 26th of 2009 from 02:00 until 06:00 local time with the same conditions as in the previous section. No situation was detected, where the crosstalk would reach higher signals than the BLM on the beam line with beam.

The distribution of the crosstalk ratios can be seen in figures 7.8 and 7.9. The maxima are at about 0.085 for both, whereas the ratios from the simulated loss location are in general above 0.1 as shown in figure 7.7. The crosstalk signals seem to be overestimated in the simulations.

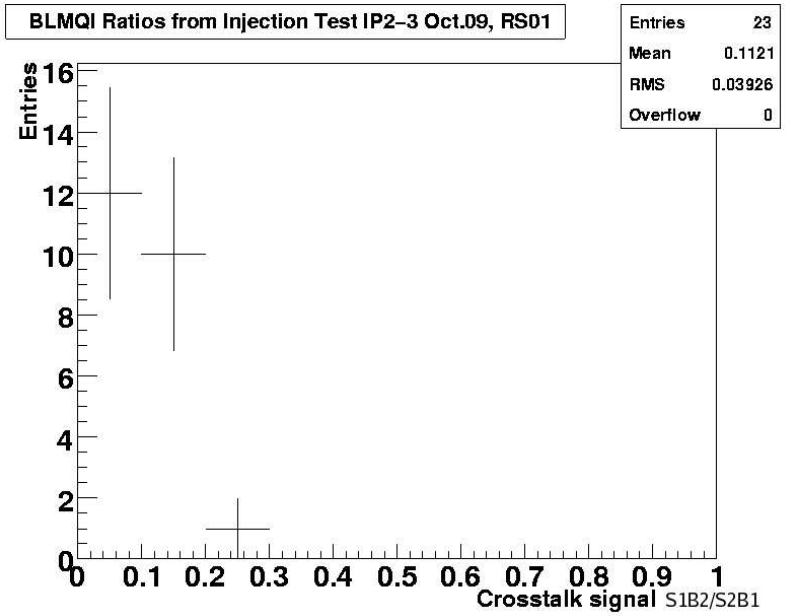

Figure 7.8: Distribution of the Crosstalk ratios between BLM1 of beam 2 and BLM2 of beam1 on MQ.

In table 7.2 the maximum values from the distribution of the measured signal ratio data is compared to the most probable crosstalk ratios for the two analysed loss patterns. Again the simulations do not seem to ideally predict the crosstalk effect in both cases. The differences between SixTrack and Twiss ratios are not significant due to the error values.

	S1B2/S2B1	S2B2/S1B1
Measurements	0.085 ± 0.015	0.085 ± 0.015
Twiss	0.16 ± 0.06	0.2 ± 0.08
SixTrack	0.18 ± 0.07	0.25 ± 0.1

Table 7.2: Comparison of the most probable crosstalk ratios for each case. Even taking into account the high error values, the crosstalk effect is significantly overestimated in the simulations (of about a factor 2).

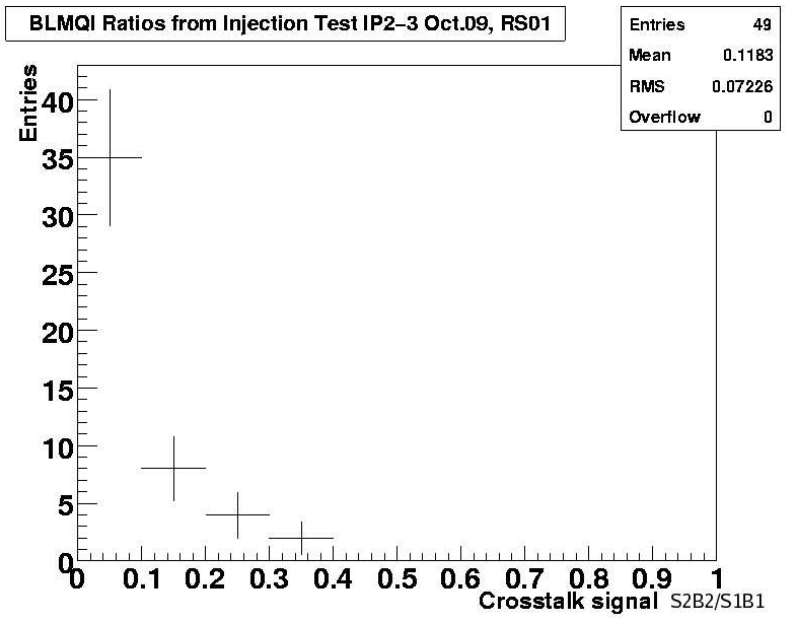

Figure 7.9: Distribution of the Crosstalk ratios between BLM2 of beam 2 and BLM1 of beam1 on MQ.

7.3 Reconstruction of the location of the maximum loss

The relation between the signals in the chambers makes it possible to estimate where the losses of the protons likely happend. This is done for the first time. The employed method is based on the least squares fit. From the Geant4 simulations one knows for each loss location j the signal S_{ij}^{Geant4} per proton in the ionisation chambers. In order to be able to compare those values with the ones from real loss events in the LHC, one needs to normalise the signals. This is done by dividing the measured signal S_i of each BLM i by the total sum of the signals:

$$Ratio_i = \frac{S_i}{\sum_{k=1}^{n} S_k} \tag{7.1}$$

The same is done for the Geant4 signals at each loss location j and for each BLM i:

$$Ratio_{ij}^{Geant4} = \frac{S_{ij}^{Geant4}}{\sum_{k=1}^{n} S_{kj}^{Geant4}} \tag{7.2}$$

and its results can be seen in figure 7.10.

The strategy is to find the loss locations for which the theoretical ratios from Geant4 $\text{Ratio}_{ij}^{Geant4}$ are the closest to the ratios Ratio_i from real loss events in the LHC. This can be evaluated through the sum of the squared differences between the ratios at each loss location, taking the error σ_{ij}^{Geant4} values into account:

$$L_j = \sum_{i=1}^{n} \left[\frac{Ratio_i - Ratio_{ij}^{Geant4}}{\sigma_{ij}^{Geant4}} \right]^2 \tag{7.3}$$

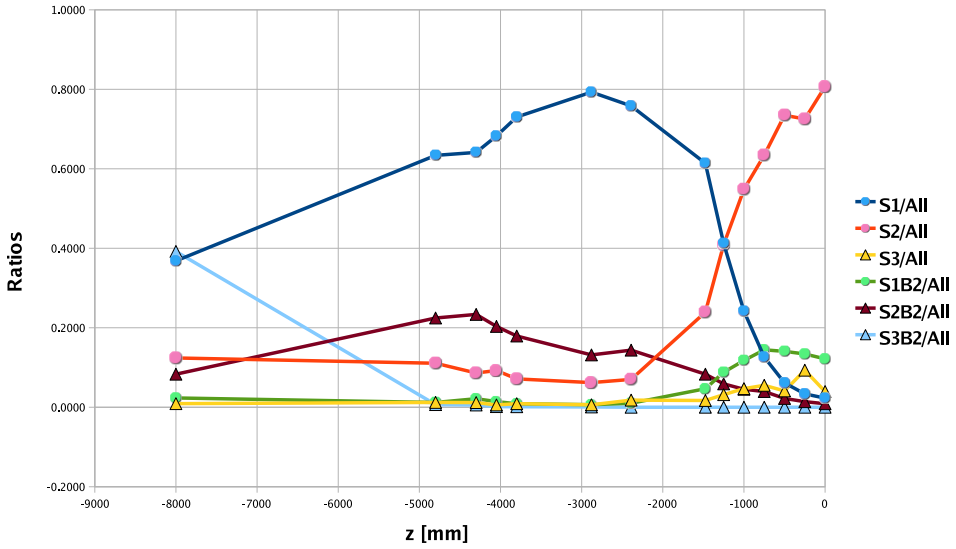

Figure 7.10: Normalised signals of all BLMs for each beam line as a function of the loss location. There is a clear domination of the BLM1 signal over almost the entire region. Exceptions are losses from inside the coil and the ones close to the middle of MQ.

In the literature this value is usually called S as it refers to a sum. Here yet to avoid confusion with the BLM signals S_i, one chose to call the value L, referring to least in the name of the utilised method.

The smaller this L-value is for a loss location, the better is the description of the event by losses happening at this point. Hence the loss location where this function reaches its minimum is the most appropriate to explain the observed BLM signals. This will further be shown and analysed on the example of six major loss events seen in figures 7.11, 7.12 and 7.13. The loss profiles of the first three MB quenches, two orbital bumps and another situation with high losses are shown. All six cases were observed at a beam energy of 450 GeV and in all plots one can see the quadrupole coil with its six monitors and their signals. Furthermore is included the dipole upstream of the MQ and, if existent, its BLMs.

The values were taken from RS04, in order to collect the total dose and minimise the falsification due to electronic saturation of the chambers at lower running sums.

For each of those examples, except one, the first BLM on the line with beam had the highest signals. The exception (right plot in figure 7.12) is very rare [2] and was chosen in order to compare the results of the presented method. Furthermore the collected dose in the second chamber is always higher than the dose in the third one. This was expected in the Geant4 simulation. Yet again there is one exception: the first quench of a main dipole. An explanation could be a very high spread of the lost protons, so that the particles would reach BLM1 and BLM3 easier through the interconnections on both sides of the MQ, than BLM2, being shielded by the cold mass.

[2]The author would estimate that in more than 95 % of the cases with high losses, the signal in BLM1 is greater than in the one in BLM2.

The crosstalk signals are at least a factor of ten underneath the ones of the chamber on the active beam line, using the same crosstalk comparison as in section 7.2.2. Moreover in four cases the second crosstalk monitor has the highest value, due to its close position after the interconnection. For the first and the second MB quench it is the third crosstalk chamber that has the highest value, which could be a hint to the fact, that the maximum of the losses happend shortly upstream to this BLM position.

In the case of the first three MB quenches, one can assume that the maximum of the losses happend inside the main dipole, which can be clearly seen for the first two quenches, where MB BLMs are installed. For the two observed orbital bumps again BLMs are present on the main dipole. They bring additional information and in contrary to the situation for the MB quenches, their signals are comparably low. This is an indication for losses happening at the end of MB or downstream of the dipole magnet. This will further be compared with the results from earlier presented method.

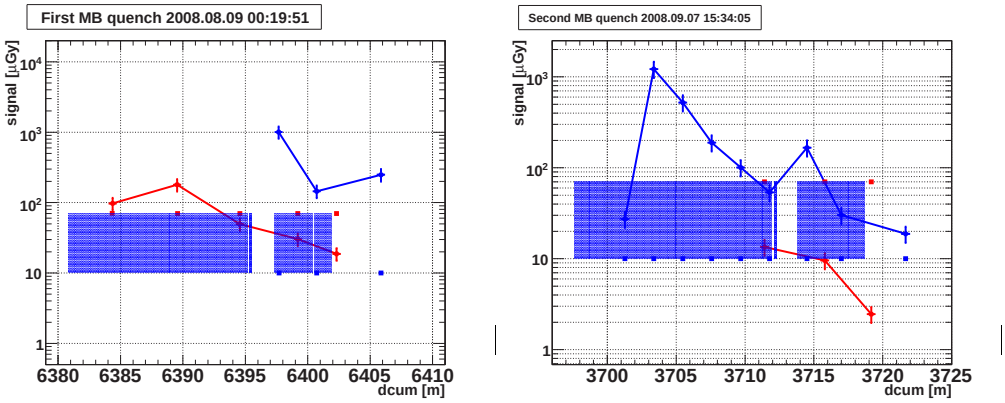

Figure 7.11: Loss Profiles. The BLM signals and positions for beam line 1 are in blue, while those for beam line 2 are in red. The blue rectangles indicate the location of the magnets, the large one being MB and the smaller one MQ. The left plot corresponds to the loss profile of the first MB quench and the right one to the second MB quench. In both cases the beam came from the left side.

In figure 7.14 one can see the L-values as defined in equation 7.3 for each loss location and for the discussed situations with high losses in figures 7.11, 7.12 and 7.13.

For the two first main dipole quenches the method finds the minimum inside MB at z = -8000 mm. This means that the method found that losses at this position best describe the observed signal compared to the other loss locations, which was also expected from the loss profiles as the MB BLMs show high values.

For the situation in the right plot of figure 7.12 with a high signal in BLM2, corresponding to the pink curve in figure 7.14, the minimum was found to be inside MQ at z = -750 mm.

The L-value for the two orbital bumps is slightly lower for the point at the end of MB at z = -4300, than for the one at z = -8000 mm, which approximately again corresponds to what was expected from the loss profiles.

Surprising is the fact that for the six analysed situations, the interconnection was found to have comparably high L-values. Yet this could simply be due to the choice of

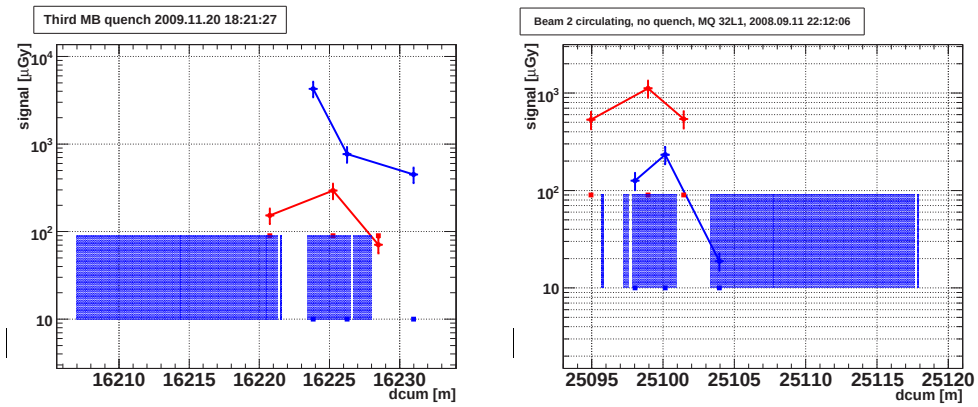

Figure 7.12: The left plot corresponds to the loss profile of the third MB quench and the right one to a situation with high losses, while beam 2 was circulating. The beam hence came in this plot from the right side. Noteworthy is that for this loss event, though being large, no information could be found in the LHC-logbook.

the special loss events.

A possible amelioration of the method is to take the longitudinal scale of the losses into account. For now the LHC loss events are compared with point like losses from the simulation and estimates which best describes the situation. This has some imperfections, which can be explained through an example: The maximum of the losses happen in the middle of MQ, but at the same time some little losses occur also in the interconnection. As already mentioned the high losses inside MQ are shielded by the cold mass, whereas the little losses from the interconnection directly lead to a relatively high signal in BLM1. It is hence possible, that both BLMs collect the same amount of charges in the real loss event, although the Geant4 simulations expect an about 50 times higher signal in BLM2 than in BLM1 for losses in the middle of MQ. Finally the method would correctly estimate that the losses came from inside the coil, but would at the same time find an extremely high L-value for the possibility that the protons got lost in the middle of MQ.

The method enables to estimate which Geant4 loss location best describes the observed detector signals from major loss events. The discussed examples show that coherent results could be found.

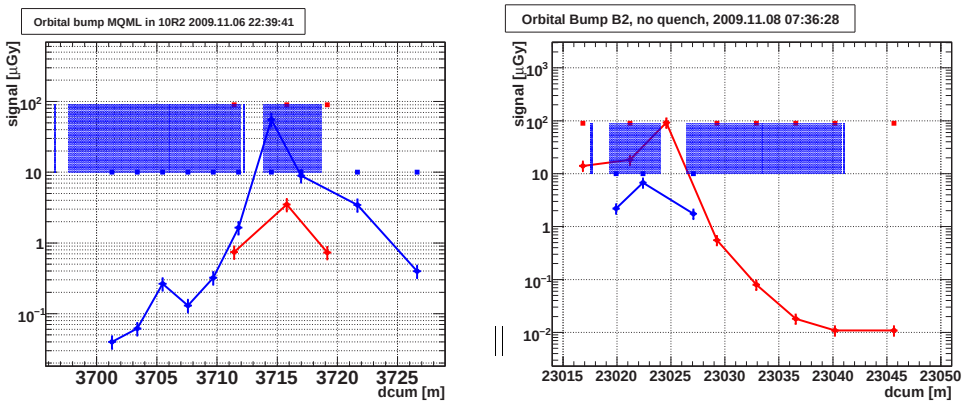

Figure 7.13: Both plots correspond to the loss profile of orbital bumps effectuated on different days and for different beam lines. In the left plot the beam is coming from the left side, corresponding to beam 1, while in the right plot the bump was done with beam 2.

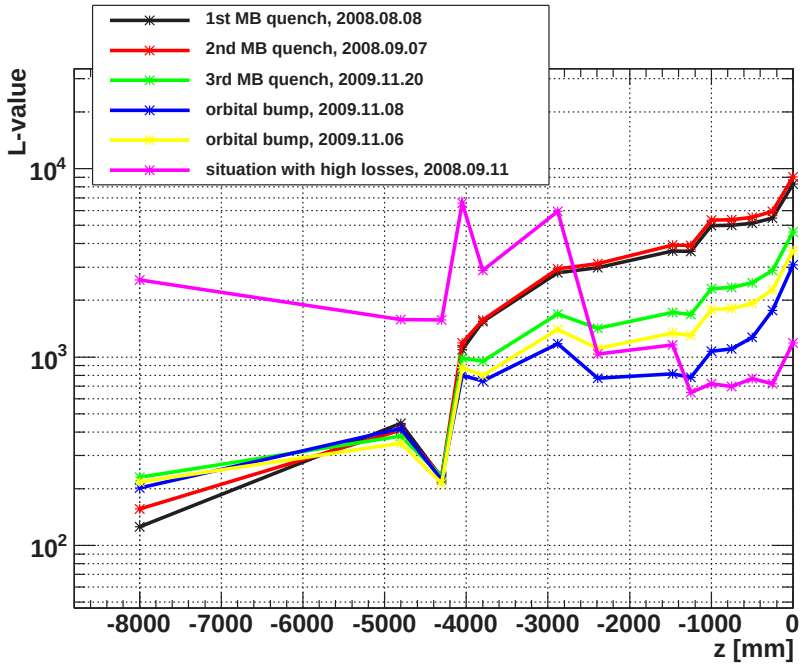

Figure 7.14: L-values for each Geant4 loss location for the six example situations with high losses. The z with the lowest L-value for each curve corresponds to the loss location that best describes where the maximum of the losses occurred in the respective situation. A comparison with the six loss profiles and the discussed expectations shows a general agreement.

Chapter 8

Conclusion

The purpose of this study was to estimate the quench protecting thresholds for the Beam Loss Monitors at the interconnection between the main dipole and the main quadrupole magnet in the LHC.

In order to attain this goal different investigations on the topic have been done. The calculation of the enthalpy limit has been performed with ROXIE code. It was found that the main quadrupole is slightly less sensitive to losses than the main dipole magnet. At injection energy the enthalpy limit for MQ at its most exposed area is of 36.52 mJ/cm^3 and of 3.44 mJ/cm^3 at a beam energy of 7 TeV. The quench level values for the steady state case have been taken from the literature and are about 48 mW/cm^3 and 23 mW/cm^3 respectively.

Two loss patterns were chosen for the region of the interconnection, one relying on the beam optical parameters and the other on beam halo tracking simulations. The common points are that no losses are expected in the region of largest aperture, while the maximum of the losses is estimated in both cases at the beginning of the beam screen, shortly after the zone without losses. The main disagreement between the two presented approaches concerns the losses in the middle of the quadrupole coil.

The simulation of lost protons with Geant4 at different locations enabled to understand the importance of the interconnection for the BLM signals, as the interconnection has less shielding effect than the cryostat mass. Furthermore the link between energy deposition in the coil and signal in the BLM was done for each loss location and for the two loss patterns, in order to compare the results.

The threshold could now be estimated and a detailed understanding and analysis of the situation enabled the proposition of the regional specialisation of protection functions for BLM1 and BLM2. The protection purpose for BLM1 was found to be optimal by only taking into account losses coming from the end of the main dipole magnet, the interconnection and the beginning of the main quadrupole magnet, while BLM2 is perfectly situated to protect from losses inside the superconducting quadrupole coil. This regional specialisation has the advantage of a better accuracy and efficiency of the system, but goes at the expense of redundancy, which was defined as having a high priority with regard to safety.

The monitor in position 3 seems not to enhance significantly the protection capability of the system for the considered loss scenarios. The proposal is discussed to place this BLM on the preceding main dipole magnet.

The quench protecting threshold for transient losses for BLM1 was found to be around 1520 ± 460 μGy at injection energy and 178 ± 55 μGy at 7 TeV beam energy. For BLM2 the respective values are 575 ± 189 μGy and 29.7 ± 9.7 μGy.

For steady state losses the quench protecting threshold for BLM1 is estimated at about 4960 ± 1640 μGy/s at injection energy and 1876 ± 620 μGy/s at collision energy. For BLM2 the respective values are 3789 ± 1250 μGy/s and 805 ± 266 μGy/s. Those values are used as initial settings in the BLM system for the 2010 run.

The thresholds are evaluated using first available data from the LHC runs. During those running periods no quench of the superconducting quadrupole coil occurred, which would have allowed to optimally calibrate the results.

With more experience and ideally quenches of the main quadrupole magnet in different situations, those thresholds will be reevaluated.

Finally for the first time an attempt was made to reconstruct from the signals in the BLMs the longitudinal location of the maximum losses. One can estimate after a loss event which loss location from the Geant4 simulations best describes the observed BLM signals. Accuracy, sensitivity and resolution are limited, nevertheless first coherent results could be found and further development can be envisaged.

Bibliography

[1] W. Barletta, M. Bai: *Fundamentals of Accelerator Physics and Technology with Simulations and Measurements Lab*, USPAS Course, June 15-26, 2009.

[2] S. Y. Lee: *Accelerator Physics*, Second Edition, World Scientific Publishing Co. Pte. Ltd., 2004.

[3] *LHC Design Report, Volume 1*

[4] H. Wiedemann: *Particle Accelerator Physics*, Springer, 2007.

[5] `http://quench-analysis.web.cern.ch/quench-analysis/phd-fs-html/node29.html`, 09.02.2010.

[6] `http://quench-analysis.web.cern.ch/quench-analysis/phd-fs-html/node34.html`, 09.02.2010.

[7] D. Bocian, B. Dehning, A. Siemko: *Modeling of Quench Limit for Steady State Heat Deposits in LHC Magnets*, IEEE Transactions on Applied Superconductivity, June 2008

[8] J. B. Jeanneret, D. Leroy, L. Oberli, T. Trenkler: *Quench levels and transient beam losses in LHC magnets*, LHC Project Report 44, 1996.

[9] T. Böhlen: *Beam Loss Patterns at the LHC Collimators Measurements & Simulations*, CERN-THESIS-2008-092, 2008.

[10] M. Lamont: *Estimates of Annual Proton Doses in the LHC*, Project Note 375, 2005.

[11] T. Garavaglia: *Proton-Proton Scattering Contribution to Emittance Growth*, Proceedings of PAC, 1993.

[12] F. Zimmermann, M.P. Zorzano: *Touschek scattering in HERA and LHC*, LHC Project Note 244, 2000.

[13] *Emittance growth induced by electron cloud in proton storage rings*, CERN-THESIS-2008-096, 2008.

[14] C. Benvenuti et al., *Vacuum Properties of TiZrV Non-Evaporable Getter Films*, Vacuum Volume 60 pages 57-65, CERN, 2001.

[15] V. Kain: *Machine Protection and Beam Quality during the LHC Injection Process*, CERN-THESIS-2005-047, 2005.

[16] B. Auchmann: *ROXIE Users Documentation*, CERN, 2007.

[17] N. Schwerg, B. Auchmann and S. Russenschuck: *Validation of a Coupled Thermal-Electromagnetic Quench Model for Accelerator Magnets*, 2007.

[18] B. Auchmann: *private communication*.

[19] P. Granieri, M. Calvi, P. Xydi, B. Baudouy, D. Bocian, L. Bottura, M. Breschi and A. Siemko: *Stability Analysis of the LHC Cables for Transient Heat Deposition*, LHC Project Report 1089, 2008.

[20] D. Bocian: *private communication*.

[21] R. Assmann, F. Schmidt and F. Zimmermann: *Equilibrium beam distribution and halo in the LHC*, Proceedings of the European Particle Accelerator Conference EPAC02, Paris, France, 2002.

[22] C. Bracco: *Commissioning Scenarios and Tests for the LHC Collimation system*, CERN-THESIS-2009-031, 2009.

[23] L. Ponce: *Locations of BLM based on proton loss maps*, LHC Collimation Working Group Meeting, June 19th 2006.

[24] W. Demtröder: *Experimentalphysik 1.*, Fifth Edition, ISBN: 978-3-540-79294-9, Springer, 2008.

[25] D. H. Wilkinson: *Ionisation chambers and counters*, Cambridge Monographs on Physics, Cambridge, 1950.

[26] G. F. Knoll: *Radiation Detection and Measurement*, Third Edition, ISBN: 0-471-07338-5, John Wiley & Sons, 2000.

[27] M. Stockner: *Beam Loss Calibration Studies for High Energy Proton Accelerators*, PhD thesis, CERN, 2007.

[28] D. Kramer: *Design and implementation of a detector for high flux mixed radiation fields*, PhD thesis, CERN, 2008.

[29] B. Dehning: *Beam loss monitoring requirements and system description*, Machine Protection System Workshop, 12.04.2005.

[30] W. Friesenbichler: *Development of the Readout Electronics for the Beam Loss Monitors of the LHC*, CERN-THESIS-2002-028, 2002.

[31] G. Venturini: *private communication.*

[32] *BLMLHC*,`http://bdidev1.cern.ch/bdisoft/development/BDI-Domains/bdeyelids/bdeyelids.php?currentSelection=GI&currentInstrument=BLMLHC&currentDomain=LHC`, 10.12.2009.

[33] C. Zamantos: *The Real-Time Data Analysis and Decision System for Particle Flux Detection in the LHC Accelerator at CERN*. PhD thesis, 2006.

[34] J. Allison et al: *Geant4-a simulation toolkit*, Nuclear Instruments and Methods in Physics Research, A 506 (2003) 250-303, 2003.

[35] A. Priebe: *The quench prevention of the LHC Main Dipoles*, CERN, 2009.

[36] E. B. Holzer, B. Dehning: *Longitudinal loss distribution along the LHC*, Proceedings of EPAC, 2004.

[37] C. Hoa, F. Cerutti, E. Wildner: *Energy Deposition in the LHC Insertion Regions IR1 and IR5*, CERN-LHC-PROJECT-Report-1167, 2008.

[38] M. Sapinski: *private communication*.

[39] `http://mathworld.wolfram.com/ErrorPropagation.html`, 09.10.2009.

[40] L. Ponce: *Positions of the BLM in the Dispersion Suppressor regions*, 2007.

[41] B. Dehning, A. Priebe, M. Sapinski: *Transient energy deposition in LHC MB magnet and quench threshold test*, Project Note 422, CERN, 2009.

[42] B. Jeanneret, H. Burkhardt: *Functional Specification on the Measurement of the Beam Losses in the LHC Rings*, EDMS Document No. 328146, CERN, 2004.